

The Sintering Effects of Time, Temperature, and ZnO Additions

on $(\text{Ca}_{0.6}\text{Mg}_{0.4})\text{Zr}_4(\text{PO}_4)_6$ [CMZP] Ceramics

by

James R. Clarke Jr.

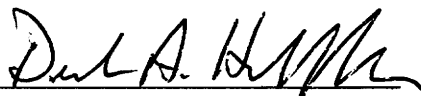
Thesis submitted to the Faculty of the
Virginia Polytechnic Institute and State University
in partial fulfillment of the requirements for the degree of

MASTER OF SCIENCE

in

Materials Science and Engineering

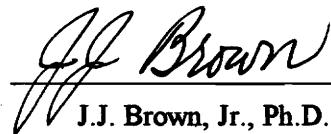
APPROVED:



D.A. Hirschfeld, Ph.D. (Chair)



W.T. Reynolds, Ph.D.



J.J. Brown, Jr., Ph.D.

July 1996
Blacksburg, Virginia

Keywords: ceramics, sintering, microstructure, strength, thermal expansion

2)

LD
5655
V255
1996
C538
0.2

**The Sintering Effects of Time, Temperature, and ZnO Additions
on $(\text{Ca}_{0.6}\text{Mg}_{0.4})\text{Zr}_4(\text{PO}_4)_6$ [CMZP] Ceramics**

by

James R. Clarke Jr.

Dr. Deidre Hirschfeld, Chair

Material Science and Engineering

(ABSTRACT)

The sintering of $(\text{Ca}_{0.6}\text{Mg}_{0.4})\text{Zr}_4(\text{PO}_4)_6$ powder (CMZP) synthesized via a new solid-state reaction method was investigated for application as a thermal barrier in next generation internal combustion engines. Specifically, CMZP is being considered as a potential material for the manufacture of exhaust port liners to increase the overall performance of diesel engines. The effects of firing time, firing temperature, and amount of ZnO sintering aid on modulus of rupture (MOR), bulk density, and coefficient of thermal expansion (CTE) were determined for both dry pressed and slip cast samples to optimize the physical properties for this application. For both processing methods, suppressing the formation of secondary interparticle phases (grain boundaries) was found to be the controlling factor for obtaining high strength and positive thermal expansion.

For a given ZnO level, increases in firing time and/or temperature resulted in improved density but a degradation in microstructure (undesirable grain growth, formation of a liquid phase, and intra-/trans- granular microcracking), accompanied by a reduction in MOR and negative CTE values. Therefore, optimizing bulk density was determined to be counter-productive for improving strength when ZnO is used as a sintering aid.

For dry pressed samples (-400 mesh powder), the highest MOR achieved was 27.6 MPa when fired to 1300°C for 0.5 h with 0.5wt% ZnO. Under these conditions, the bulk density was 79% of theoretical and the average CTE to 1000°C was +1.2 ppm/°C.

For slip cast samples (initial particle size approximately 1µm), a MOR of 111 MPa was achieved when fired to 1175°C for 0.7 h with 2wt% ZnO. Under these conditions, the bulk density was 96% of theoretical and the average CTE to 1000°C was +2.0ppm/°C. The mechanical and thermal properties obtained in this study make CMZP a suitable material for exhaust port liners in diesel applications.

All high strength samples, regardless of forming method, exhibited fine grained microstructures void of a liquid phase and microcracks. These same samples also exhibited smooth fracture surfaces indicating transgranular fracture, which is consistent with strong, brittle ceramics.

ACKNOWLEDGMENTS

The author wishes to thank:

- Materials Technology of Virginia (MATVA), who funded this research through a DOE Energy Related Inventions Program grant, and for supplying the CMZP material.
- Virginia Center for Innovative Technology.
- Caterpillar Inc. for the opportunity to conduct research at their Technical Center.
- Dr. Deidre Hirschfeld for accepting me as one her graduate students and for her leadership and support throughout this project.
- Dr. Jesse J. Brown for accepting the responsibilities of a graduate committee member.
- Dr. Bill Reynolds for being a member of my graduate committee and for introducing me to the fundamentals of metallurgy through his excellent undergraduate course.
- Dr. Mike Haselkorn for his leadership and assistance while at Caterpillar. His review of the thesis and presence at the defense was much appreciated.
- Everyone at Caterpillar for their assistance and friendship during my research at the Technical Center, including but not limited to Mike, Greg, Matt, Kurt, Jack, Chung, Vergil, Jill (both of them), Laura, and Karan.
- The MSE gang: Levon (and Tracy), Jud, Becky, Mike, Joel, Heidi, Jen (and John), and Kim.
- The MSE staff, especially Amy, Jan, and LeeAnn.
- All my other friends not mentioned but whose camaraderie is treasured just the same.
- My entire family for their everlasting love and support.

“There is nothing more difficult to take in hand, more perilous to conduct, or more uncertain in its success than to take the lead in the introduction of a new order of things, because the innovator has for enemies all those who have done well under the old condition, and lukewarm defenders in those who may do well under the new.”

-Niccolo Machiavelli-
IL PRINCIPE (1513)

TABLE OF CONTENTS

1. INTRODUCTION	1
2. LITERATURE REVIEW	4
2.1 Background of CMZP	4
2.1.1 General Overview	4
2.1.2 Crystal Structure	4
2.1.3 Effects of Composition	5
2.2 Sintering and Densification	7
2.2.1 General Summary of Sintering Processes	7
2.2.2 The Driving Force for Sintering	9
2.2.3 Solid State Sintering	9
2.2.4 Liquid Phase Sintering	10
2.3 Microcracking of Anisotropic Materials	11
2.3.1 The Formation of Microcracks	11
2.3.2 The Effects of Microcracking on Thermal Expansion	12
3. EXPERIMENTAL PROCEDURE	14
3.1 Dry Pressed Samples	14
3.2 Slip Cast Samples	15
3.3 X-ray Diffraction Samples	16
3.4 Bulk Density	17
3.5 Dilatometric Studies	17
3.6 MOR Analysis	18
3.7 Particle Size Analysis	18
3.8 Micrographs	19
3.9 Thermal Aging of Slip Cast Samples	19
4. RESULTS	20
4.1 X-ray Diffraction	20
4.1.1 Effects of Temperature	20
4.1.2 Effects of Time	26
4.2 Effects of Processing on Densification	26
4.2.1 Dilatometric Studies	26
4.2.2 Development of Microstructure with Temperature for Dry Pressed Samples	31
4.3 Effects of Processing on Bulk Density	38
4.3.1 Dry Pressed Samples	38
4.3.2 Slip Cast Samples	39

4.4	Effects of Processing on Microstructure	41
4.4.1	Dry Pressed Samples	41
4.4.2	Slip Cast Samples	43
4.5	Effects of Processing on CTE	59
4.5.1	Dry Pressed Samples	59
4.5.2	Slip Cast Samples	62
4.6	Effects of Processing on MOR	68
4.6.1	Dry Pressed Samples	68
4.6.2	Slip Cast Samples	70
5.	DISCUSSION	80
5.1	Effects of Processing on CMZP Ceramics	80
5.1.1	Sintering Temperature	80
5.1.2	Sintering Time	80
5.1.3	ZnO Additions	81
5.2	The Significance of the Minimum Mean ALPHA Temperature with Respect to ZnO Additions	81
5.3	The Relationships Between Bulk Density, MOR, and CTE	83
5.4	The Consequences of Using ZnO as a Sintering Aid	86
6.	CONCLUSIONS	91
7.	RECOMMENDATIONS	93
	REFERENCES	94
	APPENDIX	97
	VITA	100

LIST OF TABLES

Table 3.1	Processing Conditions for Dry Pressed Disks	15
Table 3.2	Processing Conditions for Slip Cast Tubes	15
Table 4.1	Decline in Zr Phosphate Peak Intensity with Temperature	20
Table 4.2	Decline in Zr Phosphate Peak Intensity with Temperature and ZnO	23
Table 4.3	Bulk Densities of Dry Pressed Samples	39
Table 4.4	Bulk Densities of Slip Cast Samples	41
Table 4.5	CTE Values of Dry Pressed Samples	59
Table 4.6	CTE Values of Slip Cast Samples	66
Table 4.7	MOR Values of Dry Pressed Samples	68
Table 4.8	MOR Values of Slip Cast Samples	70
Table 5.1	Summary of Physical Property Data versus Processing	84

LIST OF FIGURES

Figure 2.1 The NZP crystal structure	5
Figure 4.1 XRD patterns of CMZP without ZnO fired to: a) 910°C and b) 1040°C	21
Figure 4.2 XRD patterns of CMZP without ZnO fired to: a) 1170°C and b) 1300°C	22
Figure 4.3 XRD patterns of CMZP with 2.7 wt% ZnO fired to: a) 910°C and b) 1040°C	24
Figure 4.4 XRD patterns of CMZP with 2.7 wt% ZnO fired to: a) 1170°C and b) 1300°C	25
Figure 4.5 XRD patterns of CMZP with 2.7 wt% ZnO fired to 1260°C for: a) 0.33h and b) 1h	27
Figure 4.6 XRD patterns of CMZP with 2.7 wt% ZnO fired to 1260°C for: a) 4h and b) 12h	28
Figure 4.7 Dilatometric sintering profiles of dry pressed CMZP with and without 2.7 wt% ZnO	29
Figure 4.8 Dilatometric sintering profile of dry pressed CMZP with 2.7 wt% ZnO fired to 1260°C for 4h	30
Figure 4.9 Dilatometric sintering profile of slip cast CMZP with 2wt% ZnO	32
Figure 4.10 Dilatometric sintering profile of slip cast CMZP with 2 wt% ZnO fired to 1175°C for 2h	33
Figure 4.11a SEM fracture surface micrograph of CMZP with 2.7wt% ZnO fired to 1040°C for 0.33h at: a)2kX and b) 5kX	34
Figure 4.11b SEM micrograph of -400 CMZP powder at 6kX	34
Figure 4.12a SEM fracture surface micrograph of CMZP with 2.7wt% ZnO fired to 1105°C for 0.33h	35

Figure 4.12b SEM fracture surface micrograph of CMZP with 2.7wt% ZnO fired to 1170°C for 0.33h	35
Figure 4.13a SEM fracture surface micrograph of CMZP with 2.7wt% ZnO fired to 1235°C for 0.33h	36
Figure 4.13b SEM fracture surface micrograph of CMZP with 2.7wt% ZnO fired to 1300°C for 0.33h	36
Figure 4.14 RS1 generated bulk density contour plots for dry pressed samples	40
Figure 4.15a Micrograph of dry pressed sample (1) at 240X	42
Figure 4.15b Micrograph of dry pressed sample (1) at 2.5kX	42
Figure 4.16a Micrograph of dry pressed sample (A) at 240X	44
Figure 4.16b Micrograph of dry pressed sample (B) at 240X	44
Figure 4.17 Micrographs of dry pressed sample (AB) at: a) 240X and b) 600X	45
Figure 4.18 Micrographs of dry pressed sample (-400) at: a) 240X and b) 2.5kX	46
Figure 4.19 Micrographs of dry pressed sample (0.5B) at: a) 240X and b) 2.4kX	47
Figure 4.20 Micrographs at 240X of dry pressed samples: a) sample (C) and b) sample (AC)	48
Figure 4.21 Micrographs at 240X of dry pressed samples: a) sample (BC) and b) sample (ABC)	49
Figure 4.22 Micrographs of slip cast sample with 1wt% ZnO fired to 1250°C for 0.5h	51
Figure 4.23 Micrographs of slip cast sample with 1 wt% ZnO fired to 1250°C for 4h	52
Figure 4.24 Micrographs of slip cast sample with 1 wt% ZnO fired to 1300°C for 0.5h	53
Figure 4.25 Micrographs of slip cast sample with 1 wt% ZnO fired to 1300°C for 4h	54

Figure 4.26a Micrograph of slip cast sample (12-1) at 240X	55
Figure 4.26b Micrograph of slip cast sample (12-1) at 4.9kX	55
Figure 4.27a Micrograph of slip cast sample (12-4) at 240X	57
Figure 4.27b Micrograph of slip cast sample (12-4) at 4.6kX	57
Figure 4.28 Micrographs of slip cast sample (12-14) at: a) 4.5kX and b) 10.5kX	58
Figure 4.29 RS1 generated CTE contour plots for dry pressed samples	61
Figure 4.30 Thermal expansion plots to 1000°C for dry pressed samples: a) sample (C) and b) sample (ABC)	63
Figure 4.31 Thermal expansion plot to 1000°C for dry pressed sample (1)	64
Figure 4.32a Thermal expansion plot to 1000°C for dry pressed sample (0.5B)	65
Figure 4.32b Thermal expansion plot to 1000°C for dry pressed sample (-400)	65
Figure 4.33a Hysteresis plot to 1000°C of slip cast sample (12-1)	67
Figure 4.33b Hysteresis plot to 1000°C of slip cast sample (12-4)	67
Figure 4.34 RS1 generated MOR contour plots for dry pressed samples	69
Figure 4.35 MOR bar fracture surface micrographs of dry pressed samples: a) sample (-400) and b) sample (0.5B)	71
Figure 4.36 MOR bar fracture surface micrographs of dry pressed samples: a) sample (1) and b) sample (A)	72
Figure 4.37 MOR bar fracture surface micrographs of dry pressed samples: a) sample (B) and b) sample (AB)	73
Figure 4.38 MOR bar fracture surface micrographs of dry pressed samples: a) sample (C) and b) sample (AC)	74
Figure 4.39 MOR bar fracture surface micrographs of dry pressed samples: a) sample (BC) and b) sample (ABC)	75
Figure 4.40 MOR bar fracture surface micrographs of slip cast sample (12-1)	77

Figure 4.41 MOR bar fracture surface micrographs of slip cast sample (12-4)	78
Figure 4.42 MOR bar fracture surface micrographs of slip cast sample (12-14)	79
Figure 5.1a MOR bar fracture surface micrograph of slip cast sample (12-14) after thermal aging for 100h at 800°C	87
Figure 5.1b MOR bar fracture surface micrograph of slip cast sample (12-14) after thermal aging for 100h at 1000°C	87
Figure 5.2 MOR bar fracture surface micrographs of slip cast sample (12-14) after thermal aging for 100h at 1200°C	88
Figure 5.3a MOR bar fracture surface micrograph of slip cast sample (12-4) after thermal aging for 100h at 800°C	89
Figure 5.3b MOR bar fracture surface micrograph of slip cast sample (12-4) after thermal aging for 100h at 1000°C	89
Figure 5.4 MOR bar fracture surface micrographs of slip cast sample (12-4) after thermal aging for 100h at 1200°C	90

1. INTRODUCTION

Before a new material can be successfully utilized as an engineering material, a processing method must be developed. For a ceramic material such as $(\text{Ca}_{0.6}\text{Mg}_{0.4})\text{Zr}_4(\text{PO}_4)_6$ (CMZP), this process includes synthesis, batching, forming, drying, and sintering to obtain parts of desired shape and physical properties. This research focused on the sintering of CMZP ceramics, which included time, temperature, and level of ZnO sintering aid to obtain a modulus of rupture (MOR) greater than 90 MPa while maintaining a positive coefficient of thermal expansion (CTE) for potential application as insulated diesel exhaust port liners in the next generation diesel engines produced by Caterpillar Inc. (Peoria, Ill.). These liners will reduce heat loss and therefore increase efficiency and reduce emissions.

The use of thermal insulation to increase overall efficiency of internal combustion engines, which translates into lower operating costs, has long been recognized and remains a primary focus of combustion engine research. Given that an average ten year engine investment approaches one million dollars, of which 82% is fuel cost¹, any increase in fuel efficiency is considered significant. This increase in efficiency is a result of less heat loss to cooling and better exhaust energy utilization.

In 1980, heat rejection accounted for about 28% of the efficiency for a typical diesel engine. By 1994, this figure was reduced to 26%. However, future goals place heat rejection at 16%¹, a reduction possible only through use of insulating materials such as CMZP. Additionally, less heat loss results in smaller cooling system requirements which allows the packaging of higher horsepower engines into more compact, streamlined designs.

Aluminum titanate [AlTiO₄] and NZP [NaZr₂(PO₄)₃] are two other potential candidate materials for use as exhaust port liners. However, CMZP offers higher strength and improved abrasion resistance and the thermal properties and Young's modulus of CMZP also make it easier to cast-in-place. Moreover, CMZP ceramic may present an alternative to ZrO₂, which is the standard commercial thermal insulation. CMZP exhibits a thermal conductivity less than one-half that of ZrO₂; therefore less material is needed to achieve the same degree of thermal insulation. Furthermore, CMZP is substantially lighter and less expensive, two major factors that make CMZP a very appealing choice over ZrO₂, especially as an engine component, where lighter means more efficient.

This study emphasized the inter-relationship of processing, microstructure, and properties so as to optimize the sintering conditions of CMZP ceramics to obtain high strength and a low, positive thermal expansion. Initial relationships were resolved via an in-depth sintering study using dry pressed samples in a 2-level factorial experimental design. These fundamental relationships were then applied to slip cast samples resulting in a high strength, low thermal expansion material. This research was conducted at Caterpillar's Technical Center in the Advanced Materials Technology Division.

This research is actually a re-investigation of the synthesis, sintering, and thermal expansion work presented by T.K. Li et al²⁴ for dry pressed sol-gel and solid-state reacted powders which focused on the effects of time and temperature on grain size and thermal expansion. However, a new solid-state reaction method for synthesizing CMZP demanded an evaluation of the sintering parameters for the new powder. Furthermore, MOR testing, including correlation with microstructure, needed to be performed for this new powder since the only mechanical property data that existed was for hot-pressed sol-gel powder presented by W. Russ.³⁰ Because slip casting

is a cost-effective process for producing complex shapes, a slip casting process was developed for this new powder so thermal and mechanical properties, along with microstructures, could be obtained. This investigation of CMZP was necessary to show that CMZP could be processed to meet the design criteria for exhaust port liners and to prove CMZP's competitiveness with $AlTiO_4$ and NZP.

2. LITERATURE REVIEW

2.1 Background of $(\text{Ca}_{0.6}\text{Mg}_{0.4})\text{Zr}_4(\text{PO}_4)_6$ [CMZP]

2.1.1 General Overview

CMZP is a member of the $\text{NaZr}_2(\text{PO}_4)_3$ [NZP] structural group of ceramic materials known for their open but rigid crystal structure and low thermal expansion.^{2,3,4,5} Substitution of Group I and II cations into the sodium position is possible due to the large number of interstitial positions in the crystal structure and the ability of the structure to distort to accommodate different size cations.^{4,6,7,8,9,10,11,12,22} These substitutions also allow the thermal expansion behavior of the material to be compositionally controlled. CMZP is one of these compositional derivatives of the NZP structure that exhibits low coefficient of thermal expansion, low thermal conductivity, and good thermal and chemical stability.^{13,14,20,24,30} These properties make CMZP an appealing material for high temperature applications such as thermal barriers, filtration media, substrate supports, and structural ceramics.

2.1.2 Crystal Structure

The crystal structure of NZP (Figure 2.1) was determined by Hagman and Kierkegaard³ in 1968. NZP was indexed as having a hexagonal unit cell consisting of six formula units, totaling 108 atoms, and possessing R3c space group symmetry. The crystal structure is composed of strongly bonded corner sharing ZrO_6 octahedra and PO_4 tetrahedra in a three-dimensional framework. Each ZrO_6 octahedra is connected to six PO_4 tetrahedra and each PO_4 tetrahedra is connected to four ZrO_6 octahedra. Chains of face-sharing ZrO_6 and NaO_6 octahedra, joined together by PO_4 tetrahedra, make up the basic structure.

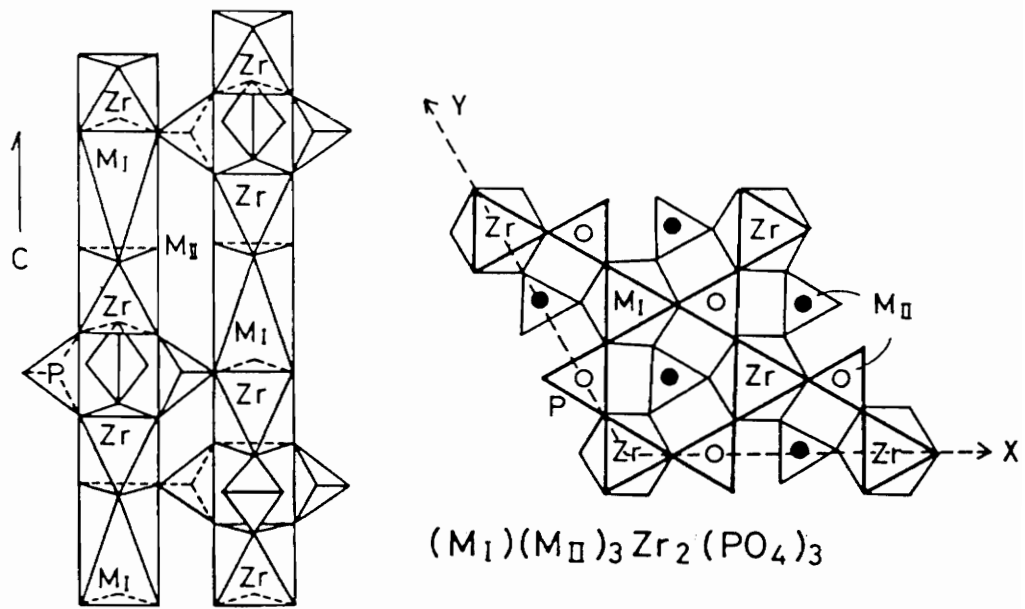


Figure 2.1 The NZP crystal structure⁸

The result of this open framework is four interstitial positions per formula unit, three octahedral sites and one prismatic site.^{3,9} The octahedral sites (M') are highly distorted and are formed by the triangular faces of two ZrO_6 octahedra that are mutually linked by PO_4 tetrahedra in such a way that empty trigonal prisms of oxygen atoms are formed.⁸ The prismatic sites (M'') are located in between the ZrO_6 octahedral chains midway between the two PO_4 tetrahedra.

2.1.3 Effects of Composition

The near zero CTE values of NZP-type structures are due to anisotropic thermal expansion in the **a** and **c** crystallographic directions, which is compositionally influenced.^{8,9,10} The structure is very adaptive to ionic substitutions due to the flexibility of the skeletal network, the strength of the bonds, and the existence of interstitial holes. Alamo and Roy⁹ observed the following NZP lattice reactions to cation substitutions: (1) the skeleton can modify itself to accommodate small as well as large cations in M' holes, (2) in order to increase the size of the M' holes, this flexible skeleton contracts in the **a** direction and expands in the **c** direction, and (3) in order to accommodate extra ions in the M'' holes, the skeleton contracts in the **c** direction and expands in the **a** direction. Therefore, with M' substitutions, the **c** parameter increases and the **a** parameter decreases with increasing ion size. Furthermore, the oxygen atoms in the structure tend to move away from the interstitial cations with increasing temperature, enlarging the M' interstitial cavity by an increase in the **c**-axis and a decrease in the **a**-axis.¹⁰ For M'' substitutions, which lie between the ZrO_6 octahedra chains, the lattice expands in the **a** direction, causing the M' holes to contract, forcing the ion out of position, allowing the structure to distort into a monoclinic structure with a simultaneous decrease in the **c**-axis.⁹ These changes in lattice parameters due to cation substitutions parallel the changes caused by temperature and account for the near zero CTE values for these structures.

2.2 Sintering and Densification

2.2.1 General Summary of Sintering Process

Once a product has been formed and dried, traditionally referred to as “green”, a heat treatment or “firing” is needed to develop the microstructure and desired properties.²⁵ During this heat treatment, sintering takes place, which is the removal of interparticle porosity from the starting compact accompanied by shrinkage and strong bonding between the particles.¹⁵ The possible changes that can occur during sintering include increases in grain size, changes in pore shape, size, and number, formation of new phases, polymorphic transformations, and decomposition of crystalline compounds.²⁷

In order for sintering to occur, there must be a mechanism for material transport and a source of energy to activate and sustain this mechanism. The three main sintering processes include solid state, liquid phase, and vapor phase. Solid state sintering is driven by free energy or chemical potential differences between the neck and the particle surface and include diffusional mechanisms such as surface, boundary, and lattice diffusion.^{15,25} Boundary and lattice diffusion are both densification mechanisms that promote both neck growth and volume shrinkage. Surface diffusion, however, does not yield volume shrinkage but does produce surface smoothing, particle joining, and pore rounding.²⁵ Liquid phase sintering also promotes densification and is driven by capillary pressure and surface tension in the presence of a wetting agent.^{15,25} Finally, vapor phase sintering, which does not result in volume shrinkage, is driven by evaporation-condensation mechanisms which produce the same effects as surface diffusion. The sintering of CMZP ceramics

is controlled by solid state mechanisms with liquid phase contributions when a sintering aid such as ZnO is used.²⁴

The sintering process can be broken down into three main stages typically referred to as the first or initial stage, the second or intermediate stage, and the third or final stage.^{15,25} During the initial stage, there is a rearrangement of particles accompanied by surface smoothing, grain boundary and interparticle neck formation, and the rounding of interconnected, open pores. Neck formation or bonding occurs at points of contact where material transport can occur and surface energy is high.¹⁵ Porosity decreases are less than 12% during the first stage of sintering.

The second or intermediate stage of sintering is marked by neck and grain growth and high shrinkage.^{15,25} The centers of the particles begin to move together resulting in significant shrinkage, which accounts for the decrease in porosity. Grain boundary movement promotes grain growth which can result in the elimination of smaller grains and porosity being trapped at the grain boundaries. Intragranular porosity may also result when grain growth is rapid. The second stage is identified by a continuous pore phase and proceeds as long as the pore channels are interconnected. The end of the intermediate stage is the development of a non-interconnected, isolated pore structure.

The final or third stage of sintering is one of continued grain growth and the final removal of porosity which results in a discontinuous pore phase.^{15,25} Porosity is reduced or eliminated by vacancy diffusion along the grain boundary which is aided by grain boundary movement and controlled grain growth. During the final stage, two types of grain growth are possible, excessive and exaggerated. Excessive grain growth is an undesirable increase in the average grain size without a change in the grain size distribution; therefore, all of the grains are affected. Exaggerated grain growth, also known as discontinuous grain growth or secondary

recrystallization, is the preferential growth of some grains at the expense of a fine grain structure²⁷. This type of grain growth is generally exhibited by very large grains, sometimes rectangular, in a smaller grained matrix. Grain growth, both excessive and exaggerated, must be controlled to obtain maximum density.

2.2.2 The Driving Force for Sintering

The fundamental driving force for sintering is the minimization of total free energy which is accomplished through grain growth.^{15,25,27} Grain growth reduces the surface energy of the system by reducing the grain boundary area and by eliminating solid-vapor interfaces, resulting in new, but lower energy solid-solid interfaces. The free energy difference across a curved grain boundary, which is proportional to particle size, is described as:

$$\Delta G = \gamma V(r_1^{-1} + r_2^{-1}) \quad \text{where } \begin{array}{l} \gamma = \text{boundary energy} \\ V = \text{molar volume} \\ r_1, r_2 = \text{principle radii of curvature} \end{array}$$

The minimization of ΔG is the driving force that makes grain boundaries move toward their center of curvature. Grains with fewer than six sides tend to shrink and grains with more than six sides tend to grow since it is observed in 2-D that these two types of grains have convex and concave boundaries, respectively. The growth of concave boundaries is due to the fact that there is a greater concentration of vacancies beneath a flat or concave surface which results in the transport of vacancies by diffusion from the concave surface with a simultaneous flow of atoms in the opposite direction.²⁵

2.2.3 Solid State Sintering

As stated previously, differences in free energy or chemical potential between the interparticle neck and the particle provide the driving force for material transport in diffusional processes. Matter can move from the surface, bulk, or grain boundary to the neck by surface, lattice, or grain

boundary diffusion, respectively. However, only transfer of matter results in shrinkage and pore elimination.²⁷ Surface diffusion only affects neck diameter, not shrinkage or porosity.

A model for lattice diffusion to the neck region from line contact between two adjacent particles^{16,17} can be described as follows:

$$\Delta L/L = \{(K\gamma a^3 Dt)/(kT d^n)\}^m$$

where L = distance between particle centers

K = geometric constant

γ = surface energy

a^3 = atomic volume of diffusing vacancy

D = self-diffusion coefficient

t = time

k = Boltzman constant

T = temperature

d = particle diameter

m,n = constants dependent on type of mass transport

This model is most valid at the intermediate or second stage of sintering when neck growth is prominent but does not account for grain growth and changes in pore geometry (diffusing vacancy). From this model, particle size and temperature are proven to be the two major factors influencing shrinkage with time being less important. The effect of temperature is further increased due its exponential relationship with the diffusion coefficient.¹⁵ The effect of time is mainly that of grain growth which does not aid in densification.

2.2.4 Liquid Phase Sintering

A sintering aid which introduces a liquid phase at temperature can be added to a ceramic to enhance and activate densification during sintering, allowing the compact to be sintered to a higher density at a lower temperature.²⁵ The liquid located between the grains draws the particles together by capillary pressure, thereby providing a driving force for densification. This liquid, which may be as little as 1 vol%, allows angular particles to rotate, enabling particles to slide and rearrange into a denser configuration. Additionally, a liquid phase can enhance sintering because

high local stresses at contact points lead to plastic creep and deformation, smaller particles dissolve in the liquid phase allowing material transfer to larger particles, and increased pressure at the contact points results in increased solubility such that material is transferred away from the contact areas allowing the particle centers to approach.²⁷ Finally, a liquid phase has been shown to rapidly penetrate between grains and disperse aggregates.¹⁸

Factors affecting liquid phase sintering include the solubility of the solid in the liquid, the wetting of the solid by the liquid, and the diffusivity of material through the liquid.²⁵ A fine particle size of the solid is also needed to develop the necessary capillary pressures since capillary pressure is inversely proportional to grain size.²⁷ Furthermore, sintering with a reactive liquid phase may promote the solution and reprecipitation of solids for improved densification. However, reactive liquids may also complicate sintering by encouraging excessive or exaggerated grain growth.

2.3 Microcracking of Anisotropic Materials

2.3.1 The Formation of Microcracks

Microcracks are the result of microstresses produced in a material during cooling by anisotropic crystallographic expansions and crystallographic misorientations across grain boundaries.^{28,29} The stored elastic strain energy of thermal expansion anisotropy is converted directly to fracture surface energy, commonly resulting in microcracks in large grained materials. Cleveland and Bradt²⁹ proposed the existence of a critical grain size which allows spontaneous microcracking in anisotropic materials. This grain size, G_{crit} , marks a sharp transition from a fine grained, high strength material to a weak, large grained, severely microcracked material. The

formation of microcracks is evidenced by significant reductions in elastic modulus and flexural strength, intergranular fracture, and pronounced thermal hysteresis upon cooling. The critical grain size was determined to be inversely proportional to the square of $\Delta\alpha_{\max}$, which is the maximum difference in thermal expansion between two crystallographic directions.

Yamai and Oota³¹ proposed the existence of two critical transition grain sizes. The first transition grain size produces narrow microcracking which is responsible for the reductions in elastic modulus and flexural strength and is focused primarily at the grain boundaries, which are the typically the weakest parts of the ceramic body. The second transition grain size produces wide microcracking, evidenced as intragranular microcracks, and affects the thermal response of the material. The second transition grain size is the release of high stress within the grains.

2.3.2 The Effects of Microcracking on Thermal Expansion

Microcracking may be responsible for anomalous thermal expansion behavior such as zero or negative CTE and pronounced hysteresis.^{8,28,31,32} Small grained materials below G_{crit} exhibit no thermal hysteresis and have CTE values near that of the average of the crystallographic axes while large grained materials above G_{crit} exhibit considerable hysteresis and extremely low CTE values. These differences are explained by the spontaneous formation of inter- and intra- granular microcracks above G_{crit} .

Crack healing of microcracked ceramic materials upon heating is the cause of the lower than expected CTE values and thermal expansion hysteresis¹⁹. The positive thermal expansion of the material is absorbed by the microcracks and results in crack healing rather than a change in sample size. For a material like CMZP²⁴, small, narrow crack healing results in near zero or negative thermal expansions at low temperatures due to the positive expansion along the **c**-axis being absorbed by microcrack healing, allowing the negative expansion along the **a**-axis to

dominate. At higher temperatures, the microcracks are completely healed and the positive expansion along the **c**-axis contributes to the overall expansion. On the other hand, wide microcracks completely absorb the **c**-axis expansion over a much wider temperature range resulting in negative CTE values.

3. EXPERIMENTAL PROCEDURE

3.1 Dry Pressed Samples

Disks were dry pressed from CMZP powder obtained from Material Technologies of Virginia (MATVA) calcined to 600°C and screened to -100 mesh. After screening to -400 mesh, small batches of CMZP (approximately 70 g) and ZnO were ball milled in Nalgene jars with 4.8 mm (3/16") zirconia media for 2-4 h, which resulted in a reproducible mean particle diameter (MPD) of approximately 4 μm . After the addition of 14 wt% binder (5% polyvinyl alcohol [PVA] solution), the samples were pressed in a 76mm (3") diameter steel die for 0.25 h at 6 MPa (875 psi). After allowing to dry overnight at 60°C, the disks were fired at 2°C/min. to 600°C, 10°C/min. to temperature for the desired time, then cooled at 10°C/min. to room temperature. The disks were then machined into MOR bars by Chand Kare Technical Ceramics (Worcester, MA) per MIL-STD-1942A Size B.

A simple 2-level factorial experimental design was constructed to determine the effects of TIME (0.5 and 4 h), TEMPERATURE (1250 and 1300°C), and %ZnO (1 and 3 wt%) on bulk density, CTE, and MOR. These levels were selected after preliminary research involving bulk density optimization, as outlined in the Appendix. Two additional samples outside the main matrix were also tested for a total of ten dry pressed conditions. A VAX based RS1 program was used for statistical analysis, assuming quadratic relationships. Table 3.1 outlines the processing conditions for each sample.

Table 3.1 Processing Conditions for Dry Pressed Disks

Sample ID	TIME	TEMPERATURE	wt%ZnO
(I)	0.5 h	1250°C	1.0%
(A)	4 h	1250°C	1.0%
(B)	0.5 h	1300°C	1.0%
(AB)	4 h	1300°C	1.0%
(C)	0.5 h	1250°C	3.0%
(AC)	4 h	1250°C	3.0%
(BC)	0.5 h	1300°C	3.0%
(ABC)	4 h	1300°C	3.0%
(0.5B)	0.5 h	1300°C	0.5%
(-400)	8 h	1300°C	0%

3.2 Slip Cast Samples

Straight tubes with an outside diameter of 28mm, a length of 70mm, and a wall thickness of 4-6mm (finished dimensions) were slip cast using a proprietary process developed by Caterpillar which produced slips having sub-micron particle sizes. These slips were a 45 to 55 weight percent ratio of CMZP powder to distilled/deionized (D/DI) water. Using plaster molds with a 1.41 weight ratio of plaster-to-water, casting times ranged from 0.67 to 1 h. The tubes were fired at 2°C/min. to 600°C, 7°C/min. to temperature for the desired time, then cooled at 10°C/min. The tubes were then machined into MOR bars by Chand Kare Technical Ceramics (Worcester, MA) per MIL-STD-1942A Size B. Table 3.2 outlines the processing conditions of the slip cast tubes.

Table 3.2 Processing Conditions for Slip Cast Tubes

Sample ID	Slip Ratio	Time	Temperature	%ZnO
(12-1)	45/55	0.5 hours	1200°C	2%
(12-4)	45/55	0.7 hours	1175°C	2%
(12-14)	45/55	0.5 hours	1200°C	1.5%

The same slip casting technique was used to produce small disks for microstructural analysis. These samples were processed with 1.0wt% ZnO and fired to 1250°C and 1300°C for 0.5 h and 4 h.

3.3 X-ray Diffraction Samples

To determine the effects of time, temperature, and ZnO level on X-ray diffraction (XRD) patterns, 25.4 mm (1") disks were pressed using -400 mesh CMZP powder with 15 wt% binder (5% PVA solution) at 24.8 MPa (3.6 ksi) for 5 minutes. The same mixing procedure described in Section 3.1 was used. The disks were allowed to dry overnight at 60°C then fired at 2°C/min. to 600°C and 10°C/min. to 1300°C. During the second furnace ramp, samples with and without 2.7wt% ZnO were removed from the furnace and water quenched starting at 715°C and then every 65°C after with a 0.33 h soak at each desired temperature. The ramp rate of 10°C/min. was maintained between temperatures. Another set of 25.4 mm (1") disks with 2.7 wt% ZnO was fired to 1260°C, removed from the furnace and air cooled after 0.33, 1, 4, and 12 h at temperature. Finally, to better identify the secondary phases, samples with 6 and 9 wt% ZnO were fired to 1250°C for 0.33 h and air-cooled. All XRD samples were scanned from 10-50° 2- θ at Caterpillar using a Nicolet diffractometer with Cu K $_{\alpha}$ radiation.

3.4 Bulk Density

All bulk density measurements were performed at Caterpillar using a Micromeretics Autopore II Model 9220 Mercury Porosimeter. Samples were pieces of an MOR bar sized to fit the penetrometer.

3.5 Dilatometric Studies

Sintering studies were performed on a Theta Dilatronic Dilatometer using a large displacement (10 mm) dual pushrod LVDT, a single crystal sapphire reference, and alumina pushrods and sample holder. Samples were approximately 5 mm in length and were either pressed at 4.45 kN (1000 lbs.) in a 6 mm diameter die or cut directly from an unfired sample. Samples were heated at 5°C/min. to the desired temperatures. Specimen expansion and Mean ALPHA were calculated by a Theta supplied Lotus macro.

CTE of sintered samples was measured using a small displacement (1 mm) dual pushrod LVDT with the same dilatometer and sample setup as previously described. The measuring head was rated for less than 1% error. MOR bars cut to 25 mm were used as samples and were tested to 1000°C at 5°C/min. Average CTE was obtained by using the value of Mean ALPHA at the desired temperatures of 700 and 1000°C.

Mean ALPHA, calculated in real time by the Theta macro, is actually an instantaneous CTE. This value is obtained by dividing the change in sample length by the temperature range at that given temperature. That is,

$$\text{Mean ALPHA} = \Delta L / \Delta T = (L_t - L_0) / (T - T_0)$$

where L_0 and T_0 are the initial length and temperature, respectively, and L_t is the sample length at the temperature T . Therefore, the Mean ALPHA value at a given temperature is the average CTE to that temperature. The Mean ALPHA label is used to distinguish the sintering study data from the thermal response (CTE) data.

Hysteresis plots, which show thermal response during heat up and cool down, were produced using a cooling rate of $5^{\circ}\text{C}/\text{min}$. from 1000°C on selected samples. These plots show the existence of any anisotropic thermal expansion response upon cooling, which is an indication of microcracking.

3.6 MOR Analysis

MOR bars, sample size of 6 to 9, were broken in 4-pt bending per MIL-STD 1942A using a JJ Tensile Testing Machine Type T5003. Tensile machine output was gathered by a PC and analyzed using a Caterpillar in-house RS1 computer program which calculated Average MOR and Standard Deviation. All MOR testing was performed at Caterpillar.

3.7 Particle Size Analysis

Particle size analysis was performed on a Horiba CAPA-700 Particle Size Analyzer operated at 960 rpm/minute. Powder samples were dispersed in D/DI water with 3 drops of sodium pyrophosphate and ultrasonically mixed for 1 minute. Slip samples were diluted with D/DI water to obtain the desired absorbance. All reported data is the average of at least 3 runs.

3.8 Micrographs

Optical micrographs of polished/thermally etched samples were obtained using an Olympus PMG3 reflecting light microscope. Scanning Electron Microscope (SEM) micrographs of polished/thermally samples and fracture surfaces were produced using a Cambridge Stereoscan 260 SEM at Caterpillar. Samples for SEM analysis were carbon coated before being analyzed. Samples were thermally etched at 50-100°C below their sintering temperatures for 30-60 minutes. The SEM was also used for Energy Dispersive Spectroscopy (EDS) analysis of grain and grain boundary compositions.

Additional micrographs of fracture surfaces of thermally aged samples were performed at Virginia Tech using an ISI-SX-40. The fracture surfaces of these thermally aged samples were gold coated before analysis.

3.9 Thermal Aging of Slip Cast Samples

Slip cast samples (12-4) and (12-14) were thermally aged at 800, 1000, and 1200°C for 100 h to determine the effect of long term exposure to temperature.

4. RESULTS

4.1 X-ray Diffraction

4.1.1 Effects of Temperature

For CMZP samples without ZnO, XRD peak analysis proved that the composition was a mixture of CMZP and zirconium phosphate (ZrP_2O_7). Given that the material supplied was calcined only to 600°C, unreacted zirconium phosphate is present since solid-state synthesized CMZP does not begin to crystallize until temperatures greater than 1100°C²⁰. For the temperature range of 845 to 1300°C, samples exhibited a steady decrease in ZrP_2O_7 with temperature as seen by the decrease in the most intense peak (21.55° 2- θ) for ZrP_2O_7 (Figures 4.1 and 4.2). Table 4.1 shows this decline in zirconium phosphate peak intensity with temperature.

Table 4.1 Decline in Zr Phosphate Peak Intensity with Temperature

Temperature	Peak Intensity
845°C	220cps
910°C	190 cps
975°C	190 cps
1040°C	120 cps
1105°C	85 cps
1170°C	70 cps
1235°C	30 cps
1300°C	30 cps

This decrease is attributed to the conversion of ZrP_2O_7 to α - $Zr_2P_2O_9$, which in the presence of divalent cations such as calcium, crystallizes into $CaZr_4(PO_4)_6$ ²¹, or in the present case, CMZP. Therefore, in the absence of ZnO, the CMZP crystal structure develops as expected.

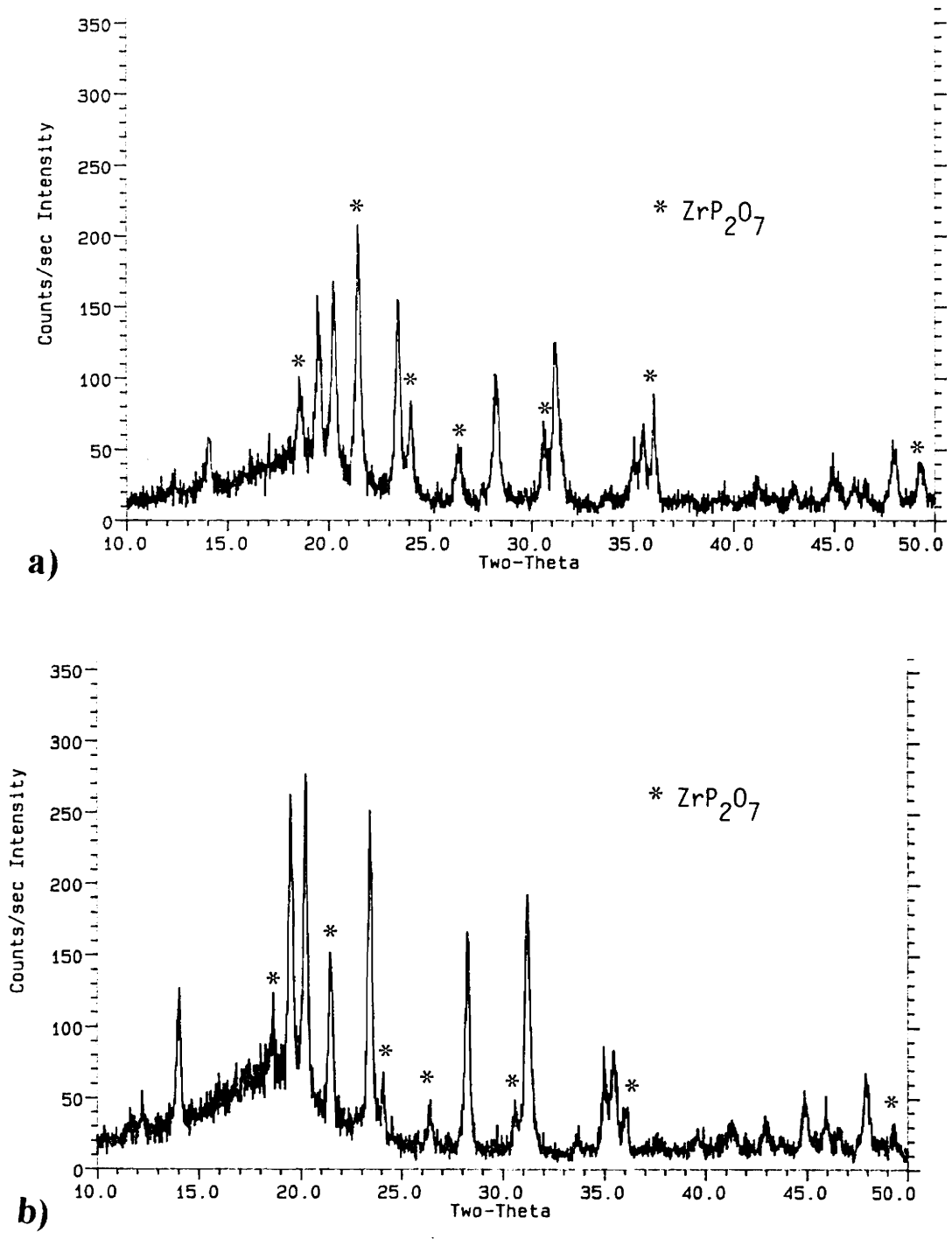


Figure 4.1 XRD patterns of CMZP without ZnO fired to: a) 910°C and b) 1040°C

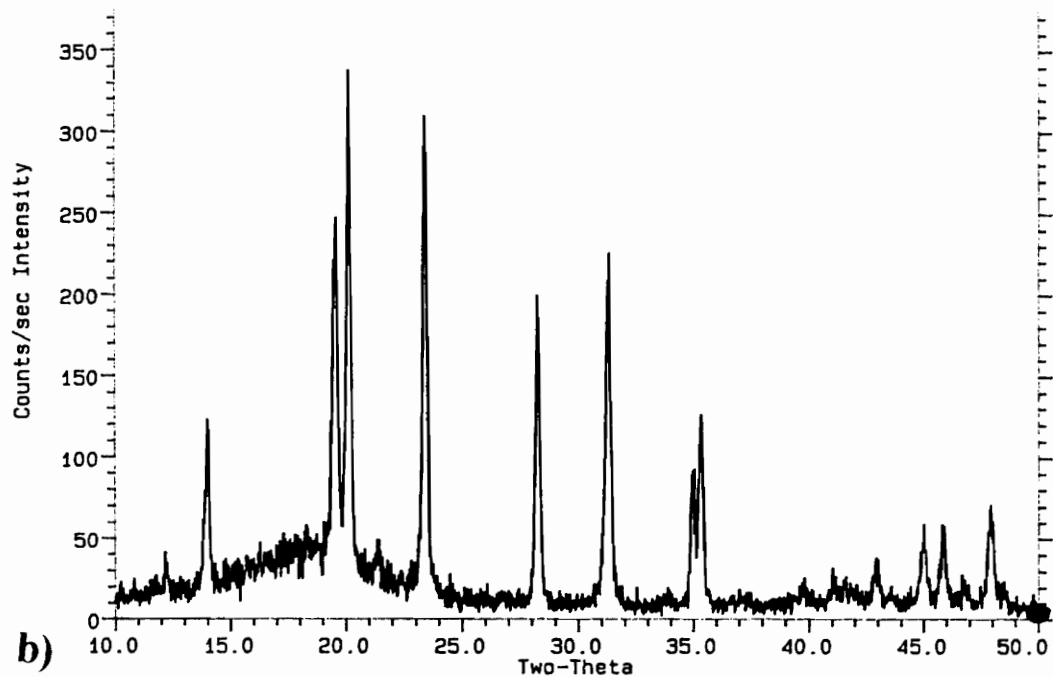
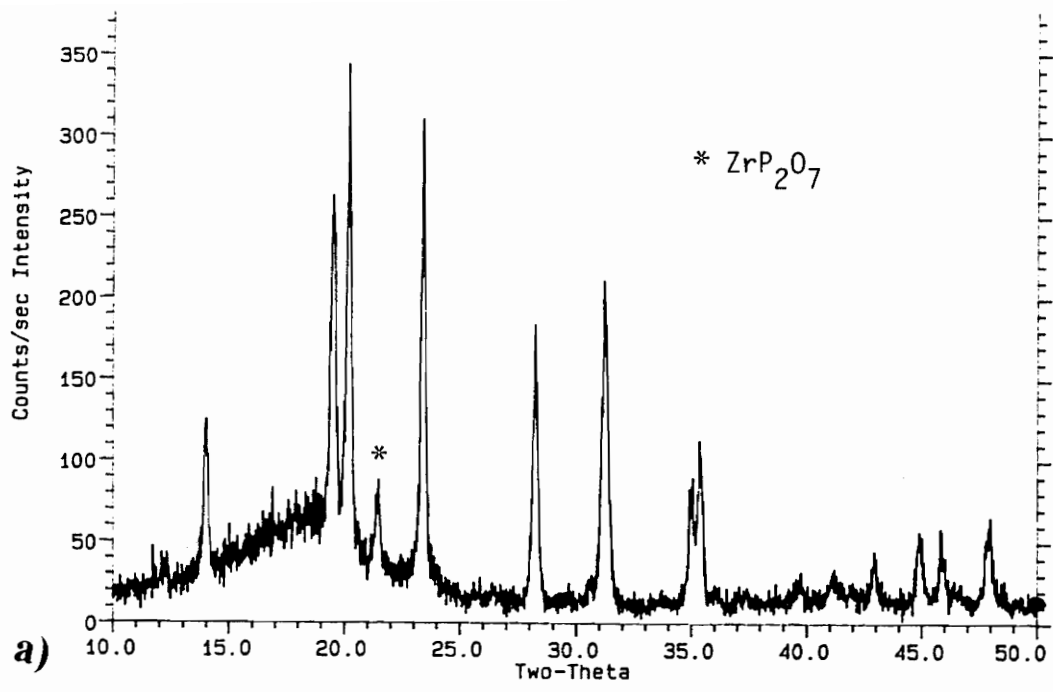


Figure 4.2 XRD patterns of CMZP without ZnO fired to: a) 1170°C and b) 1300°C

For samples fired with 2.7wt% ZnO, a similar decrease in ZrP_2O_7 intensity is seen, only more dramatically (Figures 4.3 and 4.4). Table 4.2 shows the decline in zirconium phosphate peak intensity with temperature when processed with 2.7wt% ZnO.

Table 4.2 Decline in Zr Phosphate Peak Intensity with Temperature and ZnO

Temperature	Peak Intensity
845°C	185 cps
910°C	135 cps
975°C	75 cps
1040 °C	45 cps
1105°C	30 cps
1170°C	30 cps
1235°C	0
1300°C	0

XRD peak analysis proved the formation of $ZnZr(PO_4)_2$, even at 845°C. This compound is the reaction product of ZnO and ZrP_2O_7 and is therefore responsible for the more dramatic decrease in ZrP_2O_7 intensity with temperature as compared to samples without ZnO.

ZnO also caused the formation of additional phases, starting around 1170°C. By 1235°C, the peaks of these new phases were slightly more defined and by 1300°C were very sharp and intense (Figure 4.4). Using higher ZnO content (6 and 9wt%) samples, these new peaks were identified as β - $Zr_2P_2O_9$, $ZnZr(PO_4)_2$, $Zn(PO_3)_2$, and $Zn_2Mg(PO_4)_2$. Given that only slight peak shifts in XRD patterns distinguish CMZP from $CaZr_4(PO_4)_6$ [CZP]²⁰, the presence of CZP is highly likely. The formation of Zn and (Zn,Mg) phosphates is consistent with previous work concerning the sintering of $Ca_{0.5}Zr_2(PO_4)_3$ ²². EDS analysis on samples with 3wt% ZnO fired to 1250 and 1300°C for 0.5 and 4 h exhibited Mg^{+2} deficient grains and Zn^{+2} , Mg^{+2} rich grain boundaries. For samples fired for 4 h, some Ca^{+2} was also present at the grain boundaries,

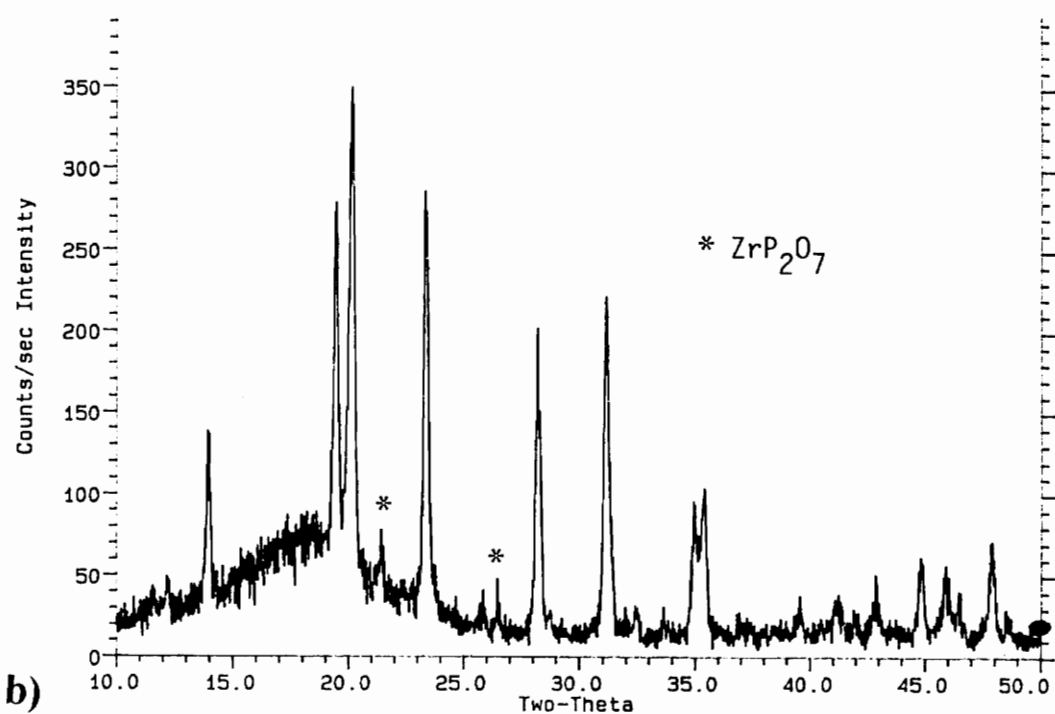
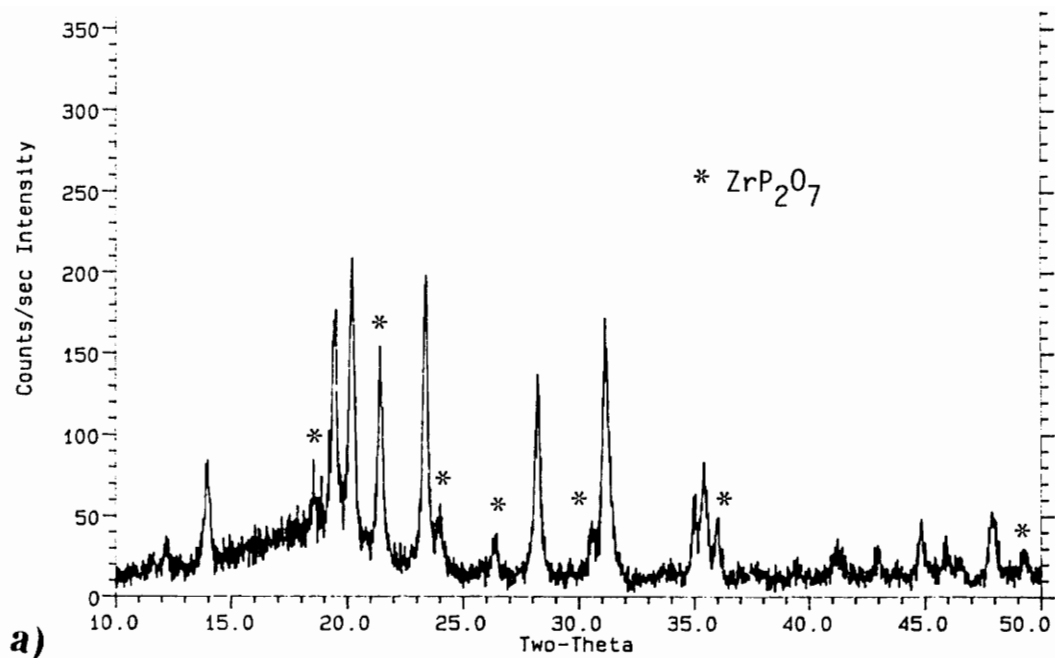


Figure 4.3 XRD patterns of CMZP with 2.7wt% ZnO fired to: a) 910°C and b) 1040°C

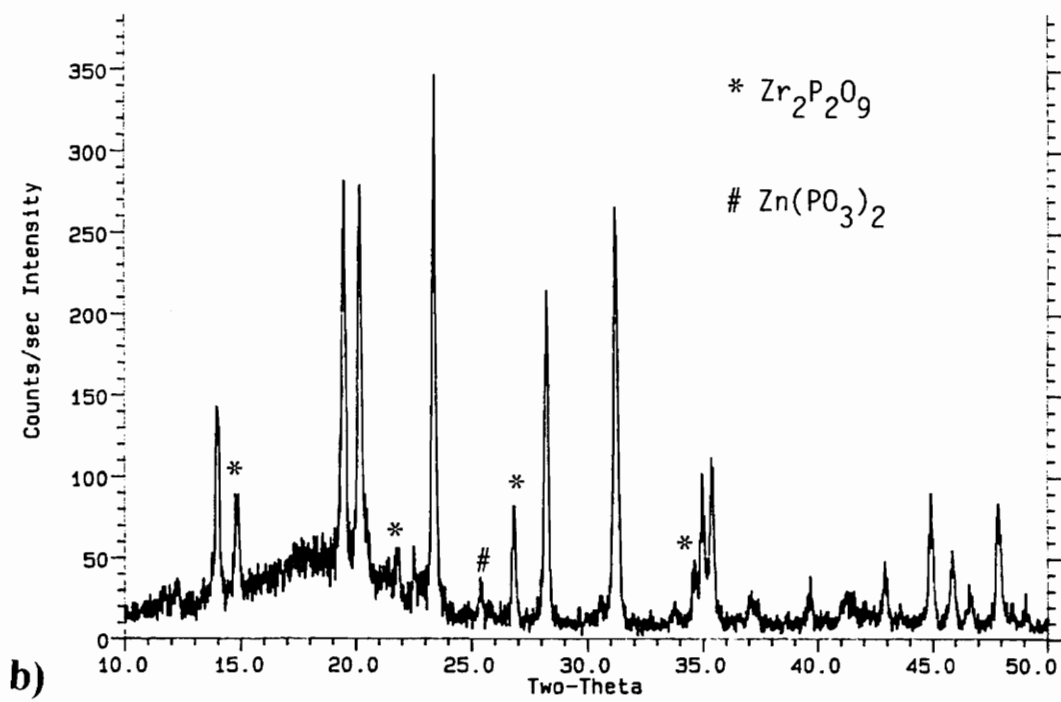
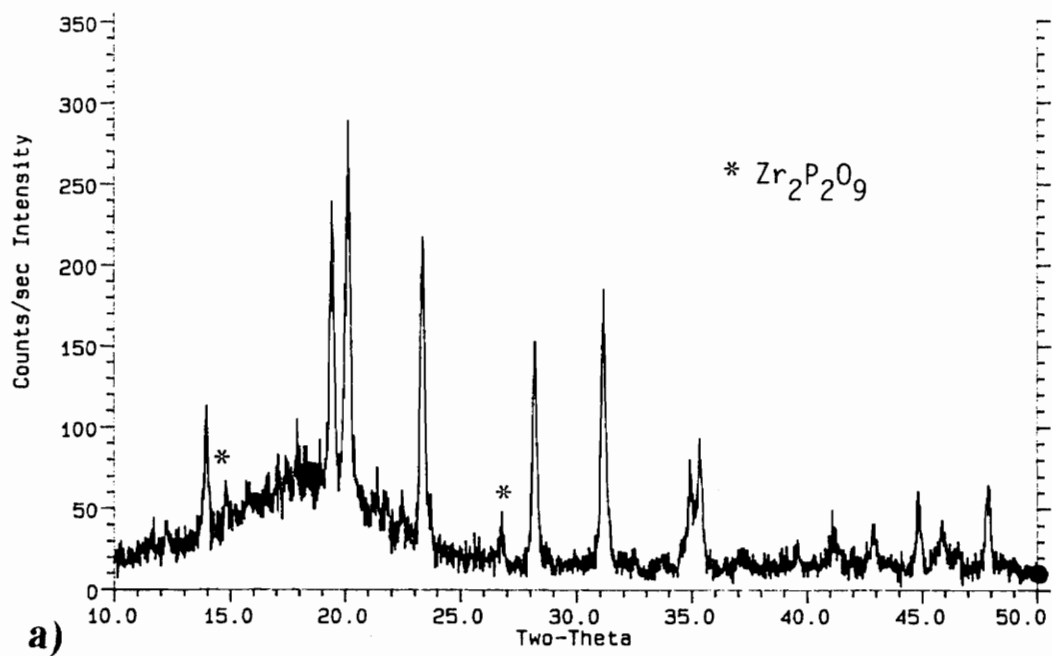


Figure 4.4 XRD patterns of CMZP with 2.7wt% ZnO fired to: a) 1170°C and b) 1300°C

especially at the 1300°C condition. A diffusional process is proposed since calcium is only found at the grain boundaries after extended firing times. No Zn^{+2} was present in the grains for any of the four conditions previously described.

4.1.2 Effects of Time

For CMZP samples fired to 1260°C with 2.7wt% ZnO, time had an effect on composition as evidenced by XRD patterns. No new peaks were formed for the time range of 0.33 to 12 h (Figures 4.5 and 4.6), therefore, all secondary phases form within the first 20 minutes of firing. However, the most intense peak for $\beta-Zr_2P_2O_9$ (26.8° $2-\theta$) became more intense as time progressed, especially after 12 h at temperature. Given that $\beta-Zr_2P_2O_9$ is the high temperature form of $\alpha-Zr_2P_2O_9$ ²³, which is the zirconium compound from which $CaZr_4(PO_4)_6$ [CZP] can be derived²¹, the intensity increase of this compound with time is reasonable, especially since Mg^{+2} is believed to migrate to and dissolve in the grain boundary phase(s)²⁴.

4.2 Effects of Processing on Densification

4.2.1 Dilatometric Studies

The effects of ZnO additions, temperature, and time on densification were determined using dilatometric data such as specimen expansion and Mean ALPHA. For -400 mesh CMZP powder, specimen shrinkage was only 6% when fired to 1350°C. During the ramp to 1350°C, a minimum Mean ALPHA temperature was seen at 1250°C. The addition of 2.7 wt% ZnO increased specimen shrinkage to 18% and pushed back the minimum Mean ALPHA temperature to 1225°C (Figure 4.7). For samples with 2.7 wt% ZnO, practically all sintering took place within the first 0.5 h at temperature with almost no additional shrinkage beyond 2 h (Figure 4.8).

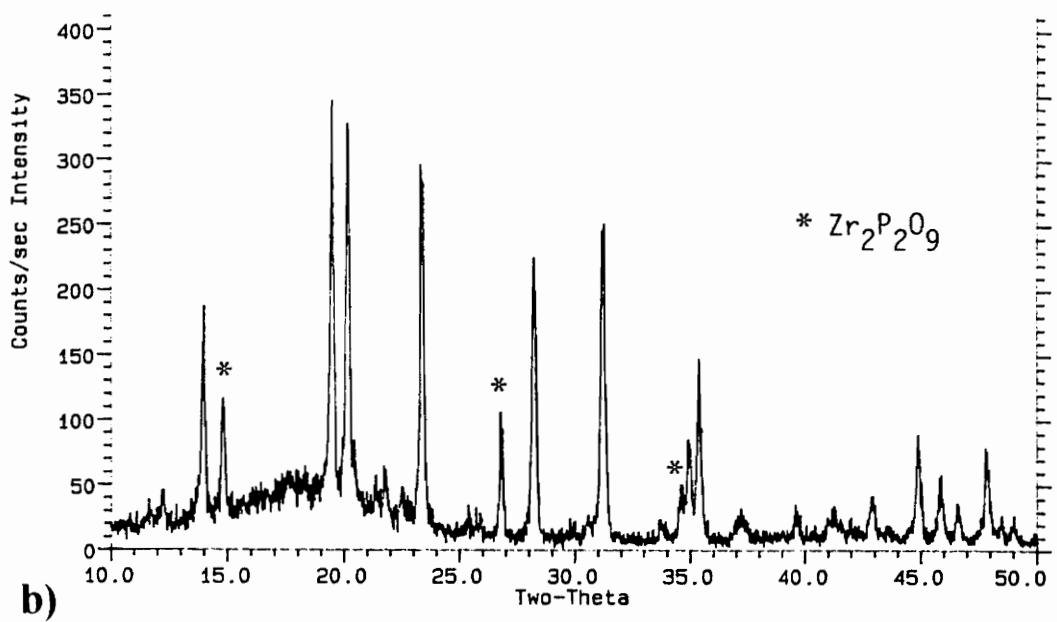
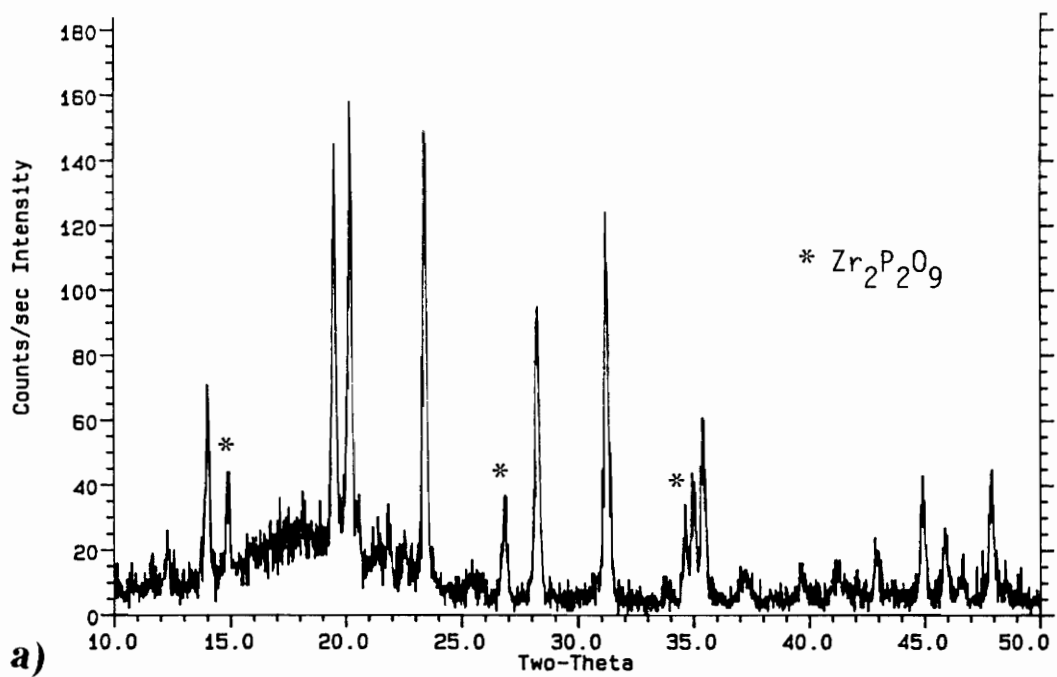


Figure 4.5 XRD patterns of CMZP with 2.7wt% ZnO fired to 1260°C for: a) 0.33h and b) 1h

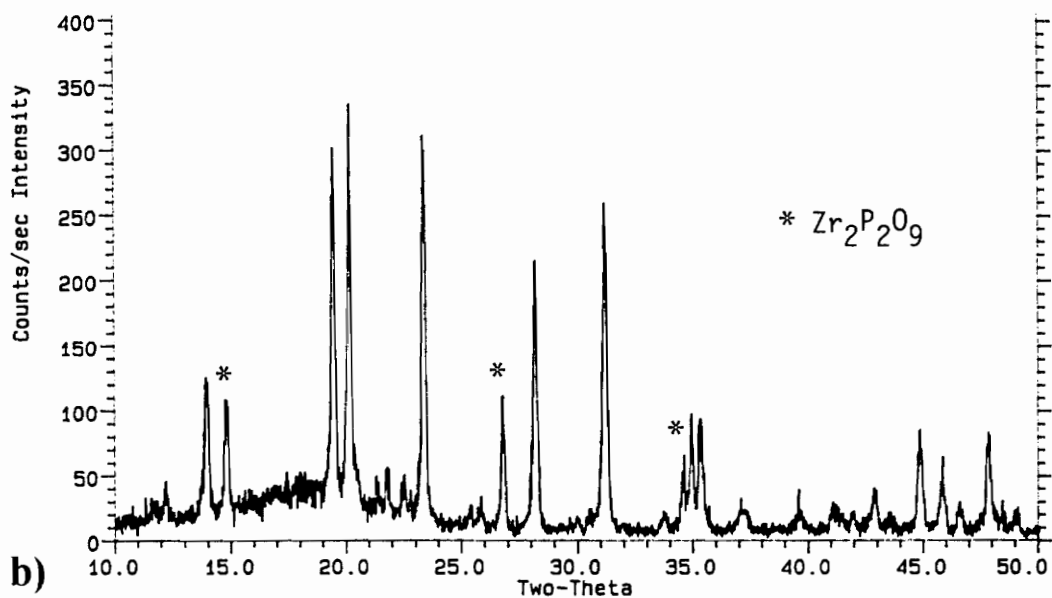
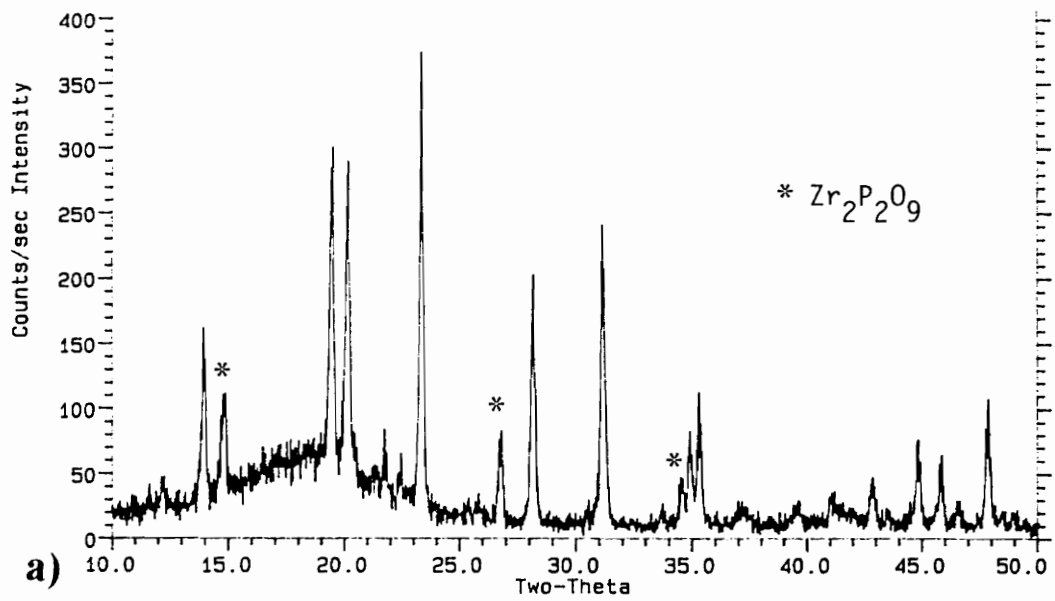


Figure 4.6 XRD patterns of CMZP with 2.7wt% ZnO fired to 1260°C for: a) 4h and b) 12h

Sintering of Dry Pressed CMZP

5 deg/min to 1350C

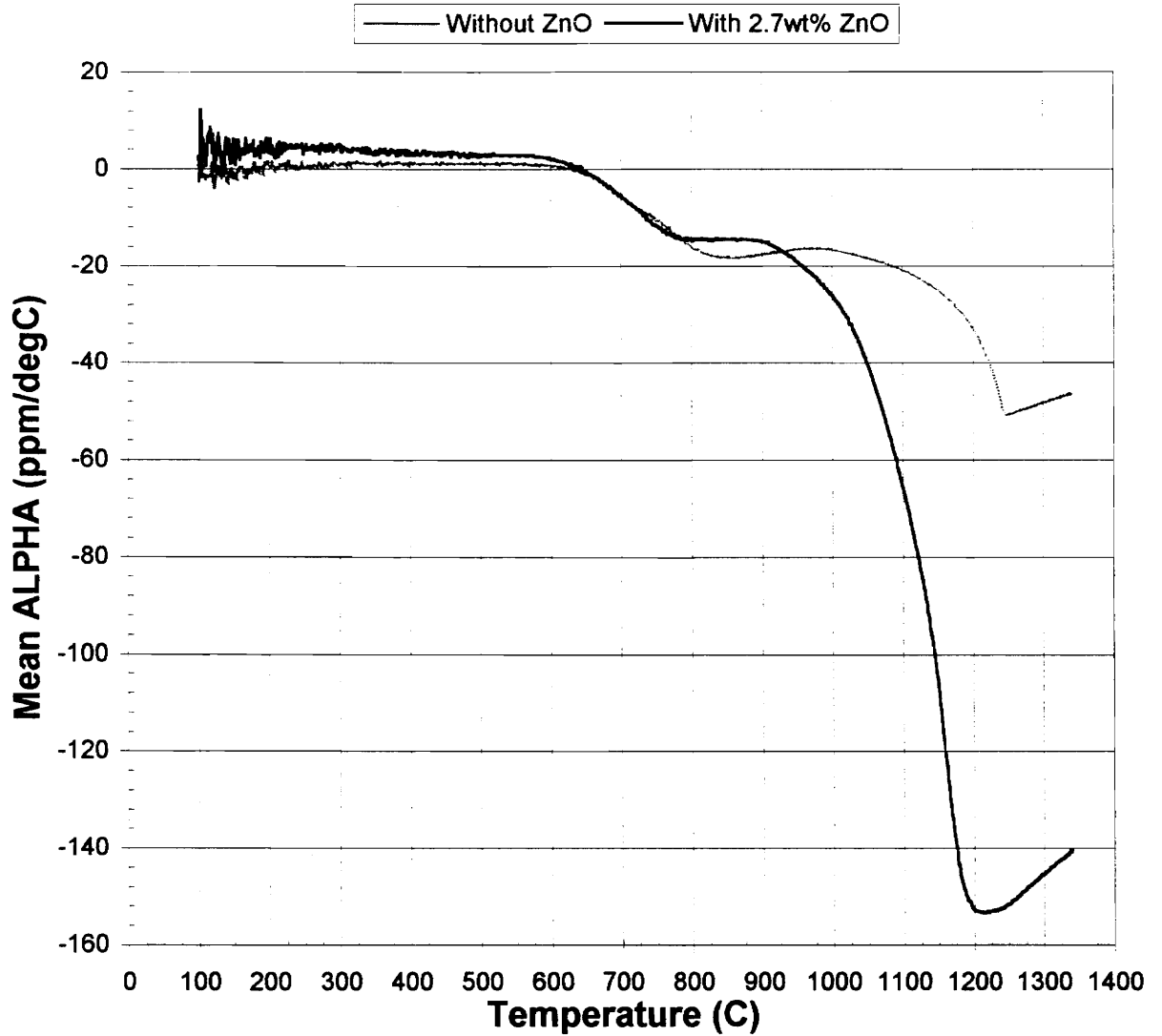


Figure 4.7 Dilatometric sintering profiles of dry pressed CMZP with and without 2.7wt% ZnO

Sintering of Dry Pressed CMZP with 2.7% ZnO

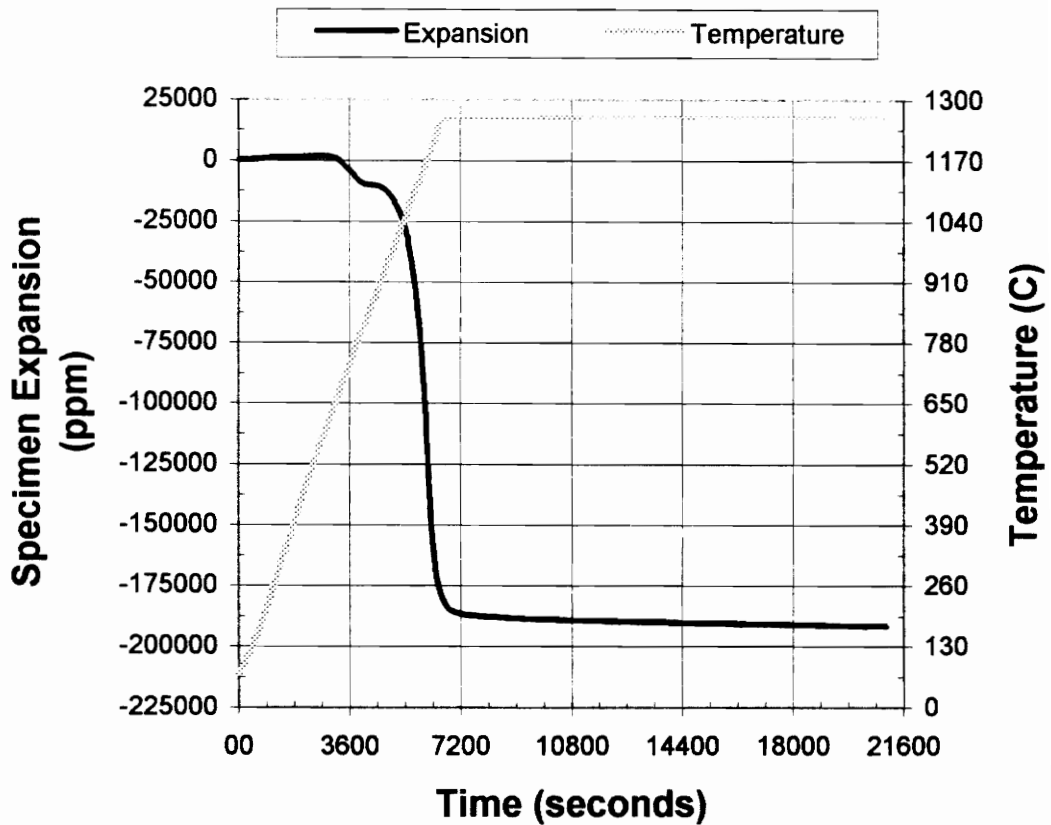


Figure 4.8 Dilatometric sintering profile of dry pressed CMZP with 2.7wt% ZnO fired to 1260°C for 4h

Sintering of slip cast specimens exhibited similar behavior. For samples with 2 wt% ZnO, specimen shrinkage was 26% with a minimum Mean ALPHA temperature located at 1175°C (Figure 4.9). When fired to this temperature, the majority of sintering took place within the first 0.5 h with little additional densification beyond 1 h (Figure 4.10).

Another characteristic of both dry pressed and slip cast samples during sintering was the formation of a densification “plateau” around 850°C. Comparing dry pressed samples with and without ZnO, the addition of ZnO sintering aid pushed back the temperature at which this plateau started as well as decreased the temperature range for which it appeared. The origin of this plateau is believed to be associated with the crystallization of CMZP.

The temperature at which the minimum Mean ALPHA develops correlates very well with the temperature at which secondary phases begin forming, as previously described in Section 4.1.1. Additionally, this temperature is close to the temperature where Agrawal and Stubican²² witnessed partial melting of $\text{Ca}_{0.5}\text{Zr}_2(\text{PO}_4)_3$ samples sintered with MgO (>1200°C) and ZnO (>1100°C), indicating that the zinc and magnesium phosphates melt and the glassy phase promotes sintering. This temperature at which liquid phase sintering begins is most likely the minimum Mean ALPHA temperature. A sintering temperature at this minimum is thought to be the optimal sintering temperature for CMZP at a given ZnO level.

4.2.2 Development of Microstructure with Temperature for Dry Pressed Samples

The SEM was utilized to view fracture surfaces of the 1” disks used in the XRD pattern versus sintering temperature experiment. Fracture surfaces were analyzed for samples fired for 0.33 h at 1040, 1105, 1170, 1235, and 1300°C with 2.7 wt% ZnO. At 1040°C (Figure 4.11a), there was little evidence of sintering, such as interparticle necking, and densification was minimal, about 3% shrinkage (change in diameter). Lack of sintering is further supported by comparison

Sintering of Slip Cast CMZP with 2% ZnO 5 deg/min to 1275C

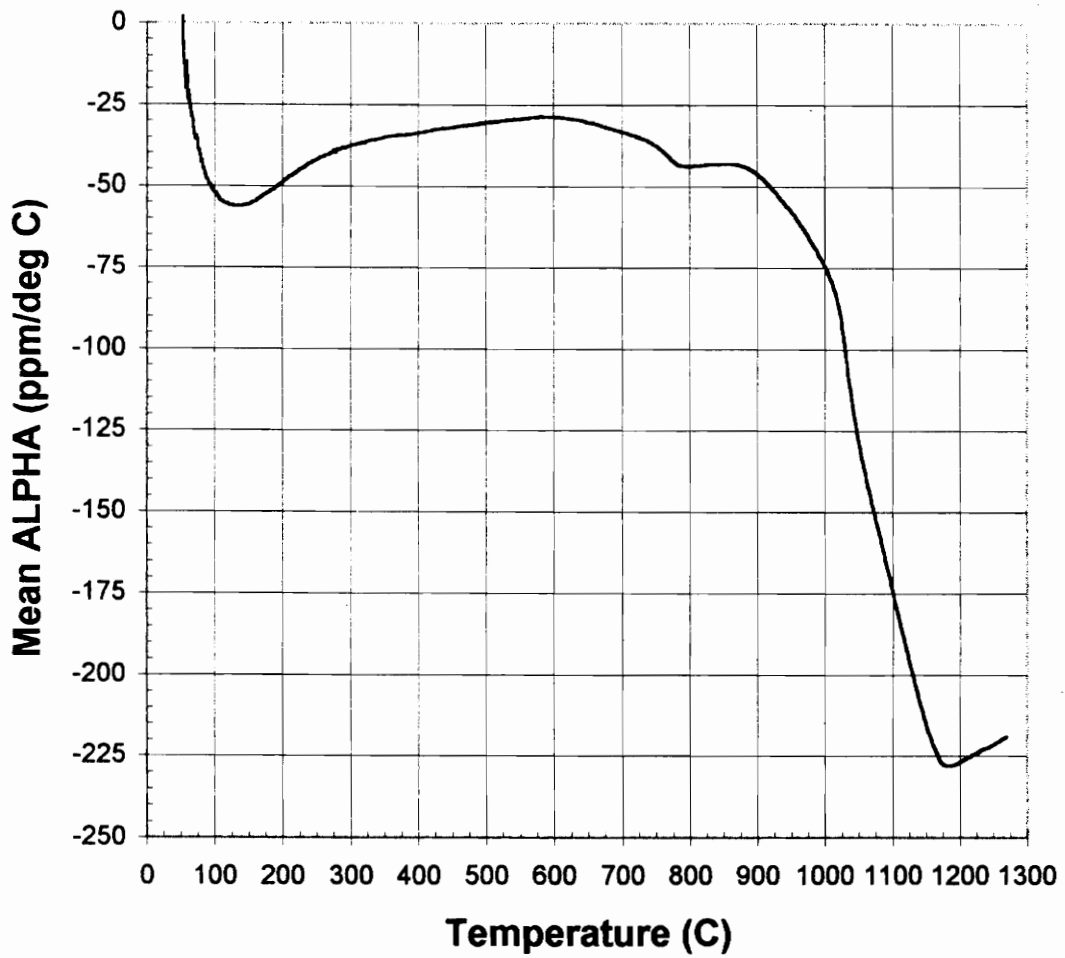


Figure 4.9 Dilatometric sintering profile of slip cast CMZP with 2wt% ZnO

Sintering of Slip Cast CMZP with 2% ZnO 5 deg/min to 1175C

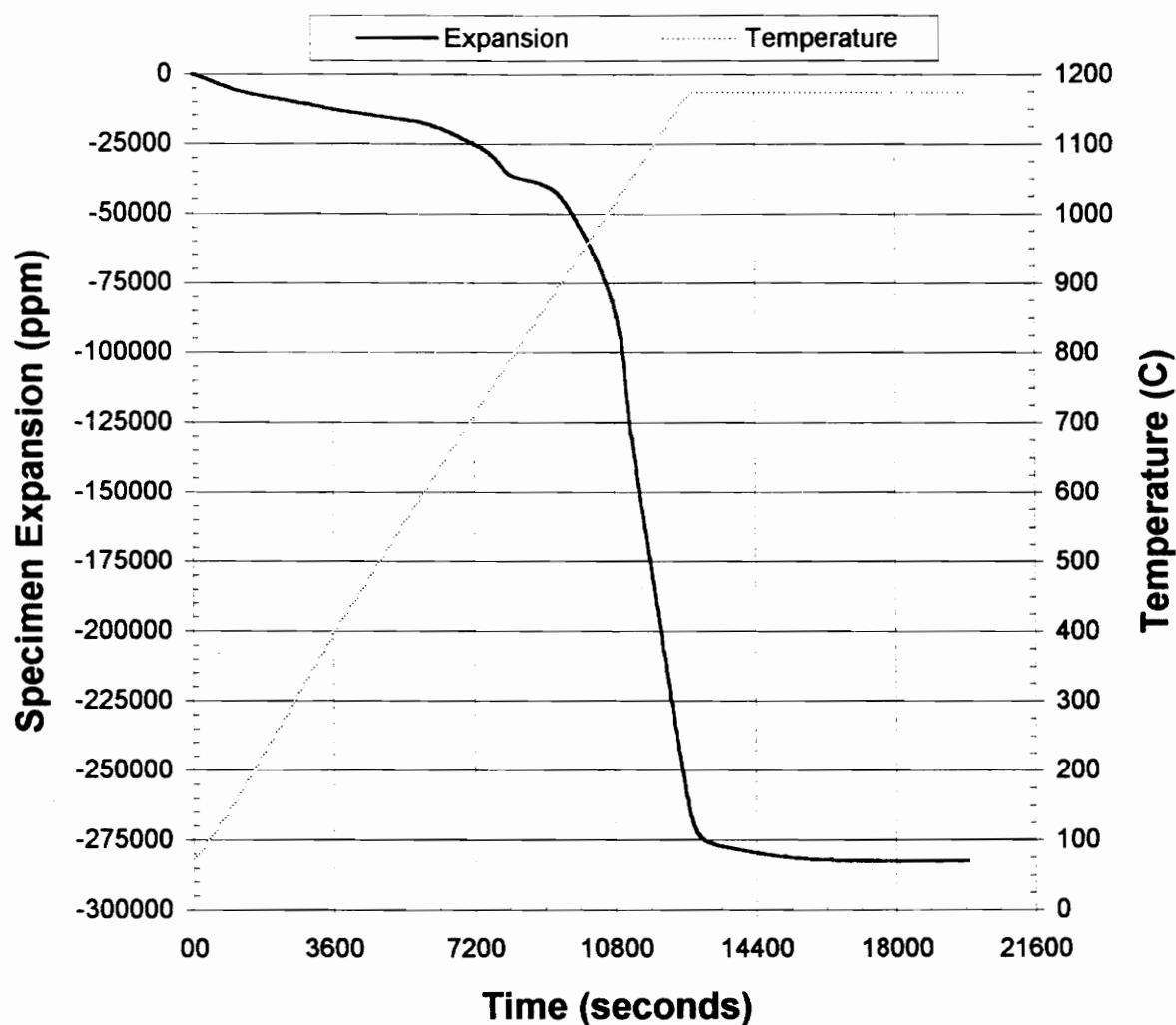


Figure 4.10 Dilatometric sintering profile of slip cast CMZP with 2wt% ZnO fired to 1175°C for 2h

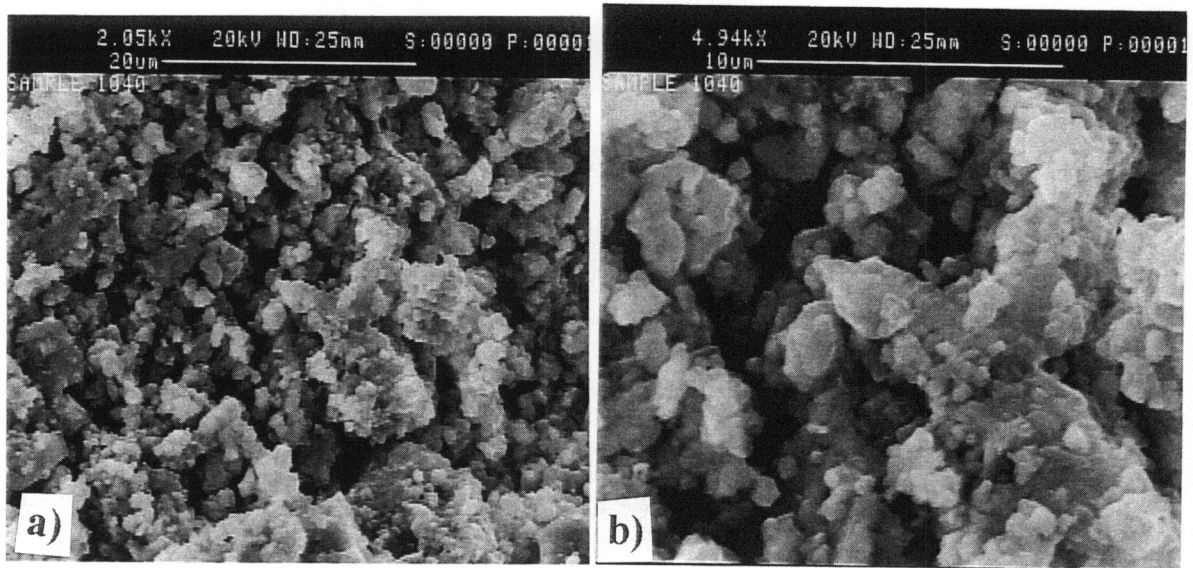


Figure 4.11a SEM fracture surface micrograph of CMZP with 2.7wt% ZnO fired to 1040°C for 0.33h at: a) 2kX and b) 5kX

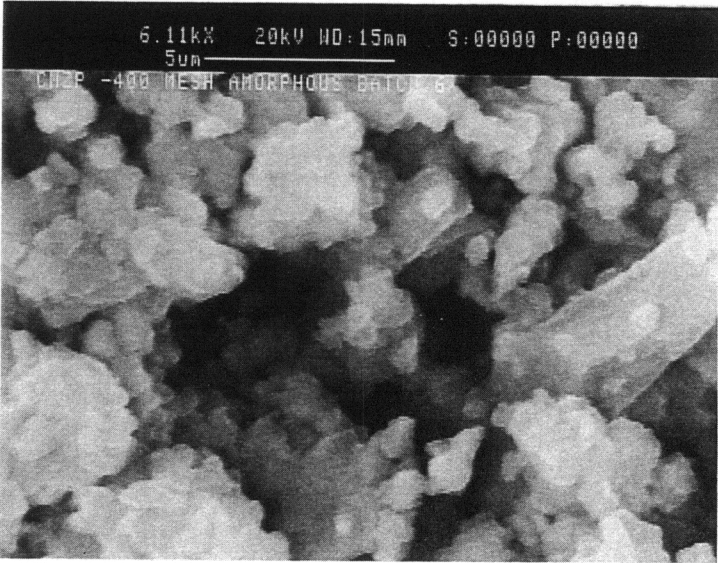


Figure 4.11b SEM micrograph of -400 mesh CMZP powder at 6kX

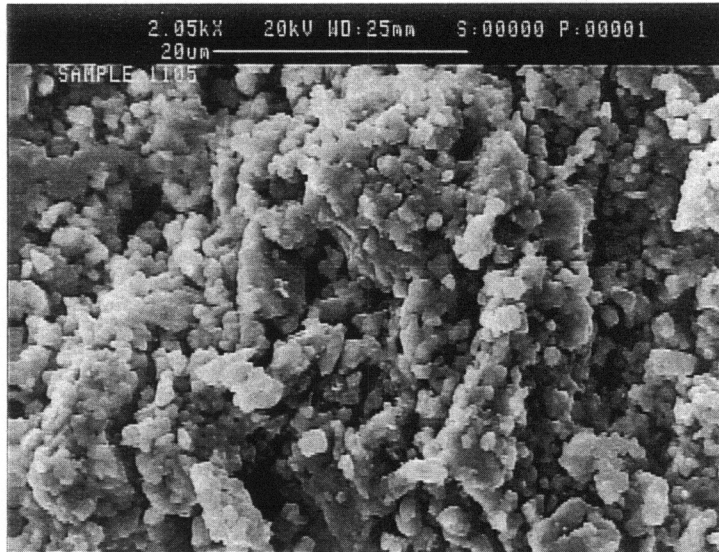


Figure 4.12a SEM fracture surface micrograph of CMZP with 2.7wt% ZnO fired to 1105°C for 0.33h

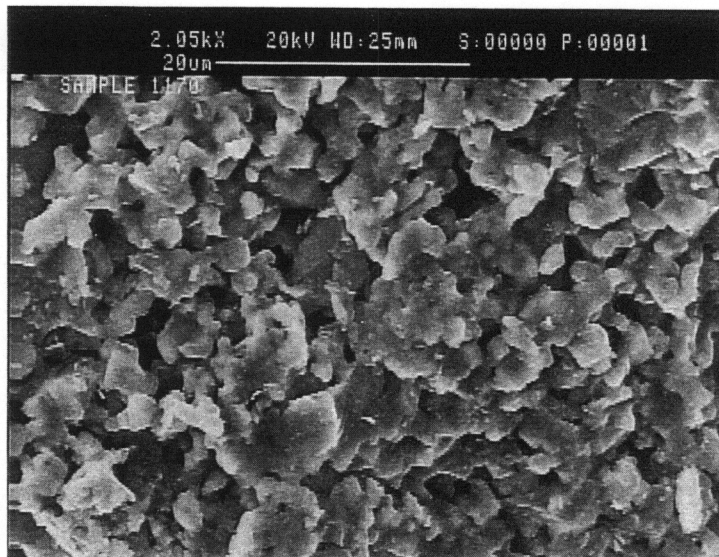


Figure 4.12b SEM fracture surface micrograph of CMZP with 2.7wt% ZnO fired to 1170°C for 0.33h

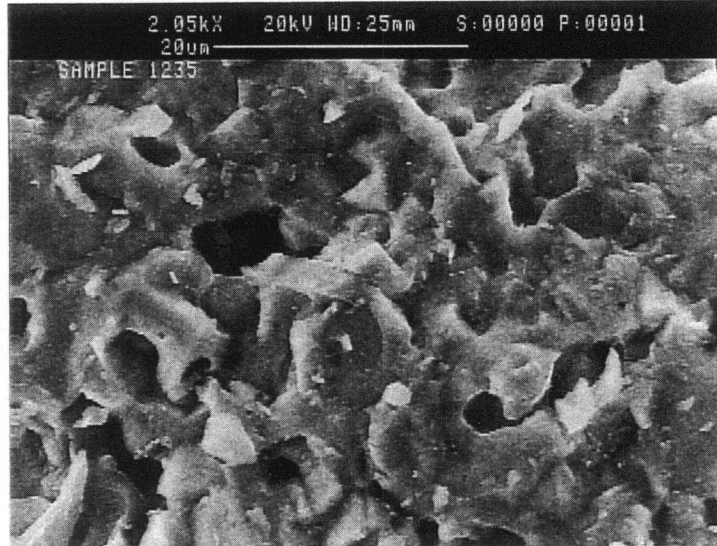


Figure 4.13a SEM fracture surface micrograph of CMZP with 2.7wt% ZnO fired to 1235°C for 0.33h

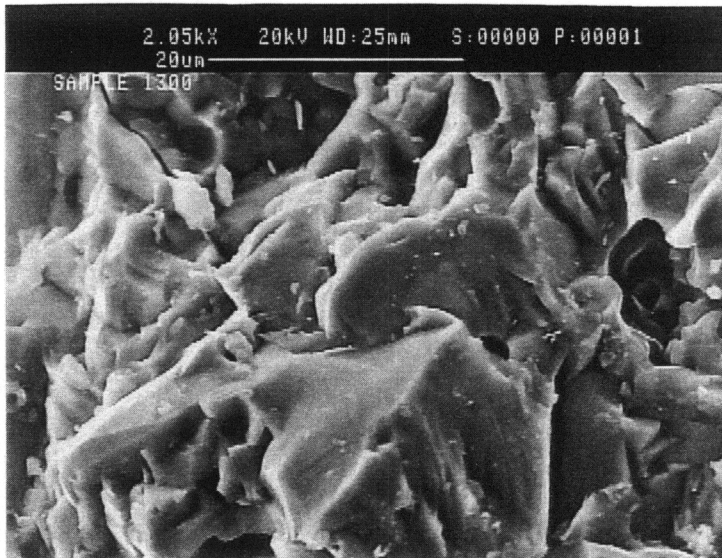


Figure 4.13b SEM fracture surface micrograph of CMZP with 2.7wt% ZnO fired to 1300°C for 0.33h

with the SEM micrograph of -400 mesh CMZP powder (Figure 4.11b). The two micrographs were nearly identical, both exhibiting a wide distribution of highly agglomerated particles. At 1105°C (Figure 4.12a), neck growth was more advanced and sample shrinkage was 6%. The development of interparticle porosity, a classic characteristic of solid-state sintering, was also observed. The small sample shrinkage, particle necking, and open pore structure suggest the sample is still in the initial or 1st stage of sintering²⁵. By 1170°C (Figure 4.12b), sample shrinkage was 16% and a large-grained structure had developed. These large grains are the product of the sintered agglomerates and subsequent grain growth. The increase in sample shrinkage, decrease in the mean pore size, and presence of a interconnected pore structure suggest the sample is in the intermediate stage of sintering. Furthermore, the relatively smooth fracture surface, typical of transgranular fracture⁸, indicates that solid-state sintering is the dominant sintering mechanism. At 1235°C (Figure 4.13a), a dramatic difference in the fracture surface takes place. Rapid grain growth occurred which resulted in intragranular porosity. The surface adopted a more jagged relief with some smooth areas remaining. Given that sample shrinkage only increased to about 17.5% and a non-interconnected pore structure had developed, the sample has entered in the final stage of sintering. The beginnings of a rough, faceted fracture surface suggest the initiation of intergranular fracture²⁶. As stated previously, this is also the temperature range at which impurity phases started to form, as shown in the XRD data. The combination of these two observations, a change in fracture surface and XRD data, strongly suggest the onset of liquid phase sintering. At 1300°C (Figure 4.13b), sample shrinkage only increased to 18%; however, grain growth was very pronounced and nearly all porosity was eliminated. These types of microstructural changes are typical of samples at the end of the final stage of sintering. Furthermore, the elimination of porosity, especially closed porosity, without a corresponding increase in sample shrinkage, is

indicative of liquid phase sintering. The fracture surfaces were very rough and faceted signaling the complete dominance of intergranular fracture. It can therefore be assumed that at some temperature above 1170°C, the dominant sintering mechanism changed from diffusional to liquid phase. This assumption is supported by the rapid grain growth, the elimination of porosity, and the shift in fracture mode from transgranular to intergranular at temperatures above 1170°C. Finally, these data correlate very well with the previously described XRD (Section 4.1.1) and dilatometric (Section 4.2.1) analyses which also strongly suggest the onset of liquid phase sintering at some temperature near the melting point of a zinc phosphate phase. Therefore, the use of ZnO as a sintering aid appears to limit the temperature to which CMZP can be used without compositional degradation, as will be discussed in Section 5.4.

4.3 Effects of Processing on Bulk Density

4.3.1 Dry Pressed Samples

Effects of processing, which included sintering time, temperature, and level of ZnO sintering aid on bulk density of dry pressed samples were determined using a simple two-level factorial design as described in Section 3.1. The following bulk densities were obtained.

Table 4.3 Bulk Densities of Dry Pressed Samples

Sample	Time	Temperature	%ZnO	Bulk Density
(1)	0.5 h	1250°C	1.0%	2.46 g/cc
(A)	4 h	1250°C	1.0%	2.91 g/cc
(B)	0.5 h	1300°C	1.0%	2.79 g/cc
(AB)	4 h	1300°C	1.0%	2.84 g/cc
(C)	0.5 h	1250°C	3.0%	3.02 g/cc
(AC)	4 h	1250°C	3.0%	3.08 g/cc
(BC)	0.5 h	1300°C	3.0%	3.09 g/cc
(ABC)	4 h	1300°C	3.0%	3.07 g/cc
(0.5B)	0.5 h	1300°C	0.5%	2.51 g/cc
(-400)	8 h	1300°C	0%	2.31 g/cc

RS1 statistical analysis proved that ZnO was the most dominant of the three main factors for controlling bulk density, accounting for about 69% of the variability. Further RS1 optimization calculations suggested a bulk density value of 3.17 g/cc could be obtained if sintered for 4 h at 1227°C with 2.22% ZnO. Given that the theoretical bulk density of CMZP is 3.18 g/cc, this optimized calculation is greater than 99% of theoretical. RS1 generated surface plots (Figure 4.14) illustrate the bulk density trends for CMZP sintered with ZnO. When correlated to MOR and CTE data, as will be discussed in Section 5.3, bulk density was determined not to be a good indicator of high strength and optimization of bulk density was actually counterproductive for obtaining desired MOR values of greater than 90 MPa.

4.3.2 Slip Cast Samples

Although an experimental design was not employed, slip cast samples followed the same trend as the dry pressed samples. The following bulk densities were obtained.

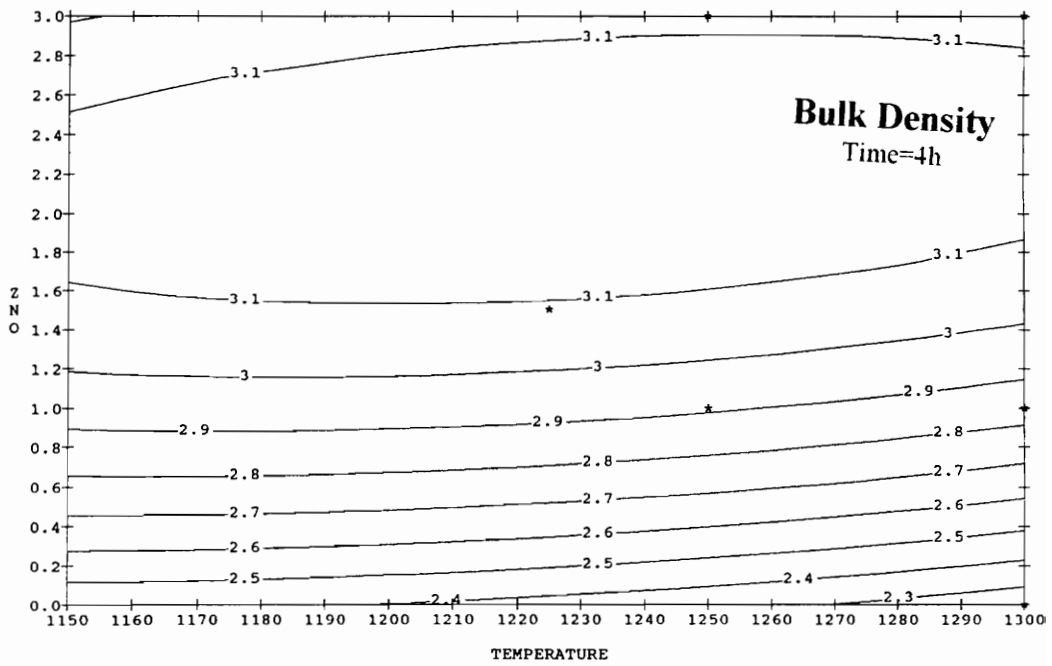
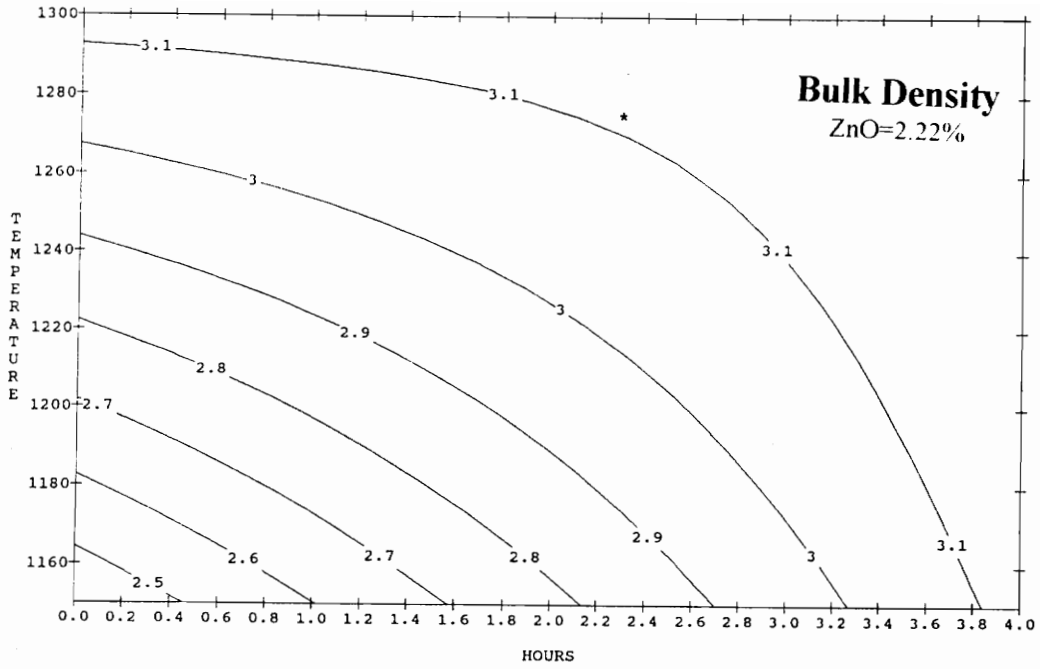


Figure 4.14 RSI generated bulk density contour plots for dry pressed samples

Table 4.4 Bulk Densities of Slip Cast Samples

Sample ID	Time	Temperature	%ZnO	Bulk Density
(12-1)	0.5 h	1200°C	2.0%	3.22 g/cc
(12-4)	0.7 h	1175°C	2.0%	3.06 g/cc
(12-14)	0.5 h	1200°C	1.5%	2.89 g/cc

The finer initial particle size ($< 1 \mu\text{m}$), and therefore greater reactivity, of the slip cast material, as compared to the dry pressed samples, allowed for higher bulk densities to be obtained. However, the higher bulk density samples also contained the impurity phases as described in Section 4.1. Therefore, the onset of liquid phase sintering is responsible for significant increases in bulk density. In addition, the density of ZnO (5.606 g/cc) pushed the bulk density of CMZP above its theoretical value of 3.184 g/cc⁶, as witnessed with sample (12-1). However, these increases are accompanied by grain growth and subsequent microcracking, both of which are detrimental to mechanical properties.

4.4 Effects of Processing on Microstructure

4.4.1 Dry Pressed Samples

Optical analysis at 240X of the polished and thermally etched dry pressed samples revealed the effects of time, temperature, and %ZnO on microstructure. For samples with 1wt% ZnO, time and/or temperature increases cause the formation of a coarse microstructure consisting of large grains, microcracks, liquid phase grain boundaries, and intragranular porosity. When viewed optically at 240X, sample (1), which was processed at 1250°C for 0.5 h, exhibited a fine grained structure with no evidence of excessive and/or exaggerated grain growth, liquid phase formation, or microcracking (Figure 4.15a). However, when viewed on the SEM at 2.5kX (Figure

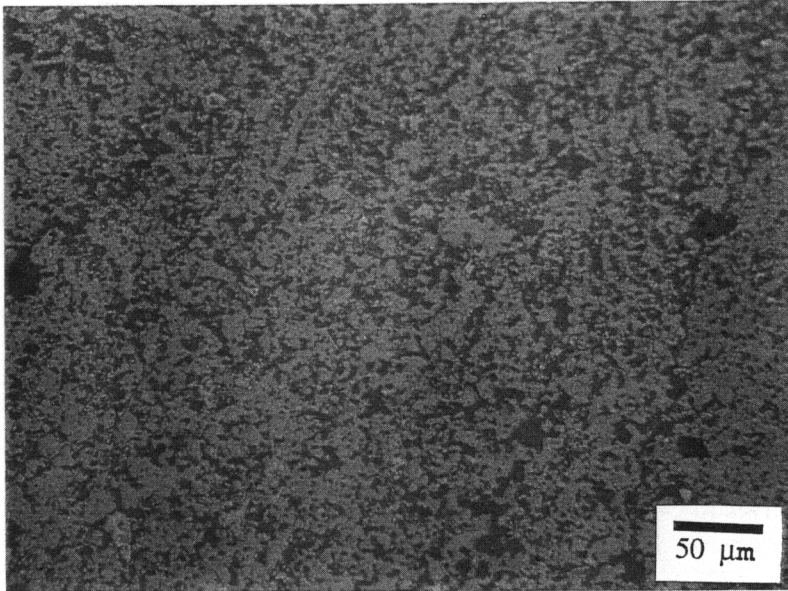


Figure 4.15a Micrograph of dry pressed sample (1) at 240X

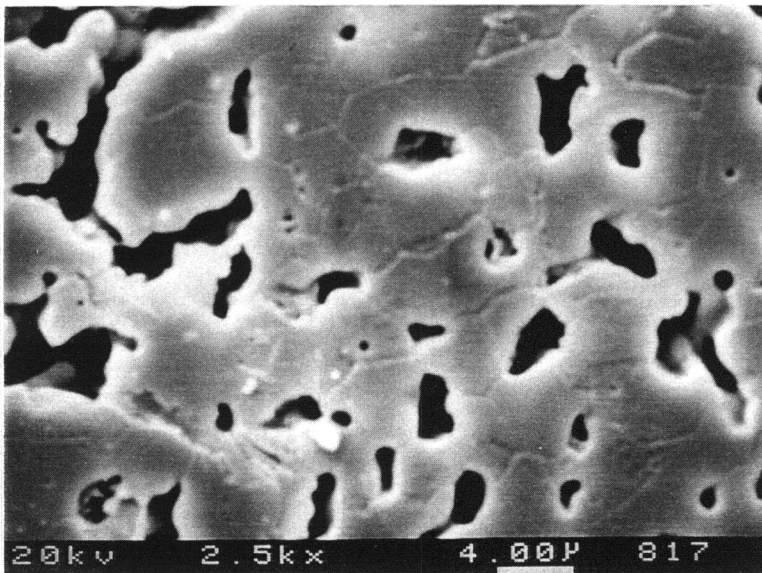


Figure 4.15b Micrograph of dry pressed sample (1) at 2.5kX

4.15b), a very fine grain boundary structure was observed. As stated previously, sample (1) also had a low bulk density as compared to the other samples. The low bulk density and the resulting microstructure of this sample indicate the lack of liquid phase sintering.

Increasing firing time to 4 h [sample (A)] (Figure 4.16a), firing temperature to 1300°C [sample (B)] (Figure 4.16b), or their interaction [sample (AB)] (Figure 4.17) resulted in a degradation in microstructure, as previously stated. Samples fired to 1300°C for 8 h without ZnO [sample (-400)] (Figure 4.18) or to 1300°C for 0.5 h with 0.5% ZnO [sample (0.5B)] (Figure 4.19) developed similar fine grained structures as sample (1), as seen by comparison of SEM micrographs at 2.5kX. However, unlike samples (1) and (0.5B), the fine grain boundary structure was not evidenced in sample (-400). The connected pore structure, small grain size, and lack of secondary phase grain boundaries define the absence of liquid phase sintering. The fact that very similar microstructures developed for samples (1), (0.5B), and (-400) supports the theory that ZnO increases the rate of solid-state (diffusional) sintering up to the minimum Mean ALPHA temperature, at which a liquid phase is introduced.

At 3wt% ZnO, all four samples [(C), (AC), (BC), and (ABC)] (Figure 4.20 and 4.21) developed almost identical microstructures of large grains with coarse, liquid phase grain boundaries, intragranular porosity, and microcracking. As previously described in Section 4.1.1, these grain boundaries were Mg⁺² and Zn⁺² rich and assumed to be Zn₂Mg(PO₄)₂. The presence of irregular shaped grains, especially elongated grains, is indicative of exaggerated grain growth which can be promoted by liquid phase sintering²⁷. These higher ZnO samples also displayed the formation of additional phase(s) within the large grains, seen as shiny white specks of irregular shape when viewed with an optical light microscope.

4.4.2 Slip Cast Samples

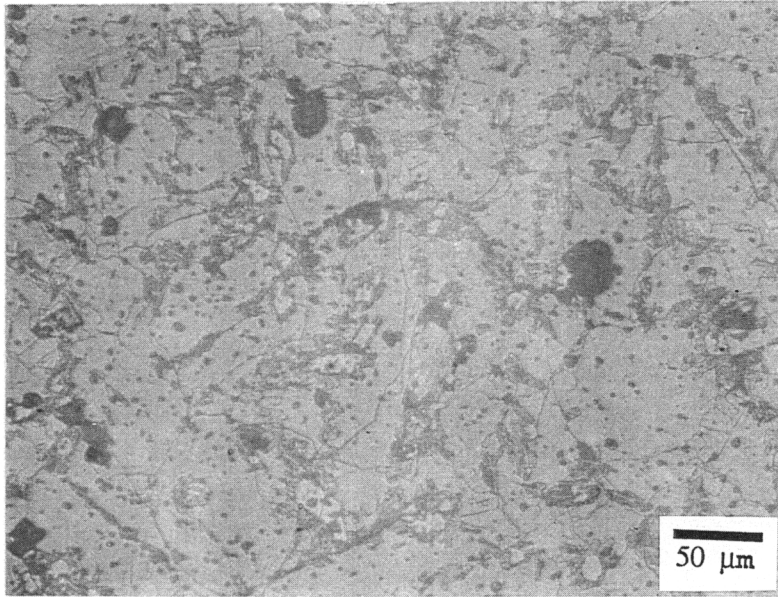


Figure 4.16a Micrograph of dry pressed sample (A) at 240X

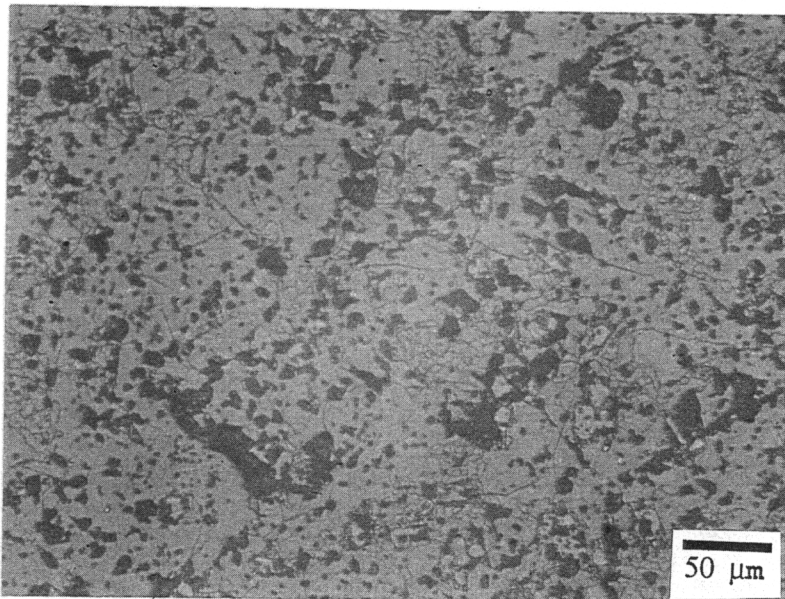


Figure 4.16b Micrograph of dry pressed sample (B) at 240X

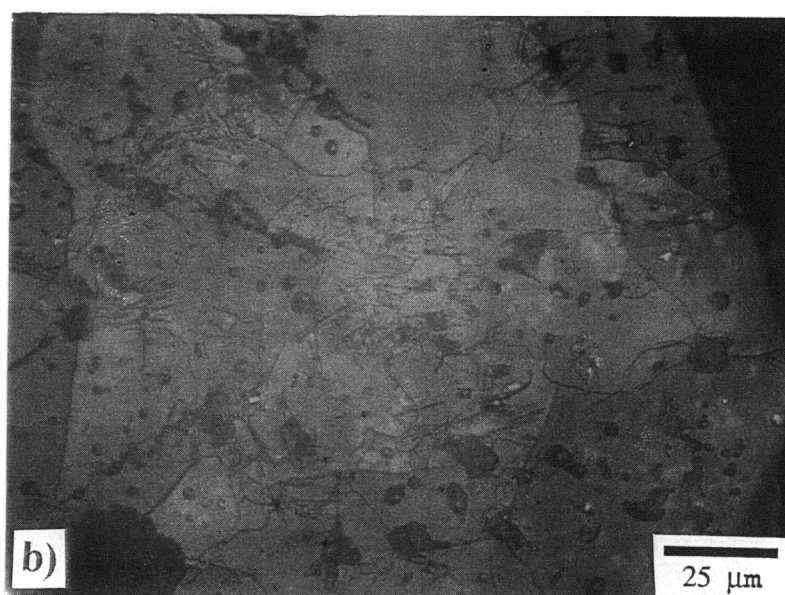
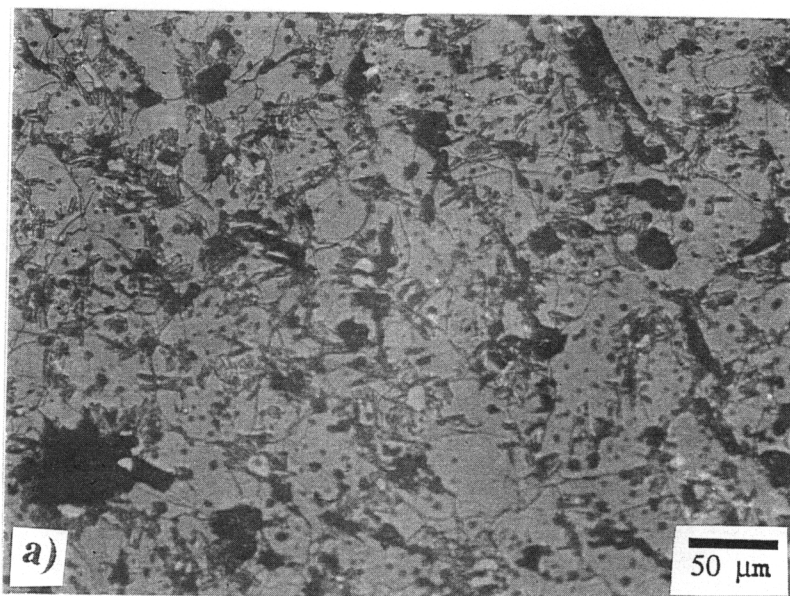


Figure 4.17 Micrographs of dry pressed sample (AB) at: a) 240X and b) 600X

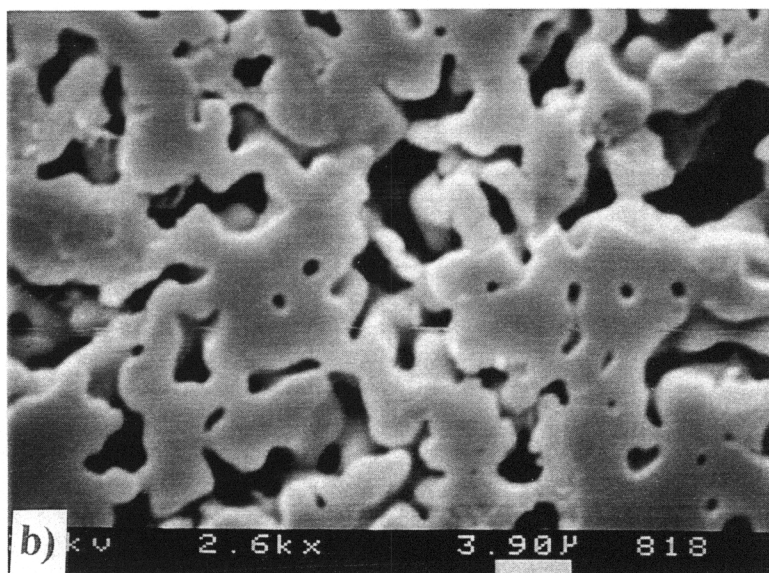
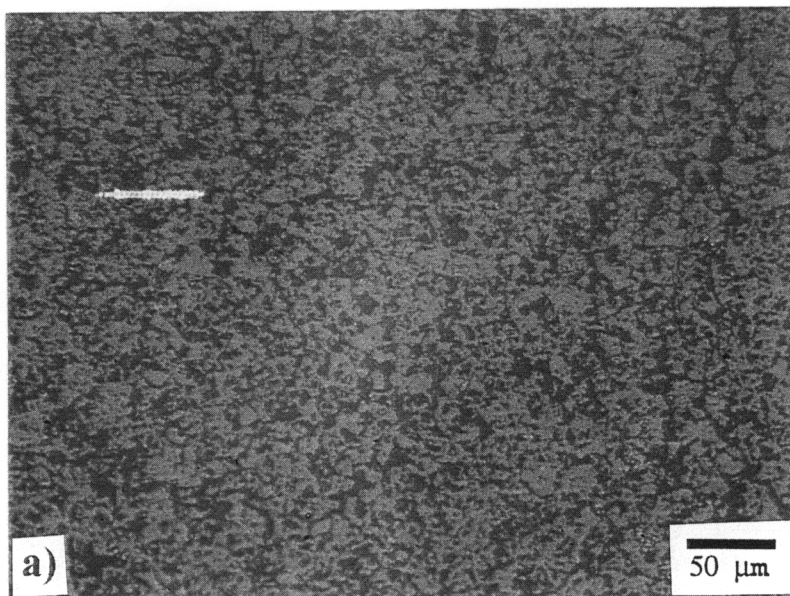


Figure 4.18 Micrographs of dry pressed sample (-400) at: a) 240X and b) 2.5kX

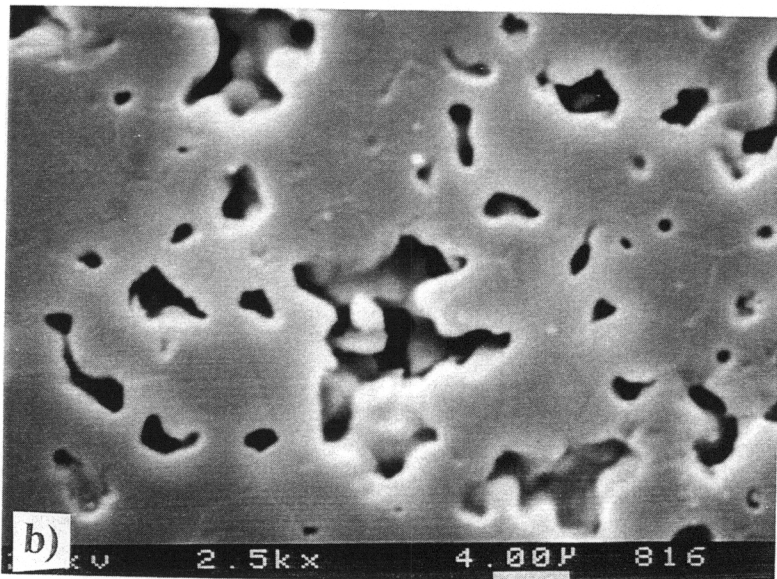
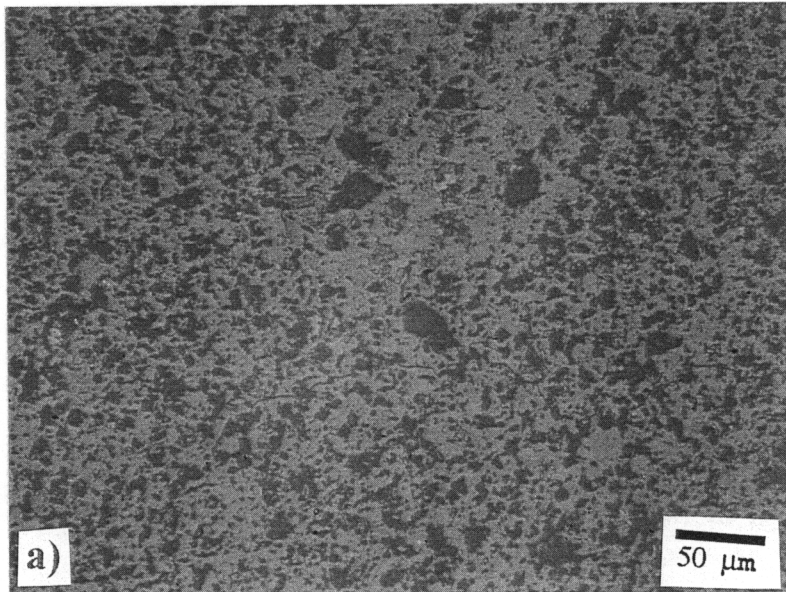


Figure 4.19 Micrographs of dry pressed sample (0.5B) at: a)240X and b) 2.4kX

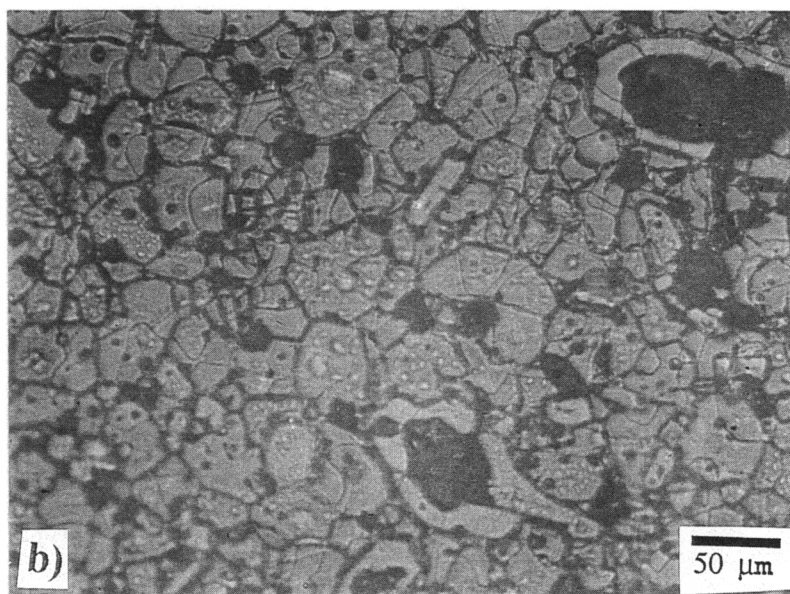
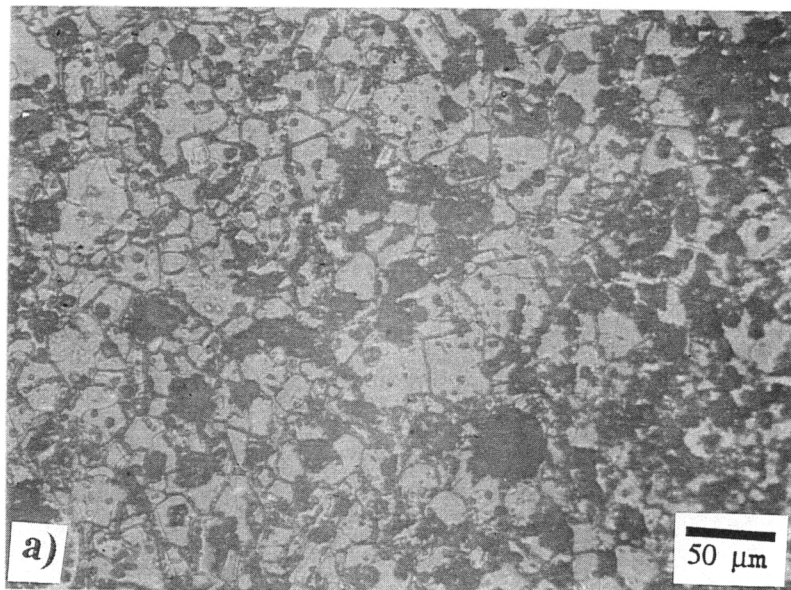


Figure 4.20 Micrographs at 240X of dry pressed samples: a) sample (C) and b) sample (AC)

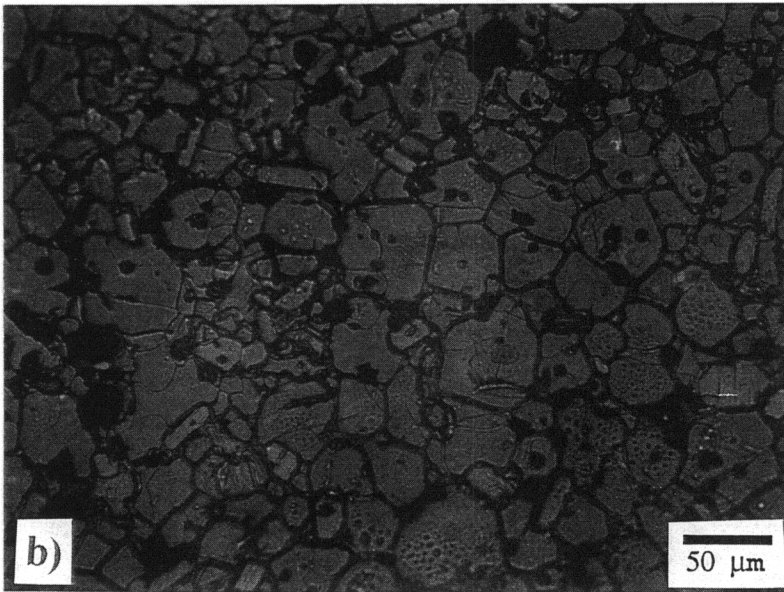
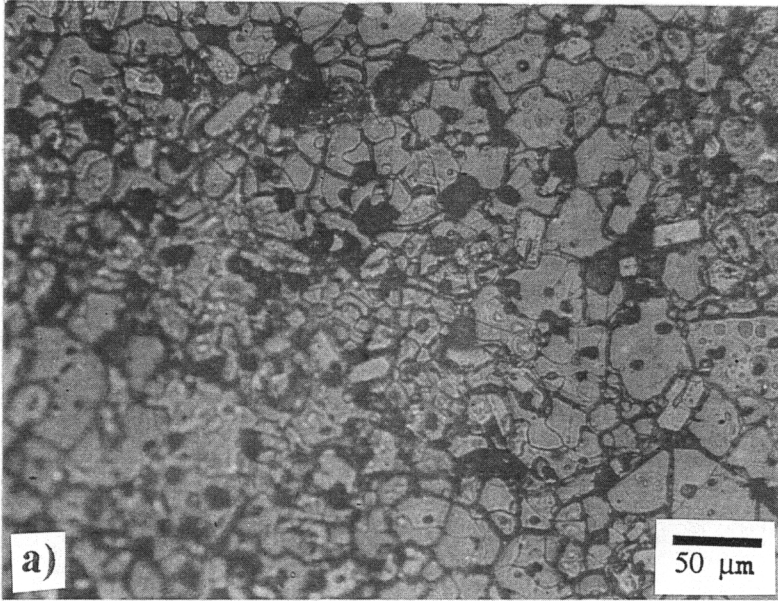


Figure 4.21 Micrographs at 240X of dry pressed samples: a) sample (BC) and b) sample (ABC)

SEM and optical analysis of polished and thermally etched slip cast samples revealed similar changes in microstructure with time and temperature as with dry pressed samples. For samples processed with 1.0wt% ZnO, the result of temperature increases (1250 to 1300°C) and/or time increases (0.5 to 4 h) are easily seen (Figures 4.22-4.25). The 4 h firing time resulted in excessive grain growth and microcracking at both temperatures. Although grain growth was pronounced at 1300°C for 0.5 h, some small grained areas were still present. All but the 1250°C/0.5 h condition exhibited considerable microcracking, liquid phase grain boundaries, and intragranular porosity. At the 1250°C/0.5 h condition, the microstructure consisted of large rectangular grains “in a matrix of” small grained material. EDS analysis revealed these rectangular grains were zirconium phosphate, most likely the β -Zr₂P₂O₉ phase, as identified by XRD analysis. The large rectangular grains that formed in the dry pressed material, as described in the previous section, are probably of the same composition. The small initial grain size of the slip casting process was clearly evident at the 1250°C/0.5 h condition, especially when viewed at 600X. Temperature and/or time increases eliminated this small grained structure. Due to the small specimen sizes used, no additional physical property data were obtained for these samples.

The three main slip cast samples, [(12-1), (12-4), and (12-14)], exhibited similar results. When their microstructures were viewed optically at 240X, the effects of firing temperature and ZnO level were observed. At 1200°C for 0.5 h with 2.0wt% ZnO [sample (12-1)], a mostly large grained structure with microcracks, liquid phase grain boundaries, and zirconium phosphate (β -Zr₂P₂O₉) inclusions developed (Figure 4.26a). However, some small grained areas still existed, as seen in the SEM micrograph viewed at 4.9kX (Figure 4.26b), which also provided more detail in regards to microcracking and the presence of a liquid phase. It is interesting to note that the β -Zr₂P₂O₉ phase was not as distinct when viewed using the SEM and was surrounded by an

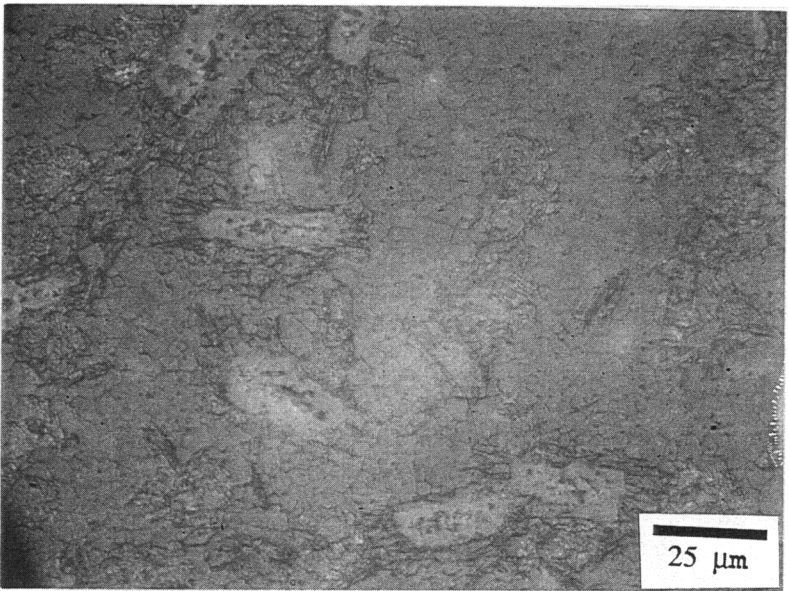
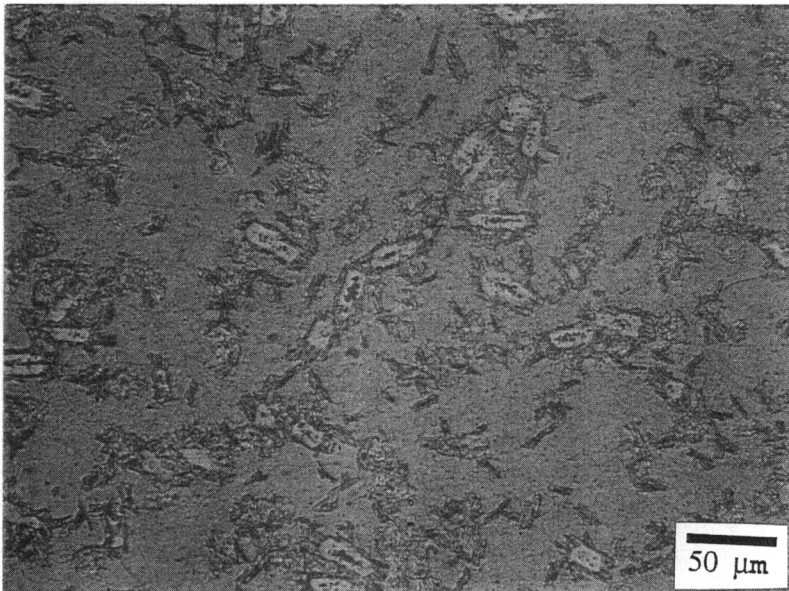


Figure 4.22 Micrographs of slip cast sample with 1wt% ZnO fired to 1250°C for 0.5h

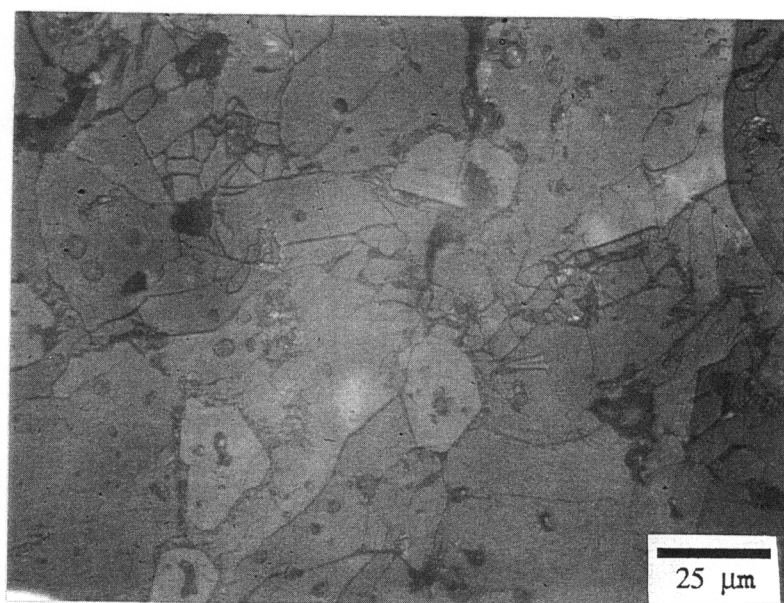
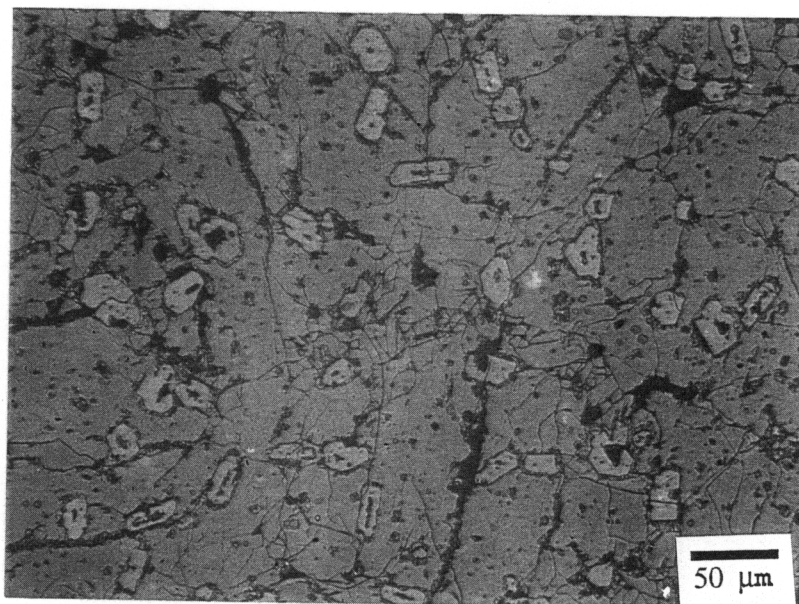


Figure 4.23 Micrographs of slip cast sample with 1wt% ZnO fired to 1250°C for 4h

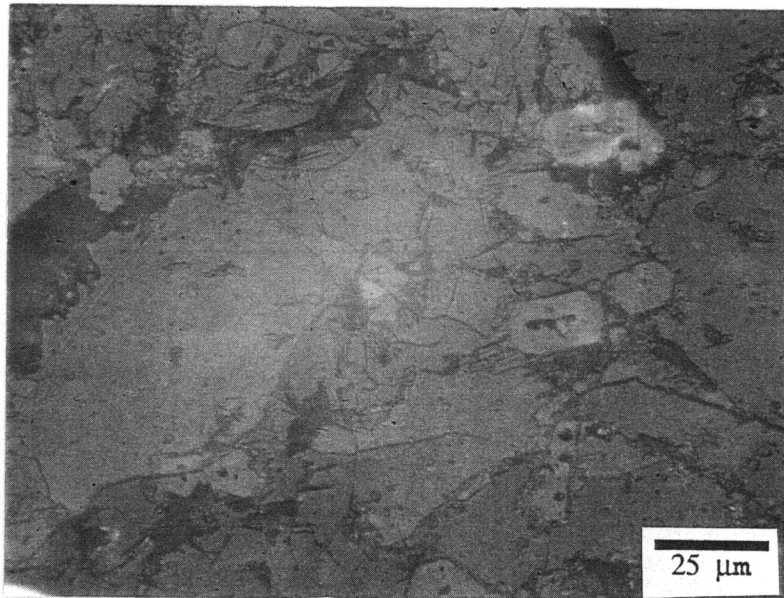
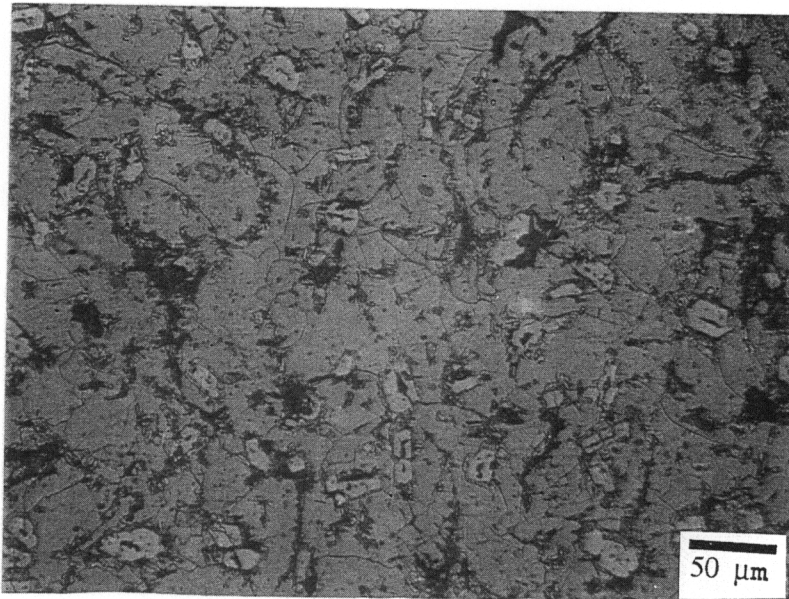


Figure 4.24 Micrographs of slip cast sample with 1wt% ZnO fired to 1300°C for 0.5h

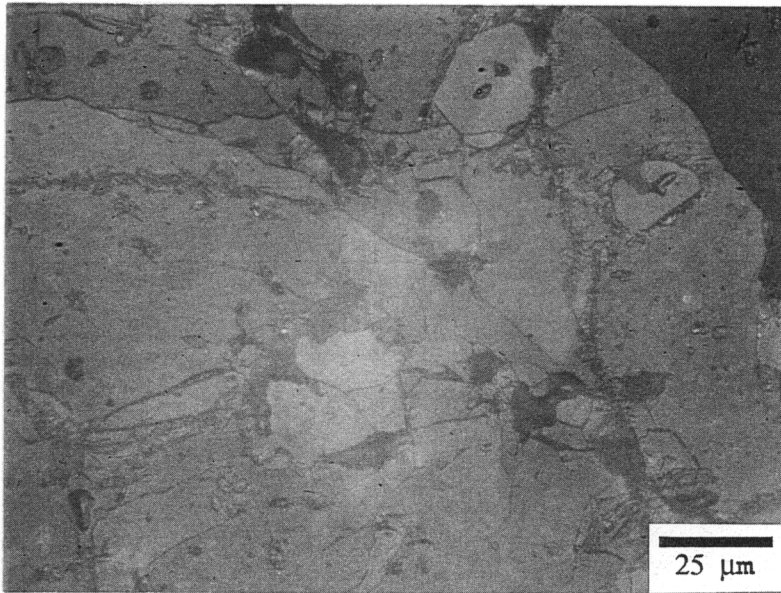
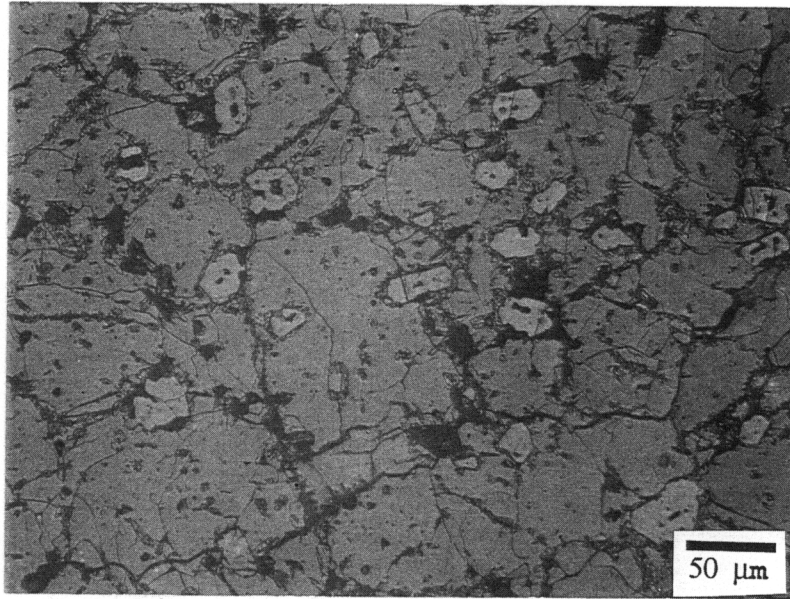


Figure 4.25 Micrographs of slip cast sample with 1wt% ZnO fired to 1300°C for 4h

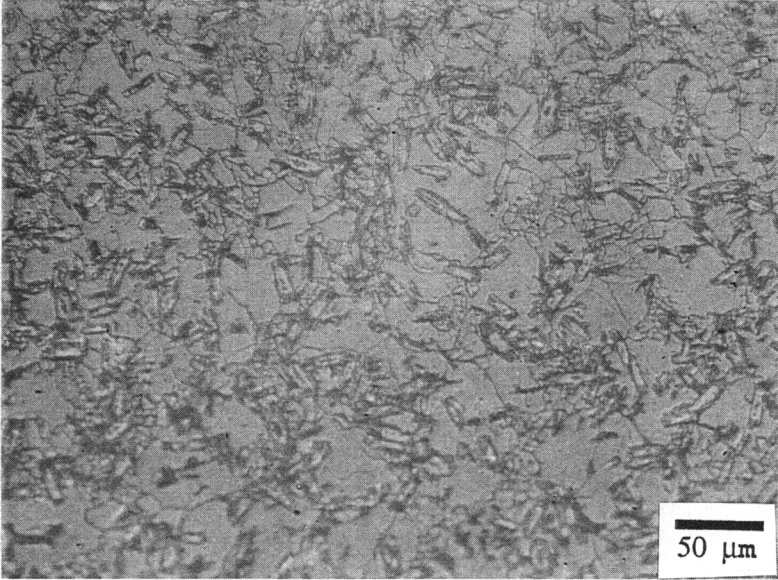


Figure 4.26a Micrograph of slip cast sample (12-1) at 240X

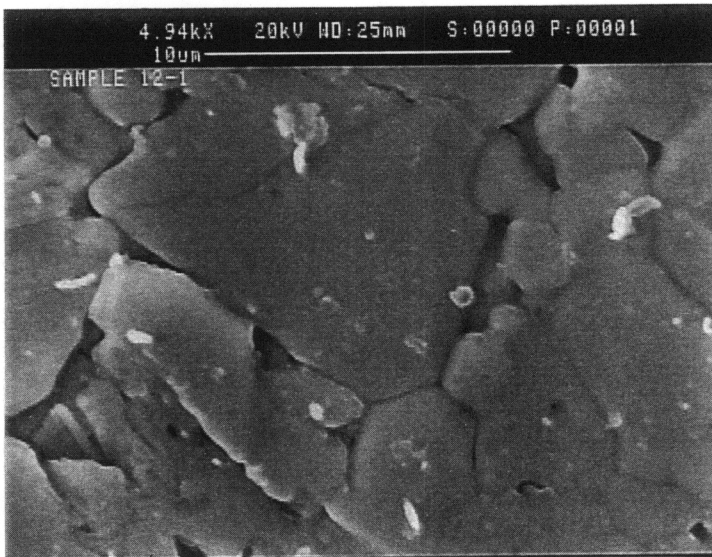


Figure 4.26b Micrograph of slip cast sample (12-1) at 4.9kX

intermediate region of finger-like projections. As stated in an earlier section, sample (12-1) was the most dense (3.22 g/cc) slip cast sample.

Reducing the firing temperature to 1175°C [sample (12-4)] resulted in a drastically different microstructure void of microcracks and discernible grain boundaries; however, zirconium phosphate inclusions were still present, as seen in the optical micrographs viewed at 240X (Figure 4.27a). When viewed under the SEM at 4.6kX (Figure 4.27b), a very fine grain boundary structure was evident, similar to dry pressed samples (1) and (0.5B), as well as non-interconnected closed porosity. Microcracked areas surrounding the zirconium phosphate inclusions could also be seen at this magnification. Given that this sample was fired at the temperature of the minimum Mean ALPHA temperature for the given ZnO level, a fine grain boundary structure is expected since this temperature is thought to be the onset of liquid phase sintering. However, the residual closed porosity suggests that liquid phase sintering was not totally dominant at this temperature. The lower bulk density (3.06 g/cc) further supports the theory that liquid phase sintering was not the dominant sintering mechanism at this temperature. It is therefore hypothesized that at the minimum Mean ALPHA temperature, sintering is controlled mainly by diffusion with a very limited contribution from a liquid phase.

Lowering the zinc oxide level to 1.5wt% [sample (12-14)] while maintaining the 1200°C firing temperature resulted in a microstructure void of zirconium phosphate inclusions, grain boundaries, and microcracks (Figure 4.28). Non-interconnected closed porosity was also more extensive, which resulted in a low bulk density (2.89 g/cc), the lowest of the three characterized slip cast samples. These microstructural features denote the total absence of liquid phase sintering. Although no dilatometric sintering tests were run, it can be assumed that the firing temperature for this sample was below the minimum Mean ALPHA temperature for the given ZnO level of

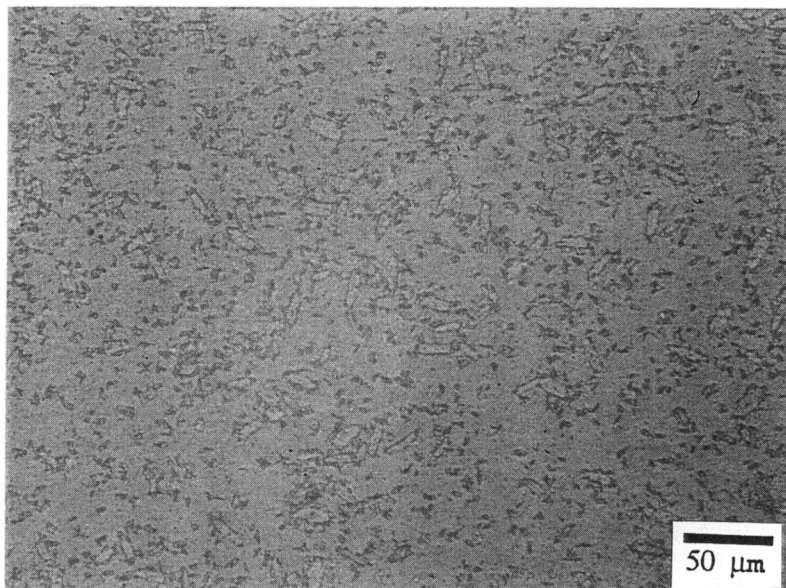


Figure 4.27a Micrograph of slip cast sample (12-4) at 240X

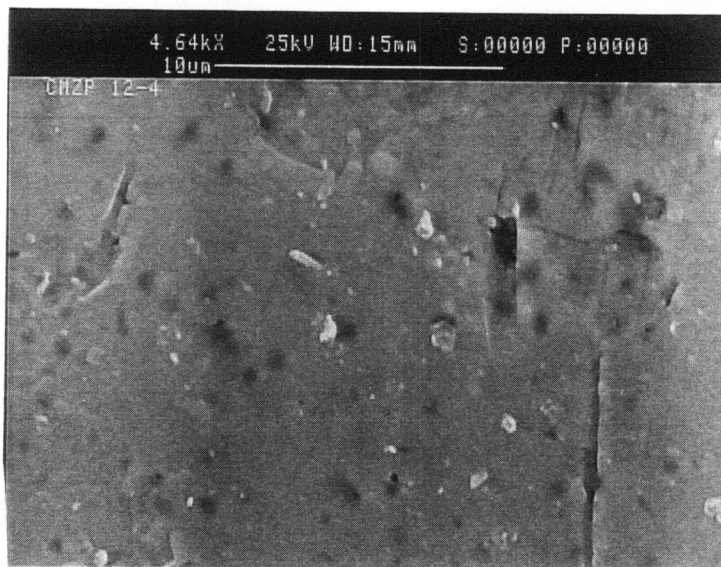


Figure 4.27b Micrograph of slip cast sample (12-4) at 4.6kX

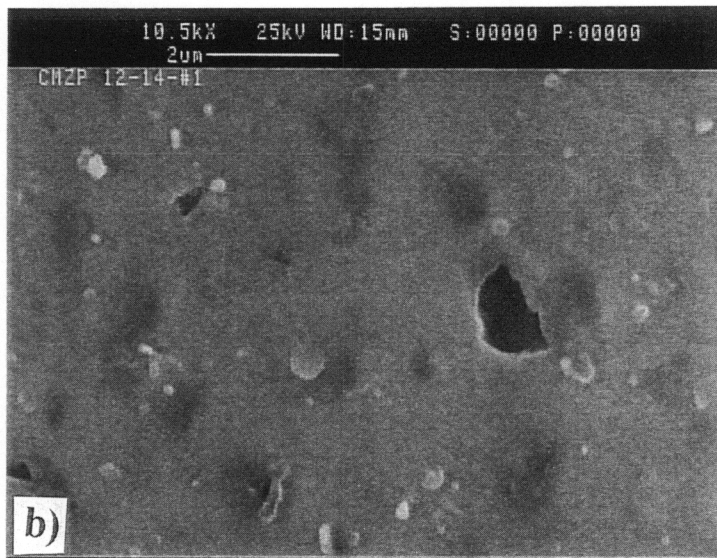
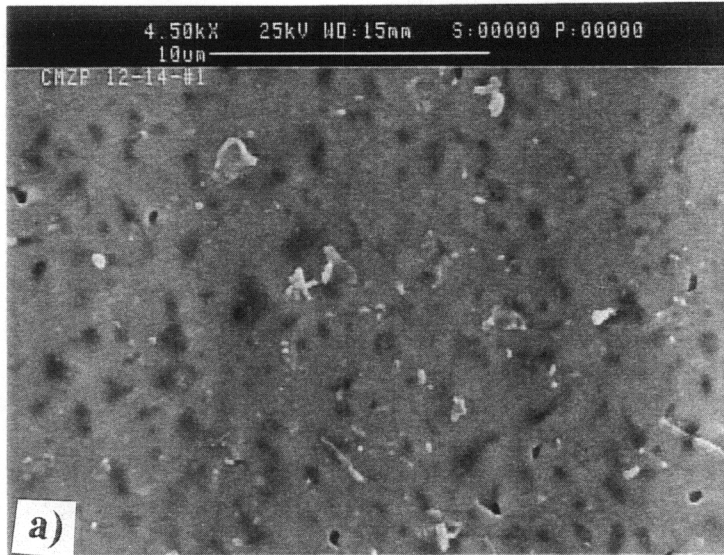


Figure 4.28 Micrographs of slip cast sample (12-14) at: a) 4.5kX and b) 10.5kX

1.5wt%. As stated previously, below the minimum Mean ALPHA temperature, ZnO is believed to enhance diffusional sintering by forming $ZnZr(PO_4)_2$ with residual ZrP_2O_7 . The microstructures of these three slip cast samples strongly support this concept.

4.5 Effects of Processing on Coefficient of Thermal Expansion (CTE)

4.5.1 Dry Pressed Samples

The dry pressed samples from the experimental design were analyzed to 1000°C at 5°C/min. and the resulting data was reduced using the RS1 statistical program. The average CTE at 700 and 1000°C was obtained by using the Mean ALPHA value generated by the Theta program at the given temperatures, as detailed in Section 3.5. The following CTE values were obtained.

Table 4.5 Coefficient of Thermal Expansion Values of Dry Pressed Samples

Sample ID	Time	Temperature	%ZnO	CTE@700°C	CTE@1000°C
(1)	0.5 h	1250°C	1.0%	1.4 ppm/°C	1.8 ppm/°C
(A)	4 h	1250°C	1.0%	-1.7 ppm/°C	-1.3 ppm/°C
(B)	0.5 h	1300°C	1.0%	-0.9 ppm/°C	-0.4 ppm/°C
(AB)	4 h	1300°C	1.0%	-1.5 ppm/°C	-1.1 ppm/°C
(C)	0.5 h	1250°C	3.0%	-1.8 ppm/°C	-0.9 ppm/°C
(AC)	4 h	1250°C	3.0%	-2.0 ppm/°C	-1.2 ppm/°C
(BC)	0.5 h	1300°C	3.0%	-1.9 ppm/°C	-0.9 ppm/°C
(ABC)	4 h	1300°C	3.0%	-2.0 ppm/°C	-1.4 ppm/°C
(0.5B)	0.5 h	1300°C	0.5%	0.6 ppm/°C	1.2 ppm/°C
(-400)	8 h	1300°C	0	1.0 ppm/°C	1.3 ppm/°C

RS1 statistical analysis proved that Time, %ZnO, and their interaction were the most significant factors affecting CTE, accounting for over 56% of the variability. Optimized contour

plots (Figure 4.29) illustrate the effects of Time and %ZnO on CTE for a constant sintering temperature. Separate analyses were performed due to the non-linearity of the data. Both plots show that for a given ZnO level, CTE decreases as firing time is increased, which is in agreement with previous studies by T.K. Li et al.⁶ These contour plots also predict a zero point at which CTE changes from positive to negative. For a 0.5 h firing time, the RS1 calculated CTE transition point is in the range of 1.3 to 1.5% ZnO for a sintering temperature of 1225 to 1250°C.

The CTE data can be broken down into two basic categories, positive and negative. The lower bulk density samples [(1), (0.5B), and (-400)], which exhibited the finer grained microstructure void of a liquid phase and microcracks yielded positive CTE values. The lack of microstructural defects allows CMZP to maintain its inherent positive CTE⁶. The absence of microcracks, which is controlled by grain size^{28,29}, does not allow the positive expansion along the c-axis to be absorbed by crack healing and therefore dictates an overall positive bulk CTE⁶. Additionally, given that bulk thermal expansion of CMZP decreases with decreasing Mg⁺² content⁶, the absence of a liquid phase in the material further assures a positive CTE since Mg⁺² was shown to migrate from the CMZP grains to the grain boundaries and form Zn₂Mg(PO₄)₂, as previously described in Section 4.1.1.

The remaining dry pressed samples, which contained microstructural defects (large grain size, microcracking, and liquid phase formation), all exhibited negative thermal expansion. The samples which were fired for 4 hours [(A), (AB), (AC), and (ABC)] had the most negative values. This strong influence of time supports the idea that Mg⁺² diffuses to the grain boundaries, which pushes the CTE of the CMZP grains towards negative values. The consequence of this migration is microcracking, and therefore a negative CTE, resulting from both greater CTE mismatch between the grains and grain boundaries and grain growth. An improvement in microcrack healing

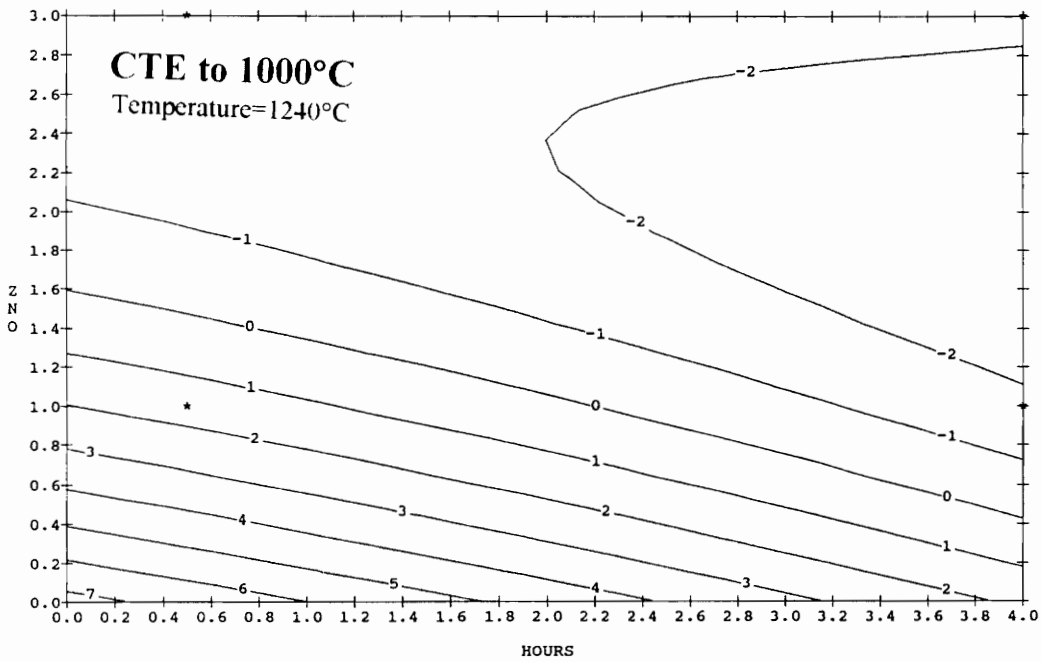
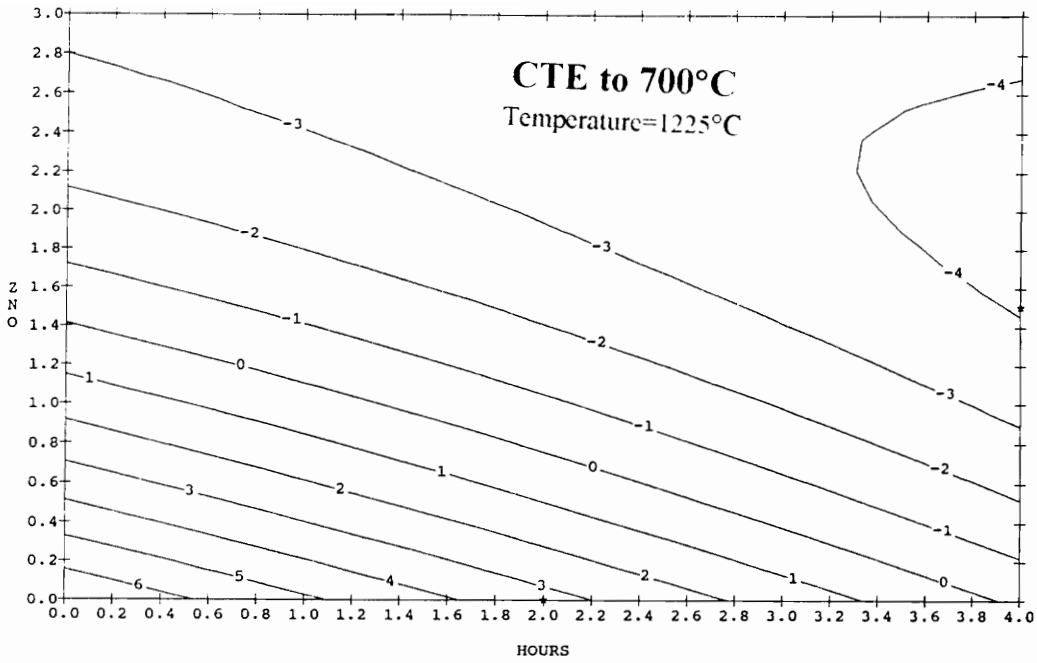


Figure 4.29 RS1 generated CTE contour plots for dry pressed samples

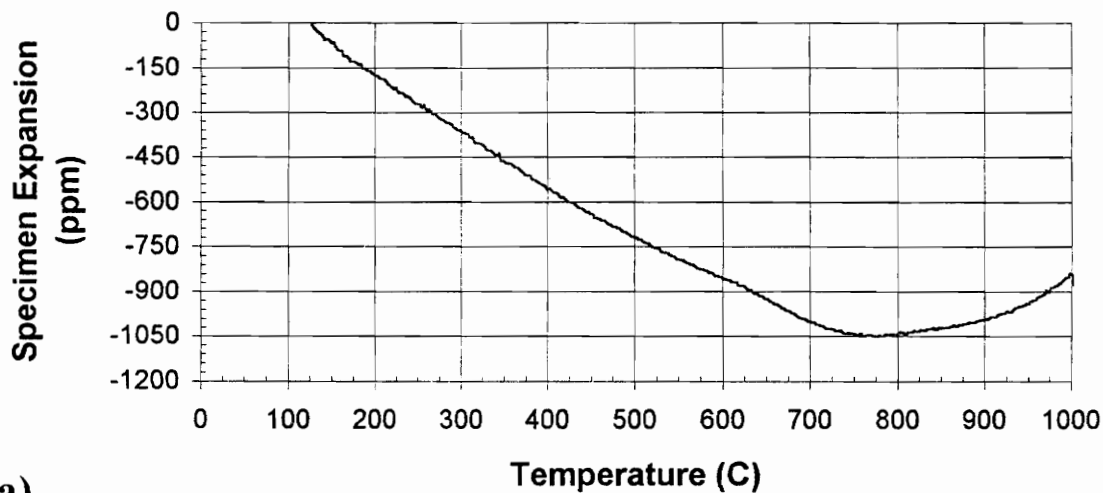
with ZnO content is proposed given the non-linear regions beyond 700°C with the higher ZnO samples [(C), (AC), (BC), and (ABC)]. Beyond 700°C, these samples began to expand (Figure 4.30), signaling microcrack healing. This improvement is probably a result of the positive expansion of the grain boundary phase complimenting the effect of the c-axis expansion. As shown in the micrographs of the higher ZnO samples, the CMZP grains were completely surrounded by the grain boundary phase, preventing grain-to-grain contact, which allows the grain boundary phase to have a significant influence on the thermal expansion of the material.

Sample (1) exhibited an almost linear expansion curve with temperature, while samples (0.5B) and (-400), which had the lower ZnO contents, produced an unusual curved response to 700°C (Figures 4.31, 4.32a, and 4.32b, respectively). Thereafter, their responses were nearly linear. This “hump” in the expansion curve was also somewhat evident in sample (1), but not nearly to the degree as with the lower ZnO samples (0.5B) and (-400). Given that sample (-400), which did not have any ZnO, produced the most pronounced “hump”, it appears that this non-linear region diminishes with ZnO level, as compared to the other samples with 0.5 and 1.0wt% ZnO. This “hump” or “kink” in the thermal expansion profile was also witnessed previously by W. Russ³⁰ with hot pressed sol-gel synthesized CMZP powder.

4.5.2 Slip Cast Samples

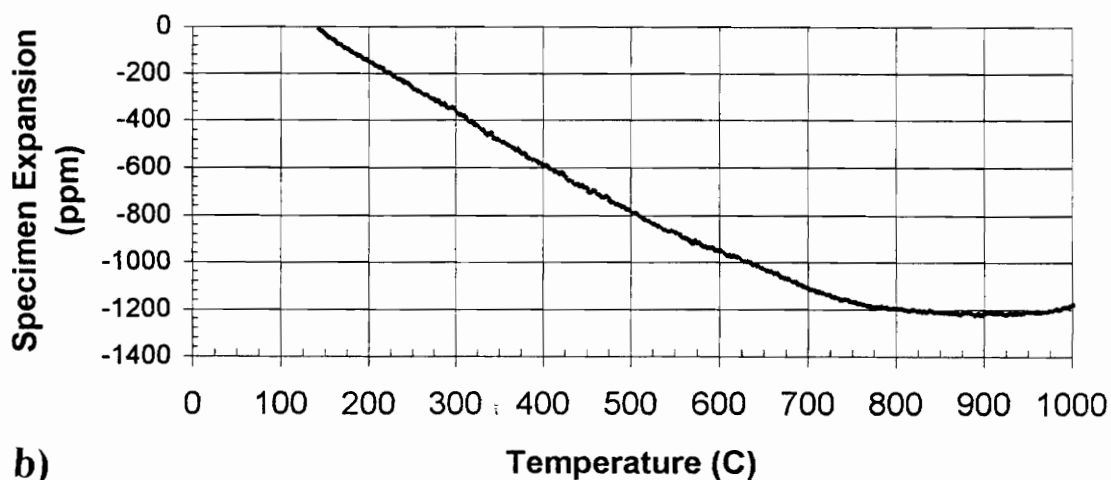
The three fully characterized slip cast samples [(12-1), (12-4), and (12-14)] were also tested to 1000°C at 5°C/min. to obtain average CTE to 700°C and 1000°C. The following values were obtained.

Dry Pressed CMZP Sample (C)



a)

Dry Pressed CMZP Sample (ABC)



b)

Figure 4.30 Thermal expansion plots to 1000°C for dry pressed samples: a) sample (C) and b) sample (ABC)

Dry Pressed CMZP Sample (1)

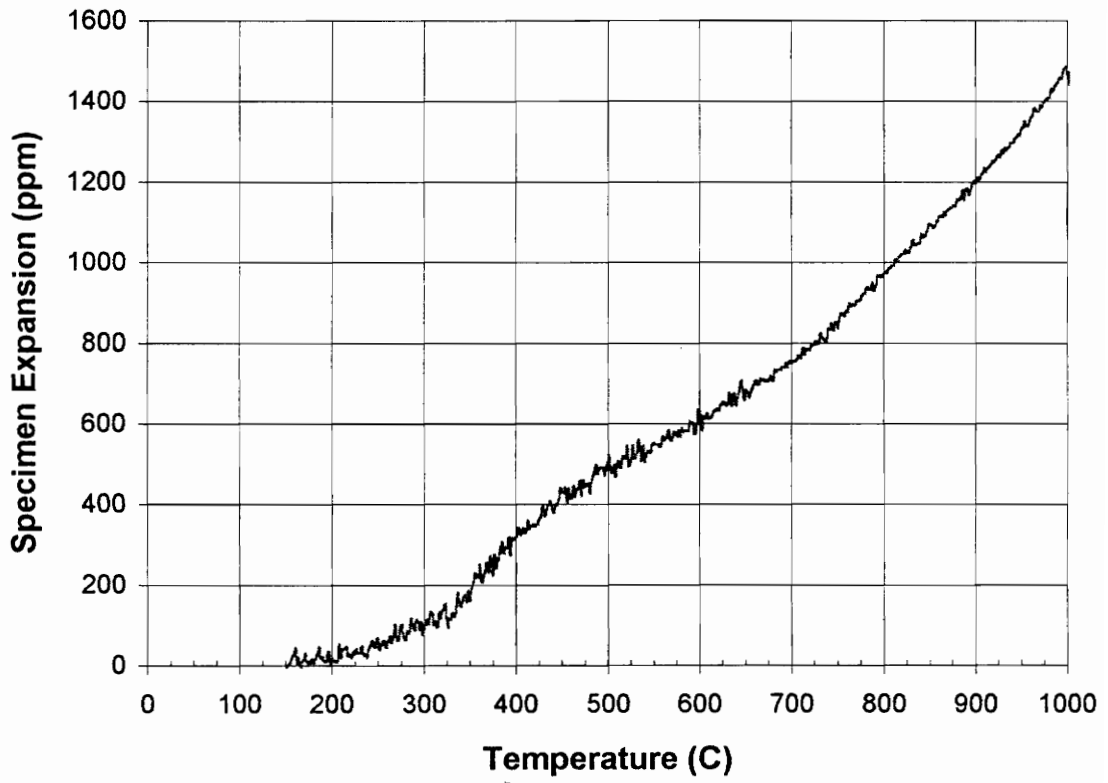


Figure 4.31 Thermal expansion plot to 1000°C for dry pressed sample (1)

Dry Pressed CMZP Sample (0.5B)

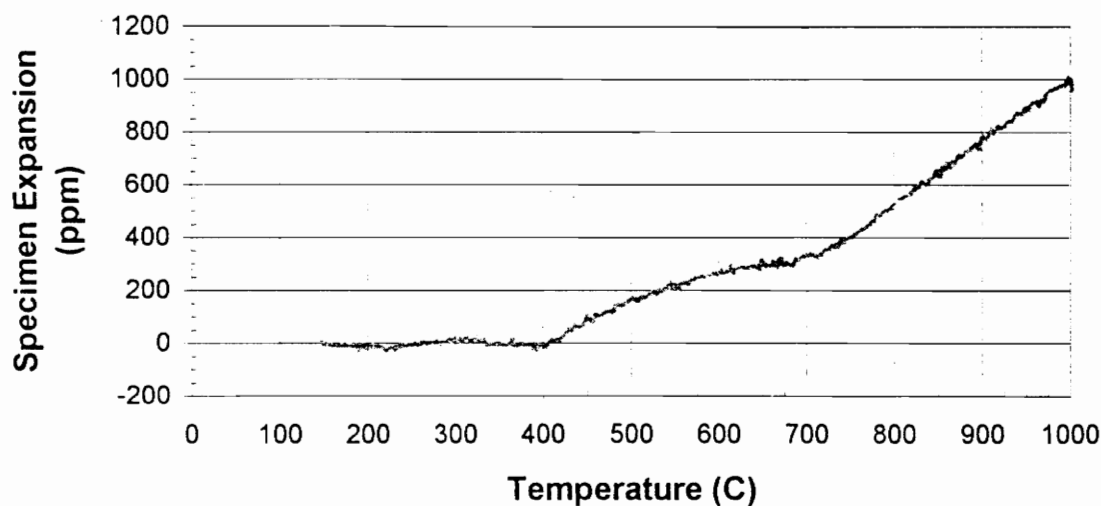


Figure 4.32a Thermal expansion plot to 1000°C for dry pressed sample (0.5B)

Dry Pressed CMZP Sample (-400)

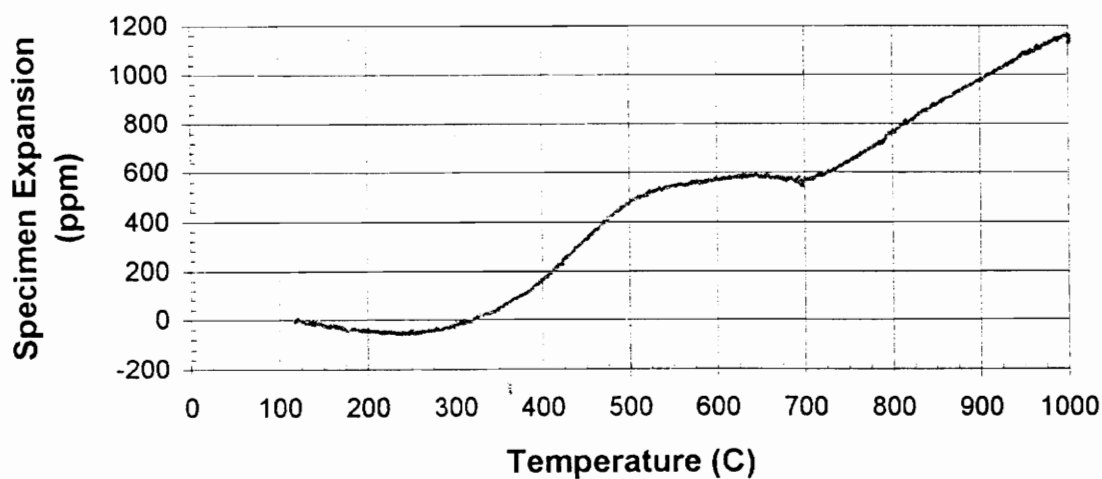


Figure 4.32b Thermal expansion plot to 1000°C for dry pressed sample (-400)

Table 4.6 Coefficient of Thermal Expansion Values of Slip Cast Samples

Sample ID	Time	Temperature	%ZnO	CTE@700°C	CTE@1000°C
(12-1)	0.5 h	1200°C	2.0%	-1.5 ppm/°C	-0.8 ppm/°C
(12-4)	0.7 h	1175°C	2.0%	1.8 ppm/°C	2.0 ppm/°C
(12-14)	0.5 h	1200°C	1.5%	1.8 ppm/°C	2.0 ppm/°C

These results exactly parallel the relationships discussed regarding the dry pressed samples. Once again, microstructure dictated the type of thermal response generated. The microstructural defects generated by the onset of liquid phase sintering, as shown in sample (12-1) (Figures 4.26a and 4.26b), forced the thermal expansion negative (Figure 4.33a). This sample also exhibited the crack healing response of sample expansion, similar to the dry pressed samples, above 700°C.

Furthermore, the positive expansion samples [(12-4) and (12-14)] produced the same “kink” in the thermal response profile (Figure 4.33b). However, the kink was seen at a lower temperature and was also less distinct as compared to the dry pressed samples

Hysteresis plots were also generated for samples (12-1) and (12-4) (Figures 4.33a and 4.33b). The large hysteresis response of sample (12-1) further illustrates the significant effect of microcracking on thermal expansion. Therefore, microcracking of CMZP samples results in both negative CTE and a significant hysteresis response upon cooling from temperature. Likewise, sample (12-4), which had a microstructure void of microcracking, had a positive expansion and a negligible hysteresis curve. Given that these two samples contained the same level of ZnO sintering aid, the importance of sintering temperature on microstructure and resulting material properties was clearly demonstrated.

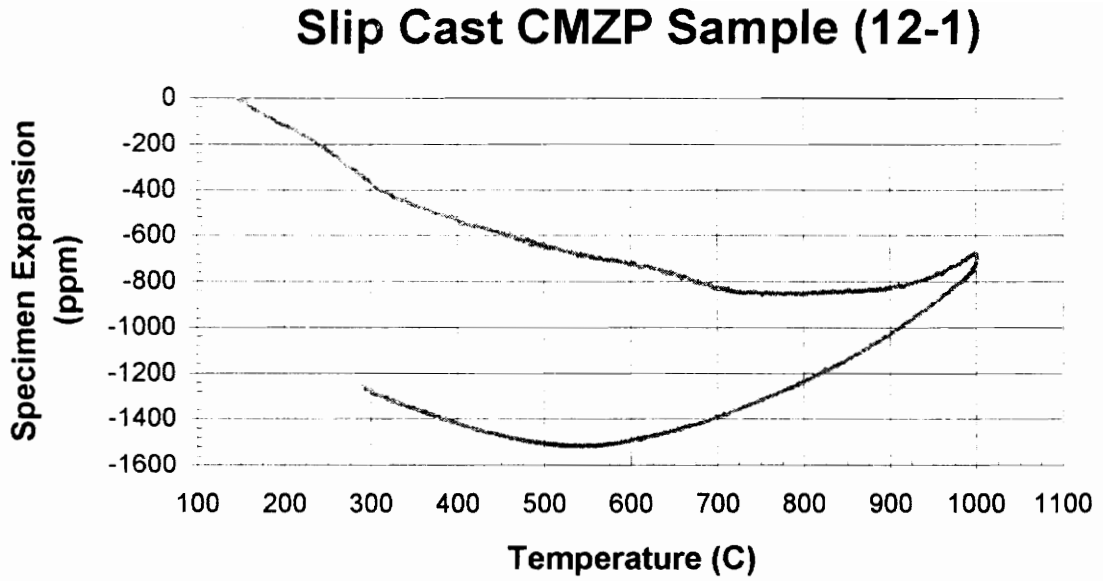


Figure 4.33a Hysteresis plot to 1000°C of slip cast sample (12-1)

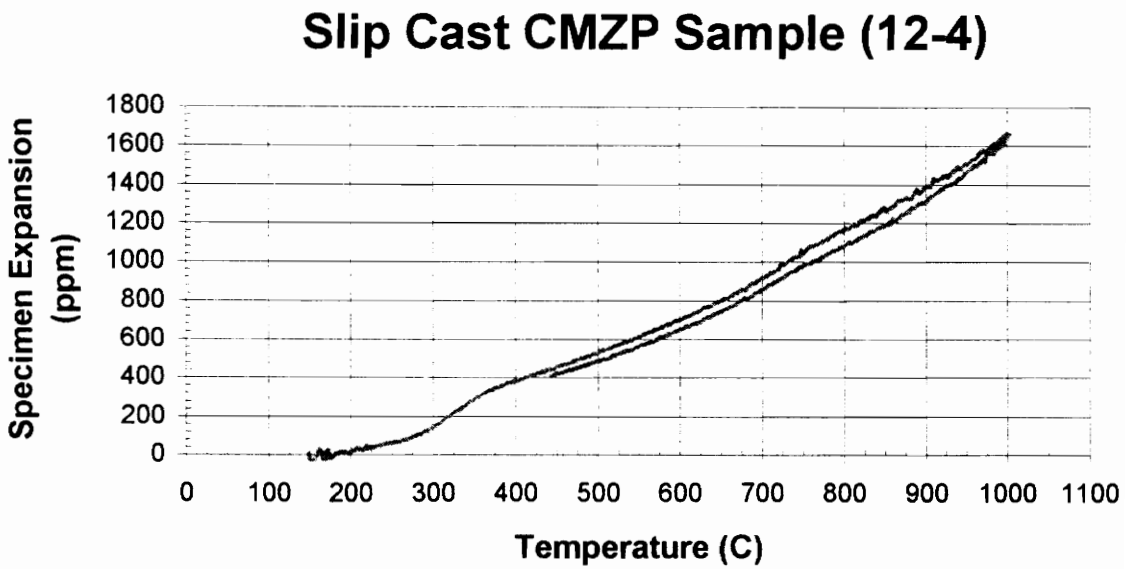


Figure 4.33b Hysteresis plot to 1000°C of slip cast sample (12-4)

4.6 Effects of Processing on Modulus of Rupture (MOR)

4.6.1 Dry Pressed Samples

Statistical analyses revealed that of the main factors, Time was most dominant for controlling MOR. However, when the quadratic terms were taken into account, the square of the ZnO level was almost equally as dominant. The combination of these two terms accounted for about 50% of the variability in the matrix. The following MOR values were obtained in 4-pt. bending.

Table 4.7 MOR Values of Dry Pressed Samples

Sample	Time	Temperature	%ZnO	MOR	STD DEV
(1)	0.5 h	1250°C	1.0%	26.4 MPa	2.5 MPa
(A)	4 h	1250°C	1.0%	13.3 MPa	1.2 MPa
(B)	0.5 h	1300°C	1.0%	12.3 MPa	3.2 MPa
(AB)	4 h	1300°C	1.0%	15.7 MPa	2.3 MPa
(C)	0.5 h	1250°C	3.0%	21.3 MPa	0.7 MPa
(AC)	4 h	1250°C	3.0%	17.8 MPa	1.7 MPa
(BC)	0.5 h	1300°C	3.0%	20.8 MPa	1.0 MPa
(ABC)	4 h	1300°C	3.0%	17.4 MPa	0.8 MPa
(0.5B)	0.5 h	1300°C	0.5%	27.6 MPa	1.6 MPa
(-400)	8 h	1300°C	0%	19.3 MPa	1.9 MPa

An RS1 generated contour plot (Figure 4.34) illustrates the effects of processing changes at a constant temperature. For ZnO levels below 1.5wt%, MOR follows a parabolic function where maximum values are produced after approximately 2 h at temperature. It was also calculated that MOR increases as ZnO is reduced for a constant sintering time and temperature. These effects support the hypothesis that ZnO, up to a certain level, improves densification by enhancing the diffusional sintering process. The optimal ZnO concentration is most likely related to the amount of residual zirconium phosphate (ZrP_2O_7) in the starting powder, which was not determined in this

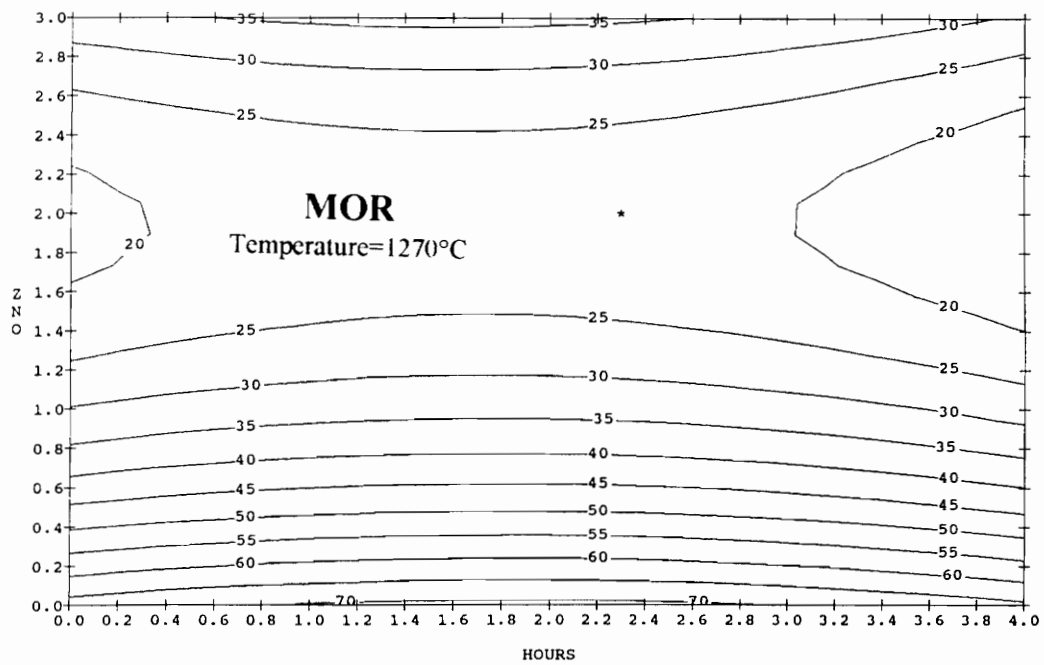
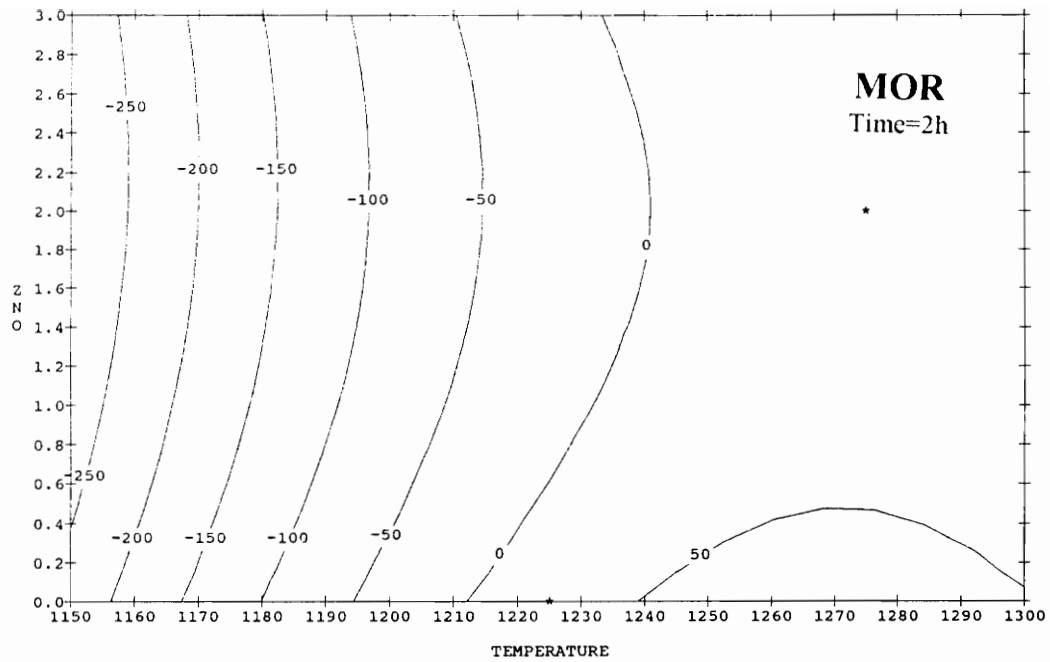


Figure 4.34 RSI generated MOR contour plots for dry pressed samples

study. ZnO levels beyond this optimal point promote liquid phase sintering which was shown to adversely affect the mechanical and thermal properties of CMZP.

The fracture surfaces of all the dry pressed samples (Figures 4.35-4.39) further strengthen the premise of an undesired transition from diffusional to liquid phase sintering, a concept that was first hypothesized from microstructural analysis and then later from viewing fracture surfaces of samples sintered at different temperatures. The only samples which exhibited transgranular fracture, seen as a relatively smooth fracture surface, were (1), (0.5B), and (-400). These three samples were also the least dense of the dry pressed samples, 2.46 g/cc, 2.51 g/cc, and 2.31 g/cc, respectively. However, samples (1) and (0.5B) were the strongest of the dry pressed samples despite their low density. The low strength of sample (-400) might be a result of the long firing time, which has been shown detrimental to MOR in this study as well as past studies by Yamai and Oota^{31,32}. The remaining dry pressed samples all exhibited intergranular fracture, denoting that microstructural defects, specifically liquid phase grain boundaries and microcracks, are controlling the properties, rather than the CMZP grains themselves. This shift in fracture mode, defined as a faceted, rock-candy like surface, was also observed in the previously described analysis of microstructure versus sintering temperature in Section 4.2.2.

4.6.2 Slip Cast Samples

As expected, the relationships determined in the dry pressed study held true for slip cast samples as well. The following MOR values were obtained.

Table 4.8 MOR Values of Slip Cast Samples

Sample ID	Time	Temperature	%ZnO	MOR	STD DEV
(12-1)	0.5 h	1200°C	2.0%	27.6 MPa	2.8 MPa
(12-4)	0.5 h	1175°C	2.0%	111.3 MPa	25.7 MPa
(12-14)	0.5 h	1200°C	1.5%	95.7 MPa	15.1 MPa

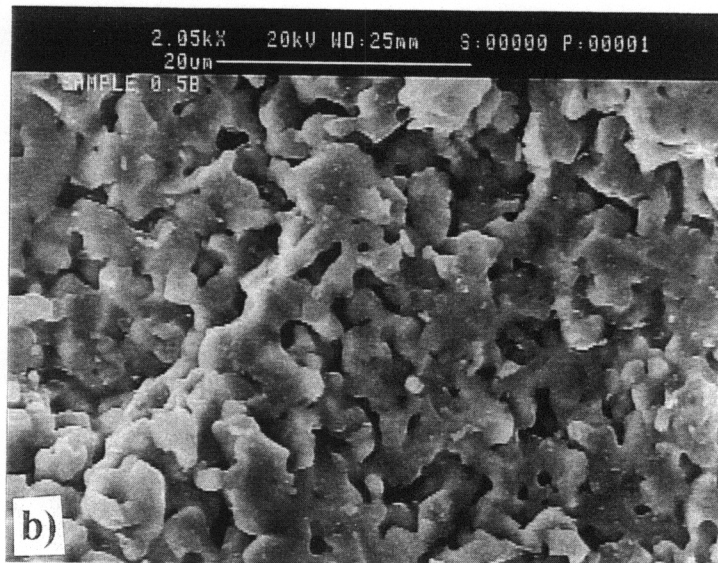
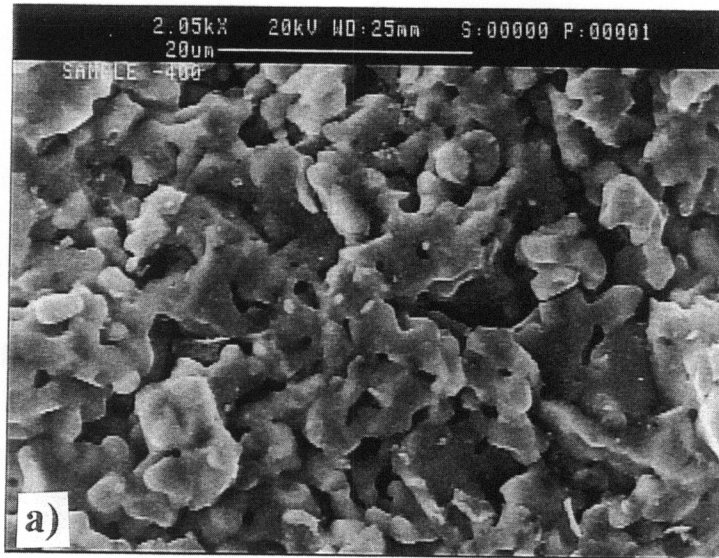


Figure 4.35 MOR bar fracture surface micrographs of dry pressed samples: a) sample (-400) and b) sample (0.5B)

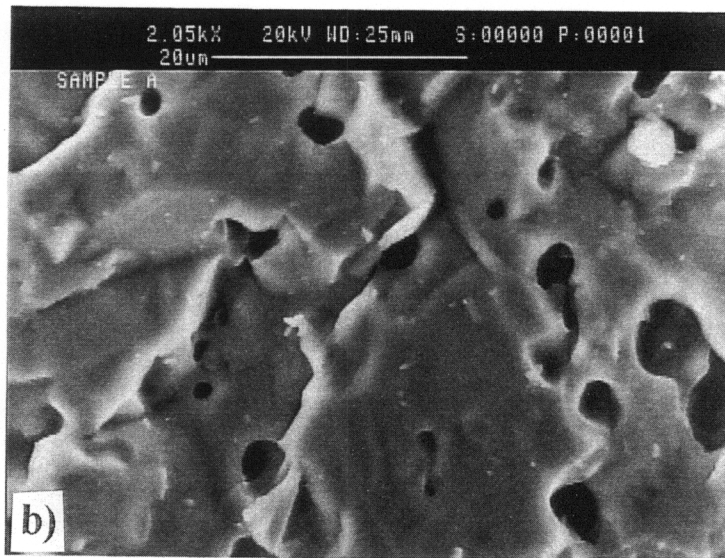
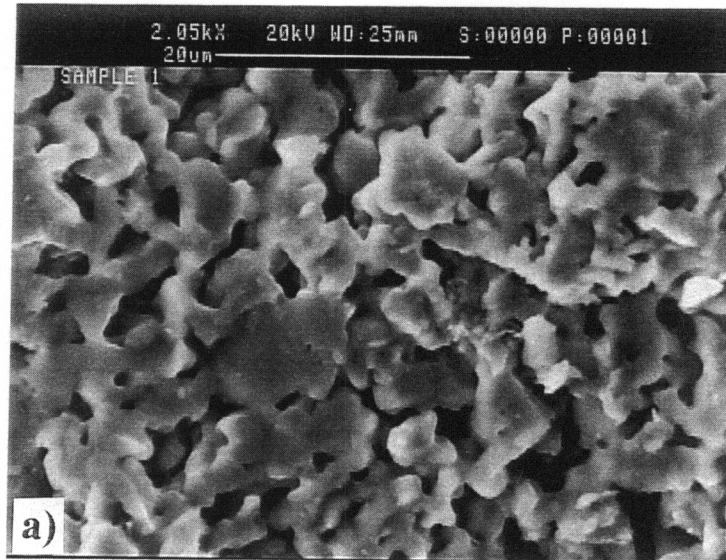


Figure 4.36 MOR bar fracture surface micrographs of dry pressed samples: a) sample (1) and b) sample (A)

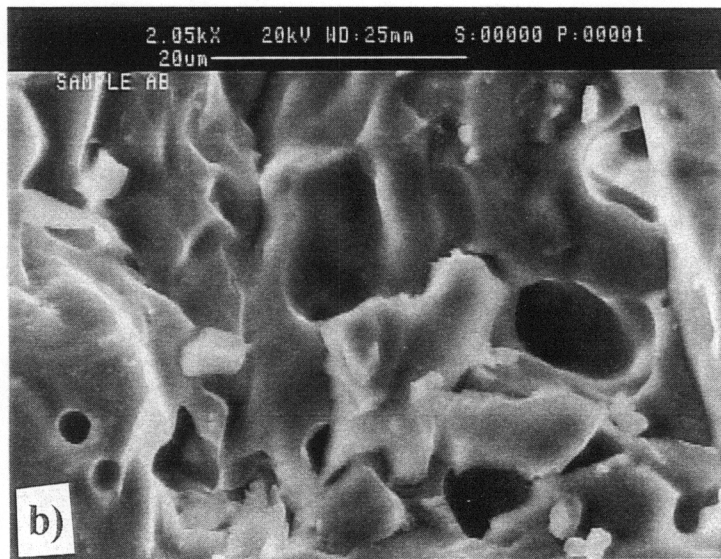
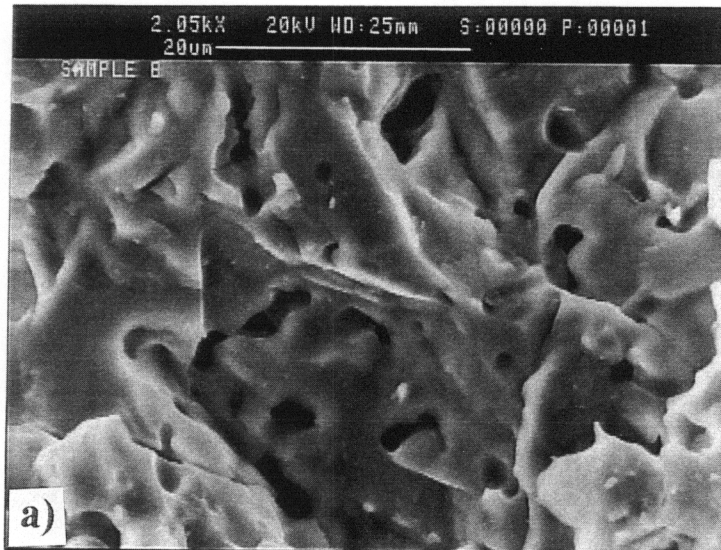


Figure 4.37 MOR bar fracture surface micrographs of dry pressed samples: a) sample (B) and b) sample (AB)

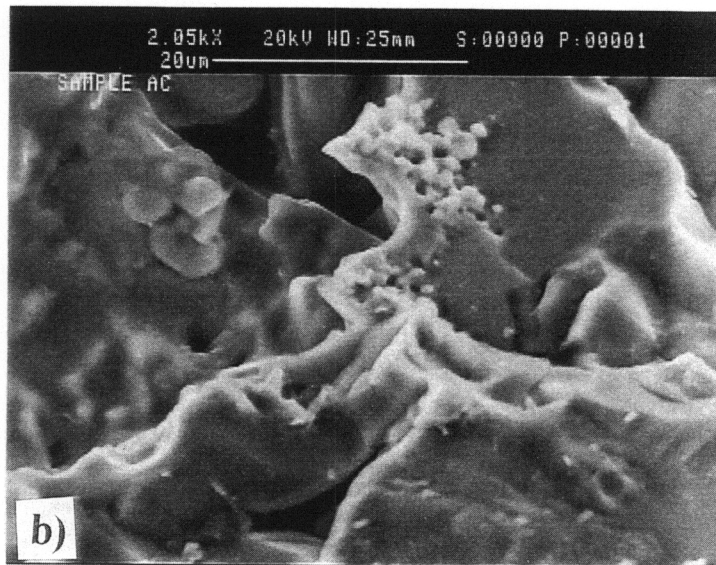
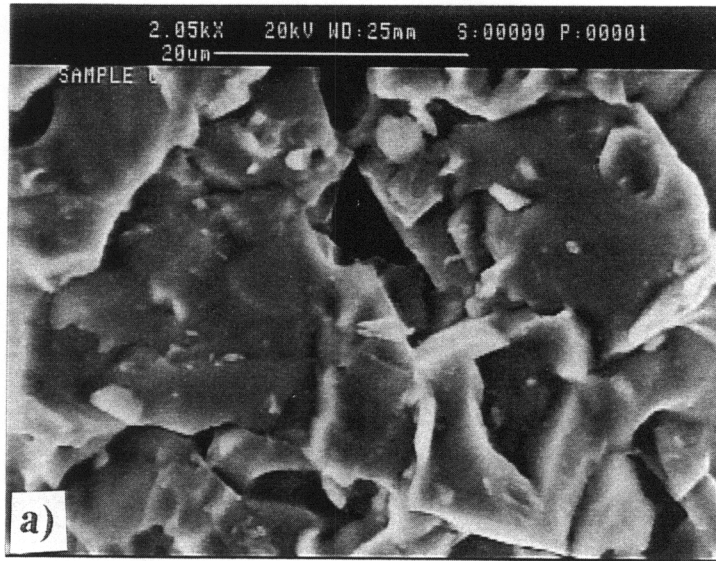


Figure 4.38 MOR bar fracture surface micrographs of dry pressed samples: a) sample (C) and b) sample (AC)

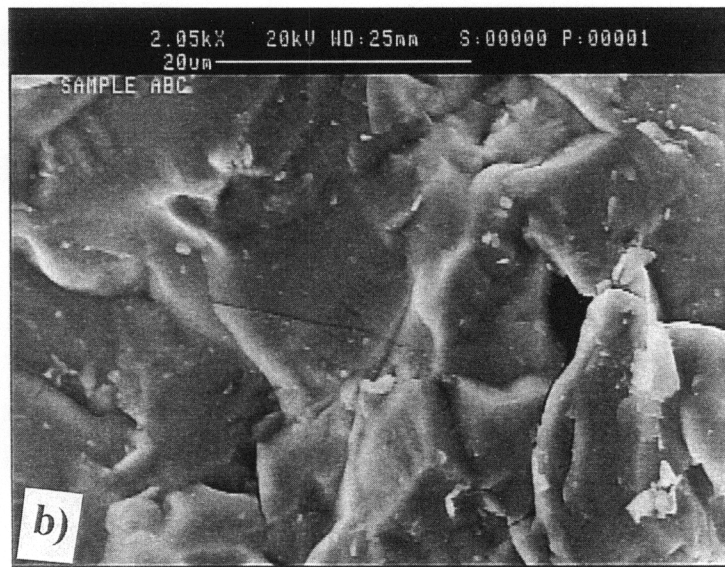
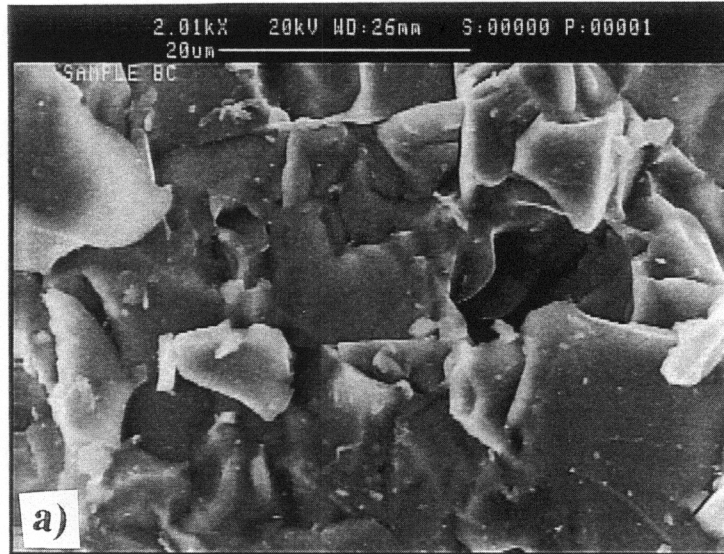


Figure 4.39 MOR bar fracture surface micrographs of dry pressed samples: a) sample (BC) and b) sample (ABC)

The small difference in sintering temperature from sample (12-1) to (12-4), which resulted in a significant increase in MOR, details the important relationship between firing temperature and ZnO level and its effect on MOR. Although a statistical analysis was not performed using the slip cast data, Temperature, which proved less significant than Time and ZnO for the dry pressed samples, is assumed to be a dominant factor considering the small temperature range for which a large change in properties was seen. This difference is probably a result of the smaller particle size and the more homogenous composition produced by the slip cast process. The smaller particle size and lack of agglomerates makes for a more reactive composition and therefore allows temperature to assume a more dominant role in controlling the final properties.

The fracture surfaces of the three slip cast samples agree very well with their respective MOR values. Sample (12-1), which generated the lowest MOR value (27.6 MPa), exhibited the faceted fracture surface (Figure 4.40) associated with intergranular fracture (grain boundary/microcracked controlled). The remaining slip cast samples, (12-4) and (12-14), which had MOR values over three times that of sample (12-1), exhibited the smooth fracture surfaces associated with transgranular fracture (Figures 4.41 and 4.42). Comparing the micrographs of these two high strength samples, it is seen that sample (12-4), which had the higher ZnO content, did not have as a distinct grain structure as did sample (12-14).

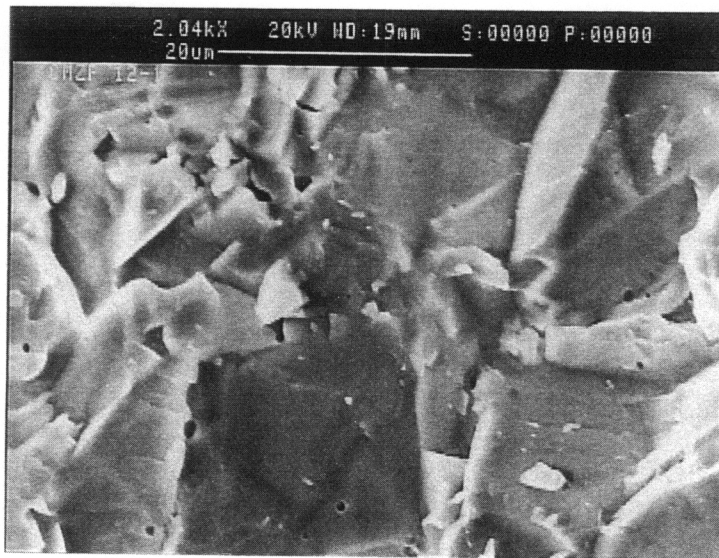
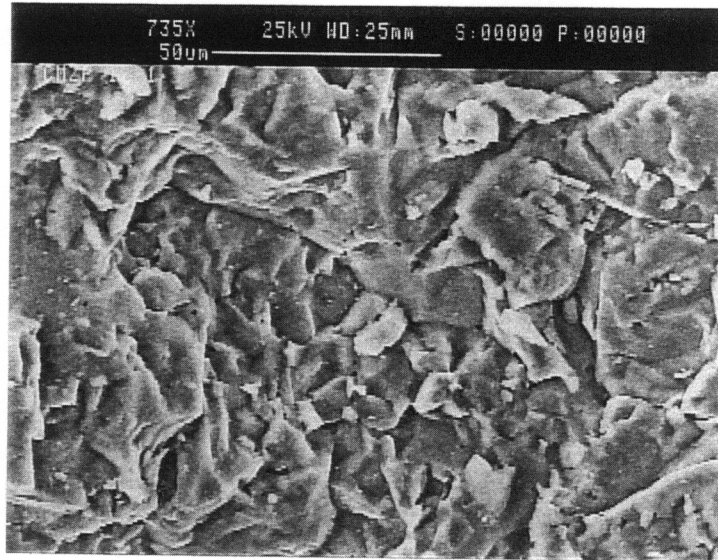


Figure 4.40 MOR bar fracture surface micrographs of slip cast sample (12-1)

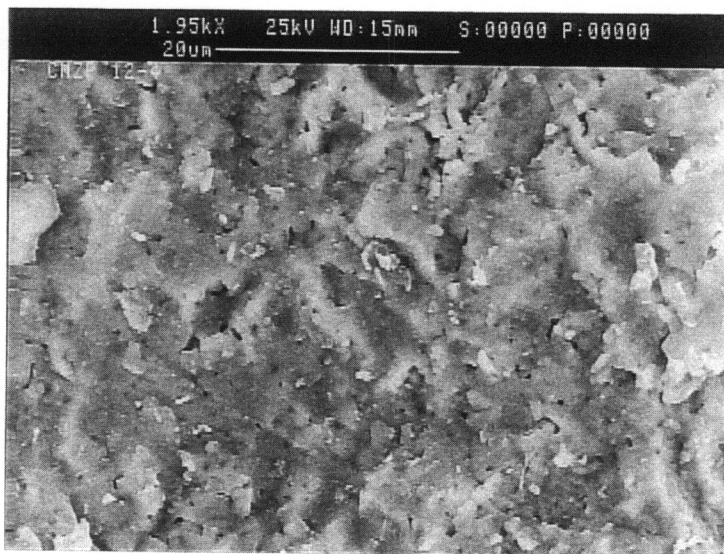
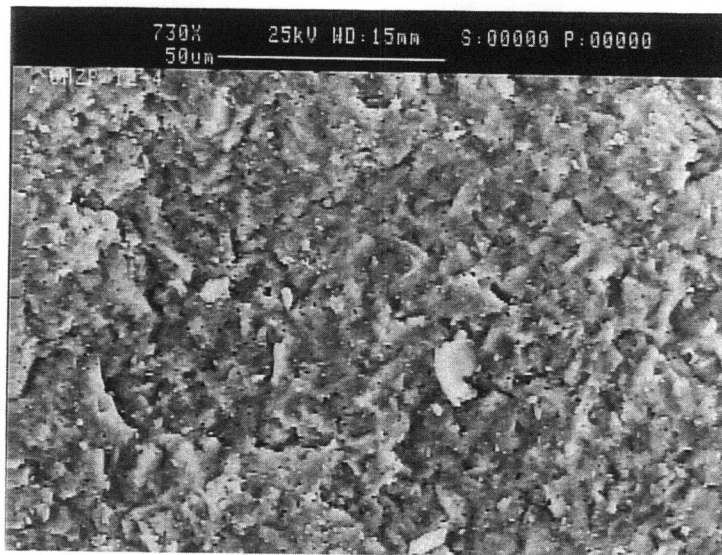


Figure 4.41 MOR bar fracture surface micrographs of slip cast sample (12-4)

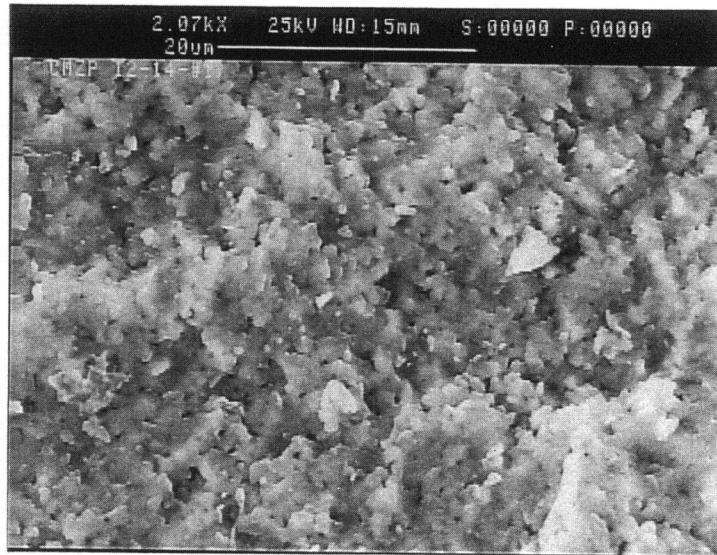
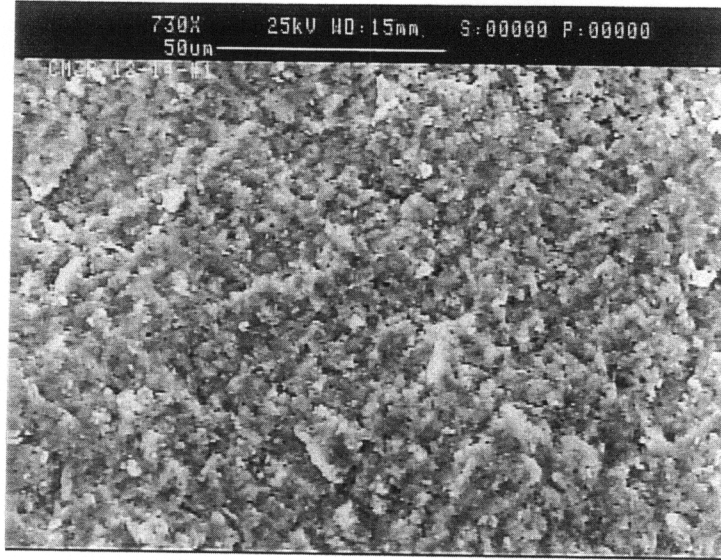


Figure 4.42 MOR bar fracture surface micrographs of slip cast sample (12-14)

5. DISCUSSION

5.1 The Effects Processing on CMZP Ceramics

5.1.1 Sintering Temperature

When sintering CMZP with ZnO, temperature dictates the sintering mechanism, either solid-state (diffusional) or liquid phase, which in turn controls the type of microstructure developed and the resulting physical properties. The onset of liquid phase sintering, which results in subsequent grain growth, is temperature controlled and is responsible for an overall degradation in microstructure and properties of CMZP ceramics. The most fundamental microstructural flaw, which controls both MOR and CTE, is the development of microcracks due to excessive grain growth. Given that the relationship between grain size and microcracking for materials with thermal expansion anisotropy such as CMZP was already established^{28,29}, the critical grain size for spontaneous microcracking in CMZP was estimated to be 8-10 μm by T.K. Li et al.²⁴ The presence of a liquid phase, which is controlled by sintering temperature, promotes grain growth and allows the grain size to exceed the critical value for spontaneous microcracking. This effect of sintering temperature was independent of forming method (dry pressed versus slip cast) and was shown to be a function of ZnO level. This relationship between sintering temperature and ZnO level will be further detailed in Section 5.2.

5.1.2 Sintering Time

The effect of sintering time is similar to that of temperature in that it influences the grain size of the sintered material. Short sintering times of less than 1 h were needed to keep the grain size below the critical value and to prevent spontaneous microcracking. The shortest sintering time

tested was 0.5 h; however, shorter times of 0.17 to 0.33 h might prove optimal given the research of Yamai and Oota^{31,32} who determined that maximum MOR values developed in less than 0.5 h for zirconium phosphate ceramics sintered with metal oxides such as ZnO.

5.1.3 ZnO Additions

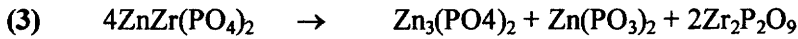
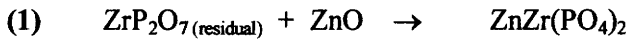
The amount of ZnO sintering aid used determines the sintering temperature at which liquid phase sintering is initiated, as will be further discussed in Section 5.2. For a given sintering time and temperature, increases in ZnO levels resulted in higher bulk densities at the expense of degradations in both microstructure and physical properties. Another consequence of increased ZnO levels may be a reduction in the maximum use temperature of the material, as will be discussed in Section 5.4.

5.2 The Significance of the Minimum Mean ALPHA Temperature with Respect to ZnO Additions

The minimum Mean ALPHA temperature has been shown to be approximately the transition temperature at which a dramatic change in microstructure and physical properties occur. This rapid change was especially evident in the slip cast samples where a 25°C increase in firing temperature above the minimum Mean ALPHA temperature resulted in a decrease in MOR of over 300% and the CTE being pushed negative.

Given that this temperature corresponds to the temperature range at which new phases begin to form in the X-Ray patterns, reactions are assumed, mostly likely the melting of a phosphate phase formed by the addition of ZnO. Since ZnO first forms $\text{ZnZr}(\text{PO}_4)_2$ with the unreacted ZrP_2O_7 , it is proposed that the minimum Mean ALPHA temperature corresponds with the melting of this phase.

The following reactions are suggested:



The first reaction, and its corresponding reaction product, $\text{ZnZr(PO}_4)_2$, is the possible source of the increase in solid-state (diffusional) sintering up to the minimum Mean ALPHA temperature. The second and third reactions, which mark the initiation of liquid phase sintering, are responsible for the dramatic changes in microstructure and physical properties beyond the minimum Mean ALPHA temperature. The reactivity of the zinc phosphate phases is most likely the cause of the sudden grain growth and the leaching of the Mg^{+2} ions out of the CMZP structure, both of which are not without consequence to mechanical and thermal properties. If all three of these reactions hold true, tight control over ZnO levels and sintering temperatures is imperative since the formation of a liquid phase is impossible to avoid when using ZnO as a sintering aid. These proposed reactions also place a limit on the temperature range at which the material can be used without degradation of microstructure and properties, as will be discussed in Section 5.4.

All of these reaction products, except for $\text{Zn}_3(\text{PO}_4)_2$, were identified in the XRD patterns. A substitution of Mg^{+2} ions into the $\text{Zn}_3(\text{PO}_4)_2$ structure is assumed since XRD data indicated $\text{Zn}_2\text{Mg(PO}_4)_2$ was present at temperatures beyond this proposed transition temperature. Additionally, EDS analysis confirmed the grain boundary phase to be rich in Mg^{+2} and Zn^{+2} . This reaction product is logical since previous studies^{22,32} have assumed the formation of $\text{Zn}_3(\text{PO}_4)_2$ when sintering zirconium phosphates with ZnO.

From these proposed reactions, it is suggested that the optimal ZnO level is based on the amount of residual ZrP_2O_7 , which is controlled by the accuracy of the batch composition during

synthesis and the degree of calcination prior to sintering. If the previous reactions are assumed true, the optimum ZnO level should be relatively large given the 1-to-1 ratio of ZnO to ZrP_2O_7 in the first equation and the large amounts of ZrP_2O_7 seen in the XRD patterns up to about 1000°C . However, it must be remembered that the ZnO should be reacting with the residual zirconium phosphate, which should be very small, since the majority of the ZrP_2O_7 is crystallized into CMZP upon heat treatment. Therefore, the optimal level of ZnO is not easily determined and probably varies slightly from batch to batch. Furthermore, small ZnO additions beyond this optimal level are detrimental given the 1-to-3 ratio of ZnO to $ZnZr(PO_4)_2$ in the second equation. This proposed parabolic effect of ZnO additions is supported by the significance of the square of the ZnO level term in the MOR statistical analysis, which accounted for over 25% of the variability in that data. The effect of too high a ZnO level and/or too high a firing temperature, both of which are predicted by equations (2) and (3), was demonstrated in both the dry pressed and the slip cast samples.

5.3 The Relationships Between Bulk Density, MOR, and CTE

The results of the bulk density, MOR, and CTE testing, including microstructure, as a function of processing has already been presented individually in Chapter 4. An attempt will now be made to explain how all of these properties are interrelated and are microstructurally, and therefore process, controlled. These relationships between processing, microstructure, and properties are the basis of materials science and are the crux of most materials research.

Perhaps the most interesting relationship exhibited by CMZP ceramics, when sintered with ZnO, is the counterintuitive, nonproportionality of bulk density and MOR. Unlike the majority of ceramic materials, maximizing bulk density did not yield high strength. As shown in the previous

chapter, the higher bulk density samples did not exhibit the high MOR and positive CTE required for the exhaust port design. As shown in Table 5.1, low strength and negative CTE are consistently associated with higher bulk density samples for the given processing method.

Table 5.1 Summary of Physical Property Data versus Processing

Sample ID	Time	Temp.	%ZnO	Bulk Density	MOR	CTE@1000°C
Dry Press						
(1)	0.5 h	1250°C	1.0%	2.46 g/cc	26.4 MPa	1.8 ppm/°C
(A)	4 h	1250°C	1.0%	2.91 g/cc	13.3 MPa	-1.3 ppm/°C
(B)	0.5 h	1300°C	1.0%	2.79 g/cc	12.3 MPa	-0.4 ppm/°C
(AB)	4 h	1300°C	1.0%	2.84 g/cc	15.7 MPa	-1.1 ppm/°C
(C)	0.5 h	1250°C	3.0%	3.02 g/cc	21.3 MPa	-0.9 ppm/°C
(AC)	4 h	1250°C	3.0%	3.08 g/cc	17.8 MPa	-1.2 ppm/°C
(BC)	0.5 h	1300°C	3.0%	3.09 g/cc	20.8 MPa	-0.9 ppm/°C
(ABC)	4 h	1300°C	3.0%	3.07 g/cc	17.4 MPa	-1.4 ppm/°C
(0.5B)	0.5 h	1300°C	0.5%	2.51 g/cc	27.6 MPa	1.2 ppm/°C
(-400)	8 h	1300°C	0%	2.31 g/cc	19.3 MPa	1.3 ppm/°C
Slip Cast						
(12-1)	0.5 h	1200°C	2.0%	3.22 g/cc	27.6 MPa	-0.8 ppm/°C
(12-4)	0.7 h	1175°C	2.0%	3.06 g/cc	111.3 MPa	2.0 ppm/°C
(12-14)	0.5 h	1200°C	1.5%	2.89 g/cc	95.7 MPa	2.0 ppm/°C

One powerful example of how high bulk density does not correlate with high strength is the RS1 optimization calculations for dry pressed bulk density. A bulk density of 3.17 g/cc (>99% of theoretical) was calculated to result when fired to 1227°C for 4 h with 2.22% ZnO. At these same processing conditions, however, the MOR was calculated to be -33 MPa and the CTE at 1000°C was calculated to be -4.3 ppm/°C. Although this MOR value makes no sense, it does prove that the conditions of high bulk density are not the conditions of high strength or positive thermal expansion.

Microstructural analysis revealed the reasons why high bulk density is not a good indicator of high strength. The initiation of liquid phase sintering, which includes the formation of secondary phase grain boundaries, is the mechanism that promotes high bulk density by encouraging grain growth and the elimination of porosity. However, this liquid phase, and the grain growth it promotes, is also the fundamental cause of poor strength and negative thermal expansion since a large grained structure initiates spontaneous microcracking in anisotropic materials such as CMZP. Therefore, the properties of CMZP, when sintered with ZnO, are dictated by microstructure, or more specifically, by the presence of a liquid phase and grain size. This relationship is strongly supported by fracture surface analysis of both the dry pressed and slip cast MOR bars in which the fracture mode changed from transgranular to intergranular when a liquid phase was present. Intergranular fracture, or fracture between the grains, is grain boundary controlled; therefore the strength of the sample is dictated by the strength of the grain boundary phase, not the grains themselves. This problem is compounded by the presence of microcracks, which is also detrimental to strength. This combination of a weak grain boundary phase and microcracked grains is responsible for the dramatic reductions in strength and the change in fracture mode witnessed at the initiation of liquid phase sintering, which, unfortunately, is also the mechanism for obtaining high bulk density. These same microstructural defects also control the thermal expansion of the material by the mechanisms discussed in Section 4.5.1.

5.4 The Consequences of Using ZnO as a Sintering Aid

Although ZnO has proven to be a powerful sintering aid capable of producing dense samples of good strength at temperatures and times far lower than for the pure material alone, this increase in sintering performance is not without consequence. The proposed reactions described in Section 5.2 impose a strict limit on the temperature at which the material can be utilized. This temperature limit is below the sintering temperature, which has been defined as the minimum Mean ALPHA temperature. Fracture surface analysis of slip cast samples (12-4) and (12-14) aged at 800°C, 1000°C, and 1200°C for 100 h revealed the effect of temperature. The lower ZnO content (1.5wt%) sample (12-14) exhibited little change in fracture mode after aging at 800°C (Figure 5.1a). At 1000°C, the fracture surface (Figure 5.1b) did appear to more faceted than before aging. However, at 1200°C, grain growth and microcracking was pronounced resulting in the total dominance of intergranular fracture (Figure 5.2). For the higher (2.0wt%) ZnO sample (12-4), aging at 800°C (Figure 5.3a) resulted in a slightly more faceted fracture surface, and at 1000°C (Figure 5.3b), a coarser, even more faceted fracture surface was seen. By 1200°C, fracture was totally intergranular and grain growth was significant (Figure 5.4), similar to sample (12-14).

These changes in fracture surface indicate a strong progression towards intergranular fracture with temperature and support the idea that grain growth and extensive microcracking are unavoidable at aging temperatures at or above the sintering temperature when ZnO is used as a sintering aid, as discussed in Section 5.2. Also, at the 800 and 1000°C aging temperatures, there appeared to be an increase in overall porosity, possibly due to the volatilization of a low melting point phosphate phase. The effects of these changes on MOR and CTE were not evaluated but are very important and require further investigation.

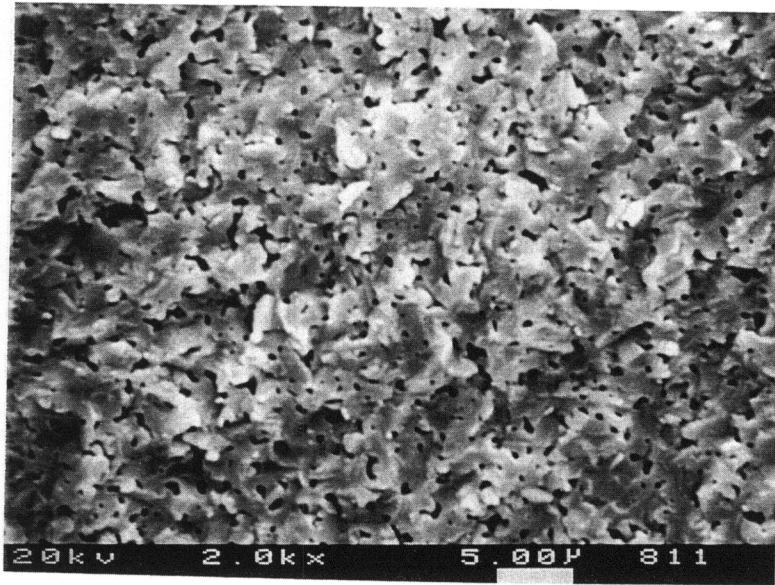


Figure 5.1a MOR bar fracture surface micrograph of slip cast sample (12-14) after thermal aging for 100h at 800°C

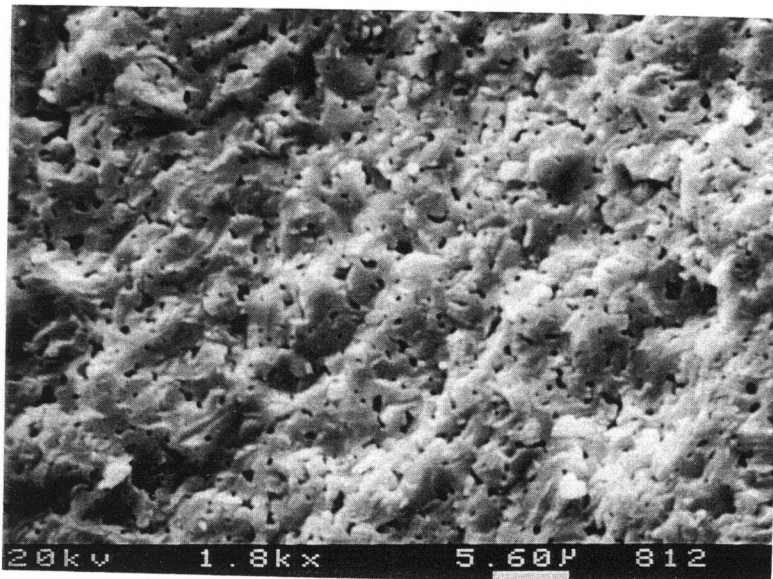


Figure 5.1b MOR bar fracture surface micrographs of slip cast sample (12-14) after thermal aging for 100h at 1000°C

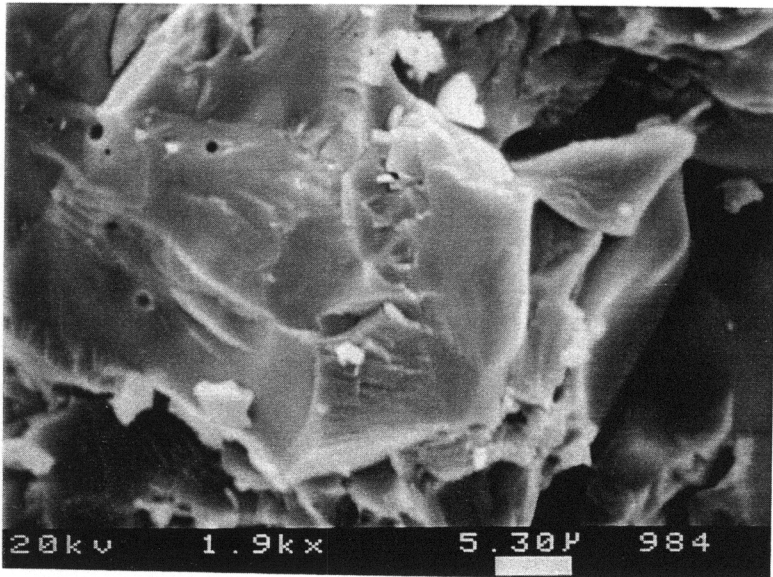
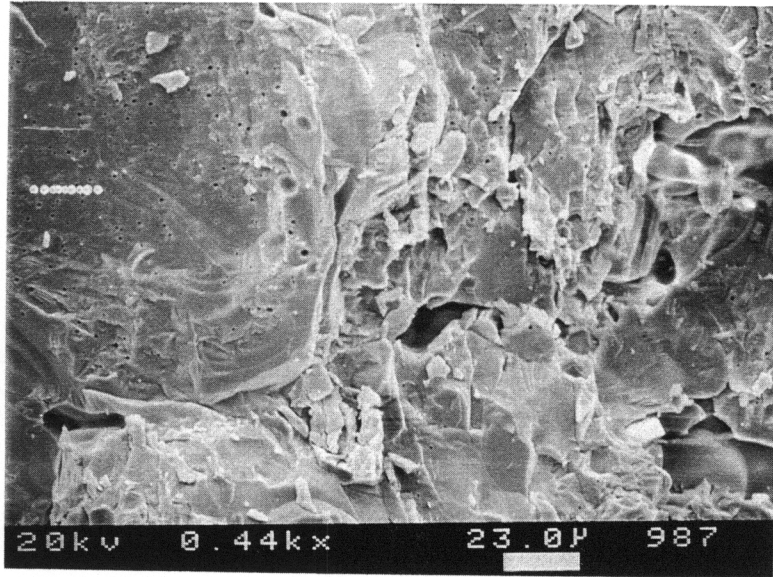


Figure 5.2 MOR bar fracture surface micrographs of slip cast sample (12-14) after thermal aging for 100h at 1200°C

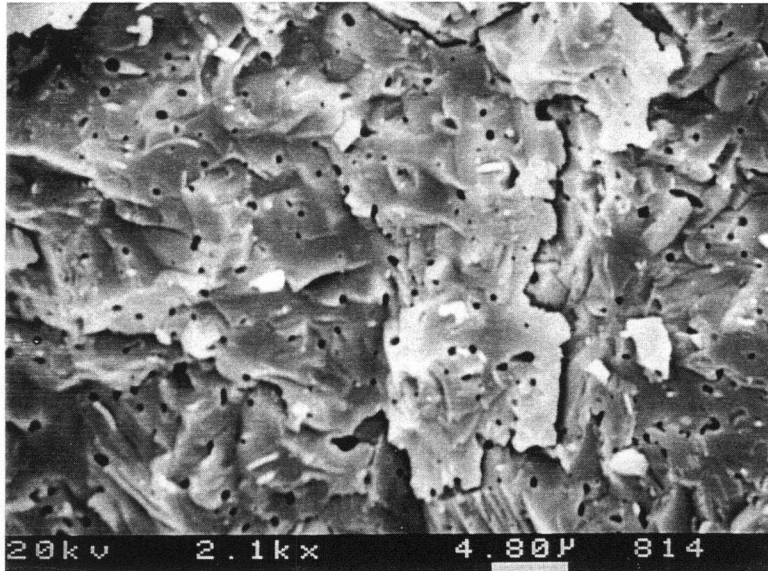


Figure 5.3a MOR bar fracture surface micrographs of slip cast sample (12-4) after thermal aging for 100h at 800°C

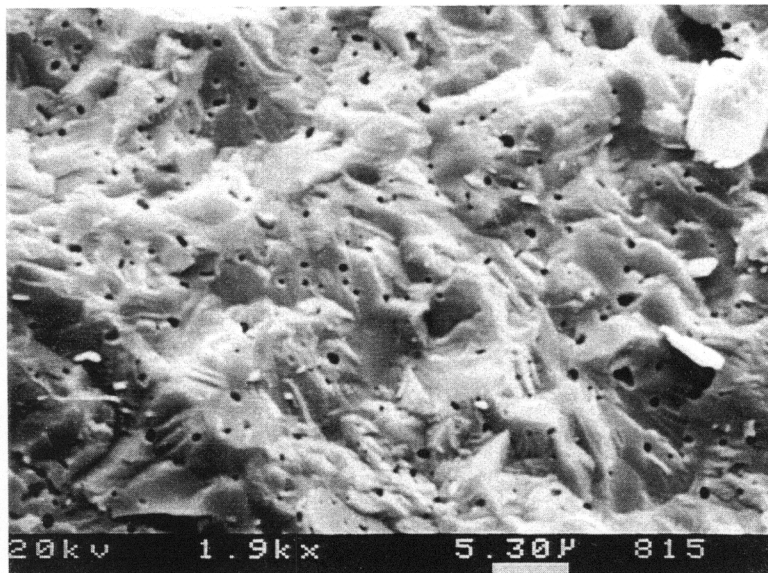


Figure 5.3b MOR bar fracture surface micrographs of slip cast sample (12-4) after thermal aging for 100h at 1000°C

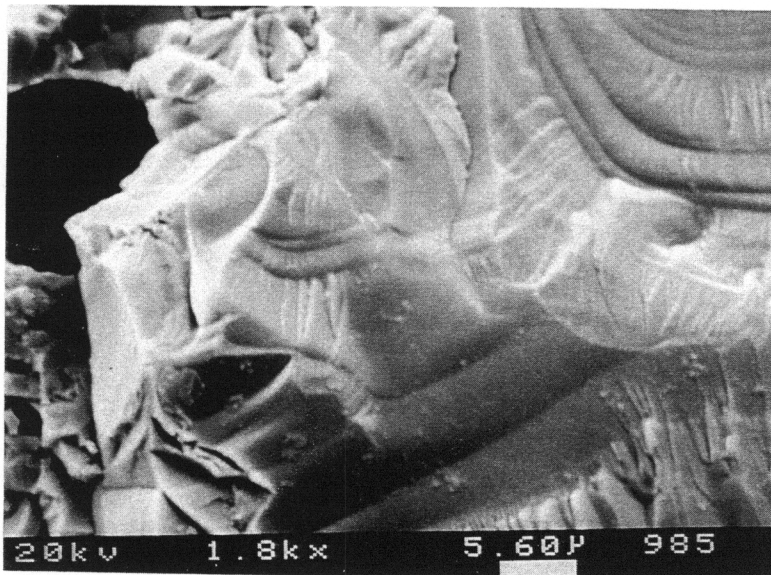
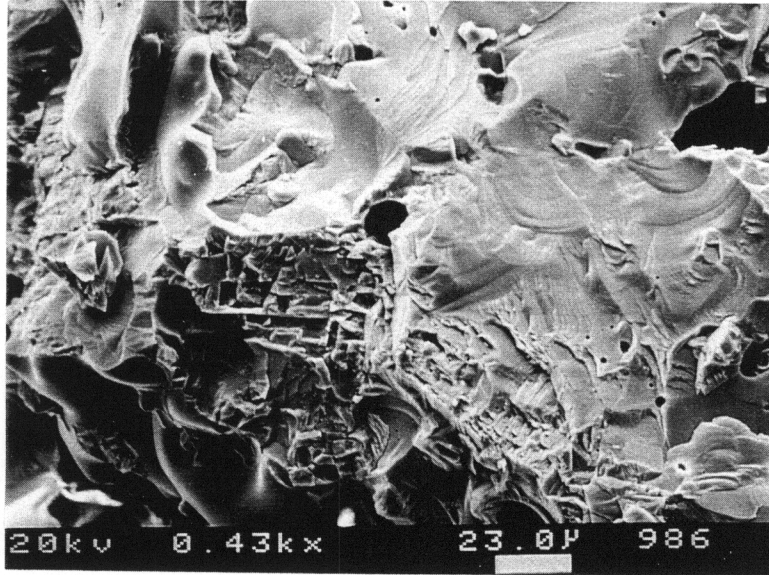


Figure 5.4 MOR bar fracture surface micrographs of slip cast sample (12-4) after thermal aging for 100h at 1200°C

6. CONCLUSIONS

This research has proven that CMZP ceramics can be processed to meet the requirements for diesel exhaust port liner applications in terms of strength and CTE. This research has also aided in the understanding of how ZnO affects the sintering of CMZP and the resulting material properties. Only through process improvements and better understanding of the development of material properties during processing can new materials, such as CMZP, be accepted as true engineering materials. The following conclusions were made:

1. The use of ZnO as a sintering aid greatly enhanced the sinterability of CMZP ceramics as exhibited by the high bulk densities (>97% of theoretical) achieved in both dry pressed and slip cast samples. However, excess ZnO reduces MOR and pushes CTE negative
2. Samples of high bulk density for a given forming method had microstructural characteristics consistent with liquid phase sintering mechanisms. These characteristics included secondary phase grain boundary formation, excessive/exaggerated grain growth, absence of an interconnected pore structure, and intergranular fracture surfaces.
3. The same microstructural characteristics responsible for high bulk density were detrimental to both the mechanical and thermal properties of CMZP ceramics, regardless of forming method. The development of these microstructural defects resulted in a significant decreases in MOR and a change in thermal expansion from positive to negative.
4. High strength and positive thermal expansion are obtained by adjusting the sintering parameters so as to avoid the onset of liquid phase sintering. The optimal firing time was shown to be less than 1 h and the optimal firing temperature was proven to be a function of the ZnO level.

5. Slip cast CMZP ceramics were processed to meet the design criteria for diesel exhaust port liners in terms of strength and thermal expansion. The best values obtained were a MOR of 111 MPa and an average CTE to 1000°C of +2.0 ppm/°C.

7. RECOMMENDATIONS

Based on the findings of this research, the following research is suggested as future work:

1. Sintering analysis of slip cast samples with ZnO levels in the 0.5% to 2% range focusing on determining the optimal sintering temperature for a given ZnO level so as to develop an empirical relationship between %ZnO and sintering temperature.
2. A more detailed analysis of high temperature aging effects on the mechanical and thermal properties of CMZP ceramics sintered with ZnO so as to determine the maximum use temperature for specific ZnO levels.
3. Determine the effects of calcining temperatures greater than 600°C on the sinterability and resulting material properties of CMZP ceramics.

REFERENCES

1. Personal Communication; Mike Long, Sr. Research Engineer, Caterpillar Inc.
2. Harrison, D.E., H.A. McKinstry, and F.A. Hummel, High Temperature Zirconium Phosphate, J. Amer. Ceram. Soc., 37 [6] pg.277-280 (1954).
3. Hagman, L.O. and P. Kierkegaard, The Crystal Structure of $\text{NaMe}_2^{\text{IV}}(\text{PO}_4)_3$; $\text{Me}^{\text{IV}}=\text{Ge, Ti, Zr}$, Acta Chemica Scandinavica, 22, pg.1822-1832 (1968).
4. Lenain, G.E., H.A. McKinstry, S.Y. Limaye, and A. Woodward, Low Thermal Expansion of Alkali-Zirconium Phosphates, Mat. Res. Bull., 19, pg.1451-1456 (1984).
5. Hazen, R.M., L.W. Finger, D.K. Agrawal, H.A. McKinstry, and A.J. Perotta, High Temperature Crystal Chemistry of Sodium Zirconium Phosphate (NZN), J. Mater. Res., 2 [3] pg.329-337 (1987).
6. Alamo, J. and R. Roy, Ultralow-Expansion Ceramics in the System $\text{Na}_2\text{O-ZrO}_2\text{-P}_2\text{O}_5\text{-SiO}_2$, J. Amer. Ceram. Soc., 67 [5] C-78-C-80 (1984).
7. Roy, R., D.K. Agrawal, J. Alamo, and R.A. Roy, [CTP]: A New Structural Family of Near-Zero Expansion Ceramics, Mat. Res. Bull., 19, pg.471-477 (1984).
8. Oota, T. and I. Yamai, Thermal Expansion Behavior of $\text{NaZr}_2(\text{PO}_4)_3$ -Type Compounds, J. Amer. Ceram. Soc., 69 [1] pg.1-6 (1986).
9. Alamo, J. and R. Roy, Crystal Chemistry of the $\text{NaZr}_2(\text{PO}_4)_3$, NZN or CTP, Structure Family, J. Mater. Sci., [21] pg.444-450 (1986).
10. Lenain, G.E., H.A. McKinstry, J. Alamo, and D.K. Agrawal, Structure Model for Thermal Expansion in $\text{MZr}_2\text{P}_3\text{O}_{12}$ ($\text{M}=\text{Li, Na, K, Rb, Cs}$), J. Mat. Sci., [22] pg.17-22 (1987).
11. Limaye, S.Y., D.K. Agrawal, and H.A. McKinstry, Synthesis and Thermal Expansion of $\text{MZr}_4\text{P}_6\text{O}_{24}$ ($\text{M}=\text{Mg, Ca, Sr, Ba}$), J. Amer. Ceram. Soc., 70 [10] C-232-C-236 (1987).
12. Kazakos-Kijowski, A., S. Komarneni, D. Agrawal, and R. Roy, Synthesis, Crystal Data and Thermal Stability of Magnesium Zirconium Phosphate [$\text{MgZr}_4(\text{PO}_4)_6$], Mat. Res. Bull., [23] pg. 1177-1184 (1988).

13. Hirschfeld, D.A., S.M. Van Aken, T.K. Li, Y. Yang, and J.J. Brown, Development of Ultra-Low-Expansion Ceramics: Synthesis, Thermal Expansion, Thermal Conductivity of $(Ca_{1-x}Mg_x)Zr_4(PO_4)_6$, Proceedings of the Automotive Technology Development Contractors' Meeting; Dearborn, MI, October, 1991 (Warrendale, PA: SAE Press, June 1992).
14. Hirschfeld, D.A., D.M. Liu, and J.J. Brown, CMZP-A New High Temperature Thermal Barrier Material, Proceedings of the Fourth International Symposium on Ceramic Materials and Components for Engines, June 1991, Goteburg, Sweden.
15. Richardson, D.W., Modern Ceramic Engineering, Marcel Dekker, NY, 1992.
16. Lay, R.W., and R.E. Carter, Time and Length Corrections in the Analysis of the Initial Stages of Diffusion-Controlled Sintering, J. Amer. Ceram. Soc., 52 [4] pg.189-191 (1969).
17. Coble, R.L., Effects of Particle-Size Distribution in Initial-Stage Sintering, J. Amer. Ceram. Soc., 56 [9] pg.461-466 (1973).
18. Huppman, W.J., S. Pejovnik, and S.M. Han, Processing of Crystalline Ceramics, Plenum, NY (1978).
19. Buessem, W.R., in Mechanical Properties of Engineering Ceramics, Interscience (1961).
20. VanAken, S.M., Thermal Expansion and Thermal Conductivity of $(Ca_{1-x}Mg_x)Zr_4(PO_4)_6$ where $x=0.0 - 0.4$, M.S. Thesis, VPI and SU, Blacksburg, VA (1990).
21. Kinoshita, M. and M. Inoue, The Reaction of Zirconium Diphosphate with Calcium Carbonate, J. Chem. Soc. of Japan, [8] pg.1219-23 (1980).
22. Agrawal, D.K. and V.S. Stubican, Synthesis and Sintering of $Ca_{0.5}Zr_2P_3O_{12}$ - A Low thermal Expansion Material, Mat. Res. Bull., Vol. 20, pg.99-106 (1985).
23. Alamo, J. and R. Roy, Revision of Crystalline Phases in the System $ZrO_2 - P_2O_5$, Comm. of the Amer. Cer. Soc., C-81, May 1984.
24. Li, T.K., D.A. Hirschfeld, S. VanAken, Y. Yang, and J.J. Brown, The Synthesis, Sintering, and Thermal Properties of $(Ca_{1-x}Mg_x)Zr_4(PO_4)_6$ [CMZP] Ceramics, J. Mater. Res., 8 [11] pg.2954-2967 (1993).
25. Reed, J.S., Introduction to the Principles of Ceramic Processing, Wiley-Interscience, N.Y., (1988).
26. B.L. Gabriel, SEM: A User's Manual for Material Science, ASM, Ohio, (1985).
27. Kingery, W.D., H.K. Brown, and D.R. Uhlmann, Introduction to Ceramics, Second Edition, Wiley-Interscience, N.Y., (1976).

28. Kuszyk, J.A. and R.C. Bradt, The Influence of Grain Size on the Effects of Thermal Expansion Anisotropy in $MgTi_2O_5$, J. Amer. Ceram. Soc., 56 [8] pg.420-423 (1973).
29. Cleveland, J.J. and R.C. Bradt, Grain Size/Microcracking Relations for Pseudobrookite Oxides, J. Amer. Ceram. Soc., 61 [11-12] pg.478-81 (1978).
30. Russ, W., Structure, Property, and Processing Relationships of CMZP, M.S. Thesis, VPI and SU, Blacksburg, VA (1994).
31. Yamai, I. and T. Oota, Low-Thermal-Expansion Polycrystalline Zirconyl Phosphate Ceramic: Solid-Solution and Microcracking-Related Properties, J. Amer. Ceram. Soc., 70 [8] pg.585-90 (1987).
32. Yamai, I. and T. Oota, Low-Thermal-Expansion Polycrystalline Zirconyl Phosphate Ceramic, J. Amer. Ceram. Soc., 68 [5] pg.273-278 (1985).

APPENDIX

Preliminary Research

The basic objective of this research was to determine the sintering parameters for CMZP that would give acceptable MOR and CTE values for Caterpillar's exhaust port liner design. A MOR greater than 90 MPa and a positive CTE were the two main goals. Although these sintering parameters were previously established for the sol-gel synthesized CMZP powder, a new, more efficient solid-state synthesis method warranted additional research. The change in particle size, and therefore reactivity, was the foremost concern with this new powder. How this change in reactivity, or sinterability, affected the optimal firing temperature, firing time, and sintering aid level needed to be determined. Given that ZnO was already proven to be a powerful sintering aid with NZP-type compounds, no other sintering aids were tested during this project.

Since the goal was to maximize MOR, the most logical plan of study was thought to maximize bulk density, which is generally proportional to strength for most ceramic systems. This indirect method was chosen since a good research base needed to be established and bulk density analysis was believed to be quicker and more efficient, allowing the most data to be gathered.

Time efficient research that produced the maximum amount information from a minimum number of samples was required. Therefore, a central composite experimental design with three main factors, Time, Temperature, and %ZnO, was adopted. From this set of 20 samples, the optimal sintering parameters could be determined.

This preliminary experimental design was constructed as follows:

Sample ID	Time	Temperature	%ZnO
(1)	11.25 h	1260°C	0.81%
(A)	20.75 h	1260°C	0.81%
(B)	11.75 h	1440°C	0.81%
(AB)	20.75 h	1440°C	0.81%
(C)	11.25 h	1260°C	3.19%
(AC)	20.75 h	1260°C	3.19%
(BC)	11.75 h	1440°C	3.19%
(ABC)	20.75 h	1440°C	3.19%
- α_A	8 h	1350°C	2.00%
+ α_A	24 h	1350°C	2.00%
- α_B	16 h	1200°C	2.00%
+ α_B	16 h	1500°C	2.00%
- α_C	16 h	1350°C	0%
+ α_C	16 h	1350°C	4.00%
ZERO (6 X's)	16 h	1350°C	2.00%

From this set of samples, an empirical formula for calculating bulk density was derived using statistical analysis of the bulk density data followed by a regression analysis using the significant factors, assuming a quadratic relationship. The following empirical formula was derived:

$$\text{Bulk Density } (\rho) = -100.5 + 22.51*(\%ZnO) - 1.464*(\%ZnO)^2 + 0.2541*(\text{Temperature}) - 8.857E^{-5}*(\text{Temperature})^2 - 0.01166*(\%ZnO*\text{Temperature})$$

Optimal values of 1260°C and 2.7wt% ZnO were calculated from the partial derivatives of %ZnO and temperature with respect to bulk density, or $(\partial\rho/\partial ZnO)$ and $(\partial\rho/\partial T)$, respectively. Under these conditions, a bulk density of 89% of theoretical was predicted. Since firing time did not prove significant, the optimal firing time had to be less than the 8 h time tested. Additional tests at 2.7wt% ZnO and 1260°C reproduced the bulk density value calculated by the empirical formula

and proved that the optimal firing time was less than 2 hours. The potential of higher bulk density values was also realized by reducing the particle size from the -100 mesh (7 μ m MPD) test condition. Reducing the particle size to -400 mesh, bulk densities 98% of theoretical were obtained after 0.33 h at 1260°C with 2.7wt% ZnO. These conditions were assumed optimal and served as the basis for many of the experiments outlined in Chapter 2. As determined later in the second experimental design that tested MOR, CTE, and bulk density, the conditions that produced high bulk density were detrimental to both mechanical and thermal properties. Microstructural analysis then provided the information needed to finalize the relationships between processing, microstructure, and properties. Once these relationships were realized, a new research approach was initiated that would eventually allow the desired mechanical and thermal properties of CMZP ceramics to be obtained through sintering optimization.

VITA

James Russell Clarke Jr. was a Graduate Research Assistant for Dr. Deidre Hirschfeld in the Material Science and Engineering Department at Virginia Polytechnic Institute and State University from August 1994 through July 1996. His research focused on the processing of a low thermal expansion ceramic material for potential application as thermal insulation in diesel engines. He was funded by Materials Technologies of Virginia (MATVA) through a DOE Energy Related Inventions Program. Most of his research was conducted at Caterpillar Inc. (Peoria, Ill.) at their Technical Center in the Advanced Materials Technology Division.

James is the son of Jim and Phyllis Clarke and was born in Elmer, NJ on March 7, 1971. He grew up in Bridgeton, NJ where he attended Hopewell Township grade school. He graduated from Cumberland Regional HS in 1989 and subsequently enrolled at Alfred University, graduating with a BS in Ceramic Engineering in May of 1994. While at Alfred University, he completed co-ops at Norton Chemical Process Products (Stow, OH) and Carborundum Monofrax (Jamestown, NY) as well as a summer internship with the Ames National Lab (Ames, IA).

Following graduation from Virginia Tech, he accepted a position at Corning, Inc. as a process engineer in the Environmental Products Division (Blacksburg, VA).

James R. Clarke Jr.